

Monte Carlo dose calculations for permanent breast seed implant brachytherapy

by

Stephen G Deering

A thesis submitted to the Faculty of Graduate and Postdoctoral Affairs
in partial fulfillment of the requirements for the degree of

Master of Science

in

Physics

Specialization in Medical Physics



Ottawa-Carleton Institute for Physics

Department of Physics

Carleton University

Ottawa, Ontario, Canada

July 2017

© 2017 Stephen Deering

Abstract

In order to investigate the use of patient-specific (rather than water-based) models for permanent breast seed implant (PBSI) brachytherapy, a retrospective study of 35 PBSI patients is performed. Virtual detailed-tissue patient models are created and overlaid with Pd-103 seed geometries, allowing for simulations with egs_brachy, a new Monte Carlo code.

Considerable discrepancies in dose distributions are demonstrated. Target dose metrics are 4-26% higher using TG43 assumptions, skin metrics are underestimated by up to 66.5%, and large disparities are observed in heart, lung, and rib doses. The sensitivity of dose distributions to assumptions in model creation is examined. Individualized adipose-gland segmentation thresholds and realistic seed orientations are shown to be important for accurate modeling. Radioprotective lead shielding has a negligible impact on skin dose.

This thesis demonstrates the importance of detailed patient modeling for PBSI brachytherapy, illustrating the shortcomings of TG43-based simulations and contributing to the future clinical implementation of model-based dose calculation algorithms.

Acknowledgments

I'd like to thank all the people who helped this thesis take shape over the last two years. First, I'd like to thank my family. Without the support of Patsy, Lorne, Connor, and Joe, I would have never been able to successfully finish this project.

Thanks to my supervisor, Dr. Rowan Thomson. Her continual guidance and enduring patience was appreciated more than words can express.

I thanks my collaborators at the BC Cancer Agency, Dr. Michelle Hilts and Dr. Deidre Batchelar, for all the work and insight that has taken place behind the scenes.

And I'd like to thank my colleagues and friends at Carleton Laboratory for Radiotherapy Physics for all the questions answered and hours they've had to put up with me; Martin Martinov, Patty Oliver, Nelson Miksys, Mehan Haidari, Marc Chamberland, Randy Taylor, and Zack Parsons.

Statement of originality

This thesis contains the bulk of my research undertaken at Carleton University over the course of this Masters degree. The results presented in the following pages will be presented at national and international conferences, and form the first draft for a paper to be published in a peer reviewed journal. Additionally, this is the first work presented using the new Monte Carlo code, egs-brachy. Over the course of this work, many software bugs were identified and fixed, contributing to the eventual public release of egs-brachy.

Dr. Rowan Thomson contributed to every aspect of this study, from the initial study design and methods, to the final revisions of this thesis manuscript. Our collaborators at the BC Cancer Agency, Dr. Deidre Batchelar and Dr. Michelle Hilts created the initial patient database, assisted in study design, and provided an important clinical perspective.

The material contained in this thesis will be presented by the author at the following conferences:

S. Deering, M. Hilts, D. Morton, D. Batchelar, MP. Millete, and R. M. Thomson.

Monte Carlo dose calculations for permanent breast seed implant brachytherapy

- Presented as a poster at the 2017 Canadian Organization of Medical Physicists (COMP) Annual Scientific Meeting in Ottawa, ON.

S. Deering, M. Hilts, R. Taylor, and R. Thomson. *Applications of egs-brachy for patient-specific model-based dose calculations for brachytherapy*

- Oral presentation given at the 2017 American Association of Physicists in Medicine (AAPM) Annual Meeting in Denver, CO.

Contents

Abstract	ii
Acknowledgments	iii
Statement of originality	iv
Table of contents	vi
List of tables	vii
List of figures	x
Nomenclature and notation	x
1 Introduction	1
1.1 Breast cancer: ductal carcinoma in situ	1
1.2 Radiation therapy	2
1.2.1 External beam therapy	3
1.2.2 Permanent breast seed implant brachytherapy	4
1.3 Treatment planning and evaluation	5
1.4 Model-based dose calculation algorithms	9
1.5 Thesis purpose	12
1.6 Thesis outline	13
2 Methods	15

2.1	Patient cohort database	15
2.2	Development of virtual patient models	16
2.2.1	Metallic artifact reduction	17
2.2.2	Tissue assignment schemes	20
2.3	Seed positioning within patient models	27
2.4	Lead shield modeling	28
2.5	Dose calculations with egs_brachy	29
2.6	Analyzing dose distributions	31
3	Results	35
3.1	Comparison of MCref and TG43sim models	35
3.1.1	Cohort target dose metrics	41
3.1.2	Cohort normal tissue dose metrics	44
3.2	Sensitivity to modeling choices	55
3.2.1	Adipose / Gland segmentation	55
3.2.2	Seed orientation	61
3.3	Lead shielding	67
4	Discussion	69
4.1	Comparison of MCref and TG43sim models	69
4.2	Sensitivities in patient modeling	73
4.3	Evaluation of treatment doses	76
4.4	Future directions	78
5	Conclusions and Outlook	80
A	CT Calibration Curve	83
	References	84

List of Tables

2.1	Composition and mass density values for phantom assigned tissues	19
2.2	Target adipose proportions for MCref and MCfixed models	26
3.1	Dose metrics for MCref and TG43sim virtual models in patient #14 . . .	40
3.2	Cohort D ₉₀ values for targeted regions in simulations of MCref and TG43sim	43
3.3	Mean cohort volume metrics for targeted regions in simulations of MCref and TG43sim.	44
3.4	Cohort skin dose metrics for simulations of MCref and TG43sim	47
3.5	Mean values of dose metrics over patient cohort for regions of interest in simulations of MCref and TG43sim models	48
3.6	Dose metrics for targeted regions in simulations of MCref and MCfixed .	56
3.7	Skin dose metrics for MCref and MCfixed models	60
3.8	<i>PTV0.5</i> D ₉₀ metrics in simulations of MCref, MCref-45, and MCref-z .	62
3.9	Skin D _{1cm²} metrics in simulations of MCref, MCref-45, and MCref-z . .	66
A.1	CT calibration curve for the conversion of pixel Hounsfield Units into mass density values	83

List of Figures

1.1	Geometry of a Theraseed 200 ^{103}Pd seed	5
1.2	Mass-energy absorption coefficient data for common bodily tissues	9
2.1	Visualizing the converison of raw CT images to a full detailed model . . .	17
2.2	Example of the metallic artifact reduction process	20
2.3	Tissue assignment schemes used in model creation	21
2.4	Breast mass density histogram	23
2.5	3D visualization of a MCref virtual patient model	24
2.6	Visualization of alternative seed orientation schemes	27
2.7	Sample D ₉₀ extraction from a DVH	32
2.8	Sample V ₂₀₀ extraction from a DVH	33
3.1	A dose ratio colourwash of MCref and TG43sim for patient #14	36
3.2	Dose volume histograms for the <i>PTV0.5</i> of patient #14	38
3.3	Dose ratio colourwash of MCref and TG43sim for patient #14 with a finer scale	39
3.4	Cohort target D ₉₀ values for MCref and TG43sim Models	42

3.5	Cohort skin dose metrics for MCref and TG43sim models	46
3.6	Rib dose metrics for MCref and TG43sim models	49
3.7	Chest wall dose metrics for MCref and TG43sim models	49
3.8	Heart metrics for MCref and TG43sim models	50
3.9	Scatter plot of the mean heart doses for MCref and TG43sim models . .	51
3.10	Ipsilateral lung metrics for MCref and TG43sim models	52
3.11	Full breast dose metrics for MCref and TG43sim models	52
3.12	Homogeneity and conformity indices for MCref and TG43sim models . .	53
3.13	Ratio of homogeneity and conformity indices for MCref and TG43sim models	54
3.14	Relationship between $\% \Delta PTV0.5 D_{90}$ and patient adipose-gland bound- aries	57
3.15	Volume metric ratios between MCref and MCfixed patient models	58
3.16	Relationship between $\% \Delta$ skin D_{1cm^2} and patient adipose-gland boundaries	59
3.17	Volume metric ratios between MCref and MCref-z or MCref-45 patient models	63
3.18	$\% \Delta$ of patient cohort skin dose metrics due to seed orientation	64
3.19	$\% \Delta$ of patient cohort rib dose metrics due to seed orientation	65
3.20	$\% \Delta$ of patient cohort chest wall dose metrics due to seed orientation . .	65
3.21	$\% \Delta$ of patient cohort homogeneity and conformity indices due to seed orientation	67
3.22	A dose ratio colourwash of MCref and MCref-Pb for patient #14	68

Nomenclature and notation

- DCIS** Ductal Carcinoma in Situ
- PBSI** Permanent Breast Seed Implant (Brachytherapy)
- MBDCA** Model-Based Dose Calculation Algorithm
- MC** Monte Carlo
- CTV** Clinical Target Volume
- PTV** Planning Target Volume
- DVH** Dose Volume Histogram
- HI** Homogeneity Index
- CI** Conformity Index
- CT** Computer Tomography
- HU** Hounsfield Units
- MAR** Metallic Artifact Reduction
- STR** Simple Threshold Replacement
- TAS** Tissue Assignment Scheme
- KERMA** Kinetic Energy Released per unit MAss
- AAPM** American Association of Physics in Medicine
- TG43** AAPM Task Group 43
- TG186** AAPM Task Group 186
- BCCA** British Columbia Cancer Agency
- TOHCC** The Ottawa Hospital Cancer Centre
- ICF** Inhomogeneity Correction Factor

Gy Gray [1 joule / kilogram]

ρ Density [g / cm³]

μ_{en}/ρ Mass-energy absorption coefficient

Ψ Photon energy fluence

hν Mass-energy absorption coefficient

Z_{eff} Effective atomic number

K_{col} Collision kerma

D_X Minimum dose received by the hottest X% of a region

V_X Percentage volume of a region receiving X% of the prescribed dose

D_{1cm²} Dose received by the hottest 1 cm² of a region

%Δ Percentage difference between metrics (Eq. 4.1)

Chapter 1

Introduction

1.1 Breast cancer: ductal carcinoma in situ

The Canadian Cancer Society estimates that 2 in 5 Canadians will develop cancer at some point in their lives, with an estimated 202 000 new cases expected to be diagnosed and treated in 2016 alone¹. As Canada's population ages, this number is only expected to increase. Among Canadian women, the most common of these diagnosed cases is breast cancer, accounting for 26% of all female cancer diagnoses and 25 700 new cases in 2016. Despite a rising number of breast cancer diagnoses, the female breast cancer mortality rate (per 100 000) in Canada has been declining since the mid-1980s¹, largely thanks to improvements in cancer screening and therapy treatment procedures. These screenings, mainly consisting of the wide-spread use of mammography in clinics across Canada, have also lead to a considerable increase in the detection rate of treatable, early-stage breast cancers, the most common form of which is Ductal Carcinoma in Situ, DCIS².

DCIS is a non-invasive (or pre-invasive) form of breast cancer. Consisting of abnormal cells located in the milk ducts of the breast, it usually first presents as lesions or small microcalcifications seen during routine mammograms³. After initial identification, a biopsy is performed to confirm the diagnosis and classify the stage and extent

of the DCIS present. DCIS on its own will not spread outside the breast, but if left in place may become invasive and spread to other tissues. To prevent this from happening, two main treatment options are available.

The traditional treatment approach for DCIS is a full mastectomy², completely removing all cancerous tissue along with the remainder of the breast. A mastectomy is typically performed on patients with large or diffuse areas of DCIS or on patients unable to receive radiation therapy. While effective in treating DCIS, mastectomies are physically and mentally demanding of patients, creating demand for an alternative approach. This alternative treatment, the option pertinent to the work in this thesis, is a breast-conserving lumpectomy followed by a regime of radiation therapy⁴. The lumpectomy removes all identified areas of DCIS along with a buffer of healthy tissue. The surgeon attempts to retain as much healthy tissue as possible, allowing for the general structure of the breast to be maintained. But even with an additional buffer of tissue around the tumour taken during surgery, the possibility of microscopic portions of cancerous cells remaining in the breast exists. To prevent the possible survival and proliferation of cancerous cells, leading to a potential recurrence of DCIS, radiation treatment is prescribed as an adjuvant therapy. Patients treated with a combination of lumpectomy and radiation therapy have been shown to have superior outcomes when compared to patients treated solely with a lumpectomy^{5,6}. The lumpectomy-radiation combination treatment also has comparable recurrence rates to complete mastectomy treatments^{5,6}, while being considerably less invasive and body altering, making it an attractive treatment option for patients fitting the selection criteria.

1.2 Radiation therapy

Radiation therapy treatments use ionizing radiation to impart energy into patient cells, attempting to cause cell damage in targeted cancerous regions⁷. If a high enough radia-

tion dose is delivered, measured in Gray ($1 \text{ Gy} = 1 \text{ J/kg}$), cancer cells will sustain critical DNA damage, causing either cell death or an inability to reproduce⁸. On a macroscopic scale, radiation therapy can be used to kill or slow the growth of tumours, without the need for surgical intervention. However, radiation dose is also highly damaging to healthy tissues. This makes accurate treatment planning, execution, and evaluation essential for delivering the maximum possible dose to the targeted tumour region, while simultaneously minimizing the radiation damage done to nearby sensitive organs.

1.2.1 External beam therapy

Traditionally, DCIS radiation therapy treatments are delivered using external beam radiation therapy. External beam therapy delivers the prescribed dose through the use of linear accelerators (LINACs), which produce a high-energy particle beam able to accurately target the cancerous region. However, no matter how accurately the LINAC beam is able to target the tumor region, delivered radiation must still pass through skin on the path to the target. This unavoidable skin dose often causes unwanted side effects, potentially resulting in long-term, painful skin damage. Another drawback of external beam radiation therapy is the need for treatment fractionation to maximize treatment effectiveness. In fractionation, the total required radiation dose is divided into many smaller dose fractions, which are then delivered in frequent treatment sessions over the course of several weeks. While medically optimal, the duration and frequency of treatments needed for proper radiation fractionation can put significant personal stress on DCIS patients, leading some patients to refuse external beam treatment or opt for a mastectomy.

1.2.2 Permanent breast seed implant brachytherapy

A radiation therapy alternative to the external beam method is found in brachytherapy. Brachytherapy involves the implantation of many small, sealed containers of radioactive material (known as seeds or sources) directly into patient tissues⁹. As the seeds are located in the immediate vicinity of the targeted area, the required photon energy for treatment is very low. These low energies lead to a sharp decline in photon fluence with distance, preventing high amounts of energy deposition outside of the immediate seed vicinity. This dose localization, along with the ability to accurately position the implanted seeds, allows for the creation of highly conformal dose distributions from within the patient.

For post-lumpectomy DCIS patients, a brachytherapy alternative to external beam irradiation is permanent breast seed implantation (PBSI). First pioneered in 2006¹⁰, it consists of 50 to 120 ¹⁰³Pd seeds implanted into the target through the lateral breast wall. Ultrasound imaging allows a fiducial needle to position seeds at a predetermined depth and angle according to a calculated treatment plan. Over the course of a 1 hour surgery¹⁰, many ¹⁰³Pd seeds (eg. TheraSeed Model 200 seeds as seen in Figure 1.1) are positioned around the lumpectomy site in order to deliver the prescribed dose of 90 Gy, while also attempting to minimize the dose to skin¹¹. These ¹⁰³Pd seeds are chosen for their particularly low-energy spectra, dominated by 20.1 and 22.7 keV photons¹², which are ideal for preventing high doses outside of the target. After a brief recovery period, PBSI patients are discharged on the same day as arrival and surgery, only requiring a follow-up evaluation at 1 month post-implantation.¹³



Figure 1.1: The geometry of a Theragenics Co., TheraSeed 200. The seed consists of a lead marker (red) sandwiched between two cylindrical, radioactive ^{103}Pd coated graphite pellets (maroon), and enclosed inside a titanium tube (brown). The seed is 4.50 mm long with a diameter of 0.826 mm.

1.3 Treatment planning and evaluation

Currently, all clinical dose calculations for PBSI brachytherapy are performed according to the method suggested in the report of Task Group 43 (TG43), as published by the American Association of Physicists in Medicine¹⁴. Although the TG43 formalism does allow the user to account for source orientation when performing brachytherapy dose calculations, it recommends the use of a one-dimensional, point source approximation when seed insertion angles are not well defined. As seed orientation is often unknown or unrecorded during PBSI treatments, the one-dimensional formalism is frequently used.

To calculate dose distributions, TG43 parameters are pulled from a pre-calculated database¹⁵ by the treatment planning system, having been determined through a combination of precise water phantom measurements and Monte Carlo simulated dose distributions. To calculate a multi-seed dose distribution, individual seed dose distributions are superimposed, combining the contributions of each individual source. The TG43 method has been successfully implemented in clinical brachytherapy treatment planning systems around the world for several reasons. By providing a straightforward method for the creation of treatment dose distributions in water, inter-clinic consistency in treatment planning is improved. Using pre-calculated TG43 parameters in dose calculation eliminates the need for clinicians to perform precision dose measurements or create

Monte Carlo models, further increasing consistency. And in using a 1-D formalism to calculate dose distributions for PBSI treatment planning and evaluation, no angular seed orientations are required. Unlike seed positions, discernible on CT images due to internal lead markers, these seed orientations are extremely difficult to determine on post-surgery CT images.

While the TG43 formalism provides a fast and practical method for clinical treatment planning, it has many inherent simplifications. Patients are approximated as an infinite body of water, ignoring the presence of many non-water tissues in the patient, such as gland, adipose, cortical bone, and skin, as well as the existence of an air interface on the patient exterior. Patient tissues can differ considerably from water in both elemental composition and density (Table 2.1). These differences are of particular importance when examining the energy deposition for the low energy photons produced by a ^{103}Pd source, for reasons covered in the following paragraphs.

As radiation therapy photons travel through media, they interact primarily in one of four main ways: the photoelectric effect, incoherent/Compton scattering, coherent/Rayleigh scattering, and pair (or triplet) production¹⁶. These interactions cause photon attenuation, reducing the number (N), and potentially the energy (E), of photons further “downstream” in the medium. Photon attenuation, characterized by the linear attenuation coefficient μ , results in a lower photon fluence (ϕ) and energy fluence (Ψ). For a monoenergetic photon beam of energy $h\nu$, the photon fluence can be defined by the number of photons entering an imaginary sphere of cross-sectional area dA ⁷:

$$\phi = \frac{dN}{dA}, \quad (1.1)$$

with the energy fluence similarly defined as the energy crossing dA

$$\Psi = \frac{dE}{dA} = h\nu \cdot \phi. \quad (1.2)$$

Of the four previously mentioned photon interactions, only Compton scattering and the photoelectric effect are relevant for energy deposition at the energy scales of PBSI brachytherapy, as no pair production interactions occur at keV brachytherapy energies and Rayleigh interactions transfer no energy to charged particles. Relevant interaction cross sections are dependent on photon energy ($h\nu$), as well as the medium effective atomic number, Z_{eff} (a weighted average of atomic numbers for medium comprised of a mixture of elements). At higher energies, Compton scattering is the predominant form of photon interaction. This is because the atomic cross section for photoelectric interaction has a photon energy dependence of $(h\nu)^{-3}$, a stark contrast to Compton scattering, whose atomic cross section has comparatively little photon energy dependence at brachytherapy energies. The Compton atomic cross section does have a linear dependence on Z_{eff} , but this linear dependence is not enough to create a large difference in atomic cross section for media of similar Z_{eff} . However, for ^{103}Pd photons, the photoelectric effect is the predominant interaction. The atomic cross section for the photoelectric effect is highly dependent on the effective atomic number of the media involved, proportional to roughly Z_{eff}^4 . Thus, small changes in elemental composition can potentially have large effects on the observed photon interaction cross section in brachytherapy treatments.

The transfer of energy from photons to charged particles in the surrounding medium is described by the medium's kerma (Kinetic Energy Released per unit MAss). Kerma can be broken down into its two components, radiative kerma (K_{rad}), which represents transferred energy that is lost to radiative interactions, and collision kerma (K_{col}), which

represents the transferred energy that is eventually absorbed locally by the medium through ionizational electron interactions. Although collision kerma is not the same as radiation dose (it is calculated at the location of photon interaction rather than the site of energy deposition) the two are nearly equivalent at low energies due to the short distances traveled by the electrons (relative to the length-scales being considered). Collision kerma is also a much easier quantity to calculate than dose, as it can be defined in a medium ‘m’ for a monoenergetic photon beam as

$$(K_{col})_m = \Psi \cdot (\mu_{en}/\rho)_m. \quad (1.3)$$

This equation demonstrates that the energy transferred into a medium is directly proportional to photon energy fluence (Ψ) as well as the medium mass-energy absorption coefficient, $(\mu_{en}/\rho)_m$. Since the amount of energy deposited by photons in a medium depends strongly on the number of photon interactions in that medium, variation in media μ_{en}/ρ values are caused by changes in the underlying atomic cross sections. So at low brachytherapy energies, μ_{en}/ρ strongly depends on Z_{eff} , just like the atomic cross section for the photoelectric effect. This means that the differences in elemental composition and Z_{eff} between water and breast tissues create a large discrepancy in medium μ_{en}/ρ values (Figure 1.2). At 20.7 keV, the mean energy of a photon leaving a TheraSeed200 ^{103}Pd source¹⁷, the ratios of mass-energy absorption coefficients of adipose and gland versus water, $(\mu_{en}/\rho)_{water}^{adipose}$ and $(\mu_{en}/\rho)_{water}^{gland}$, are 0.591 and 0.798 respectively. Thus, the TG43 formalism assumption of a water equivalent patient is not an accurate representation of reality, as breast tissues are far from being radiologically water equivalent at brachytherapy energies.

Additionally, the TG43 protocol ignores the impact of interseed attenuation on patient dose distributions. The use of lead and titanium in the construction of a TheraSeed

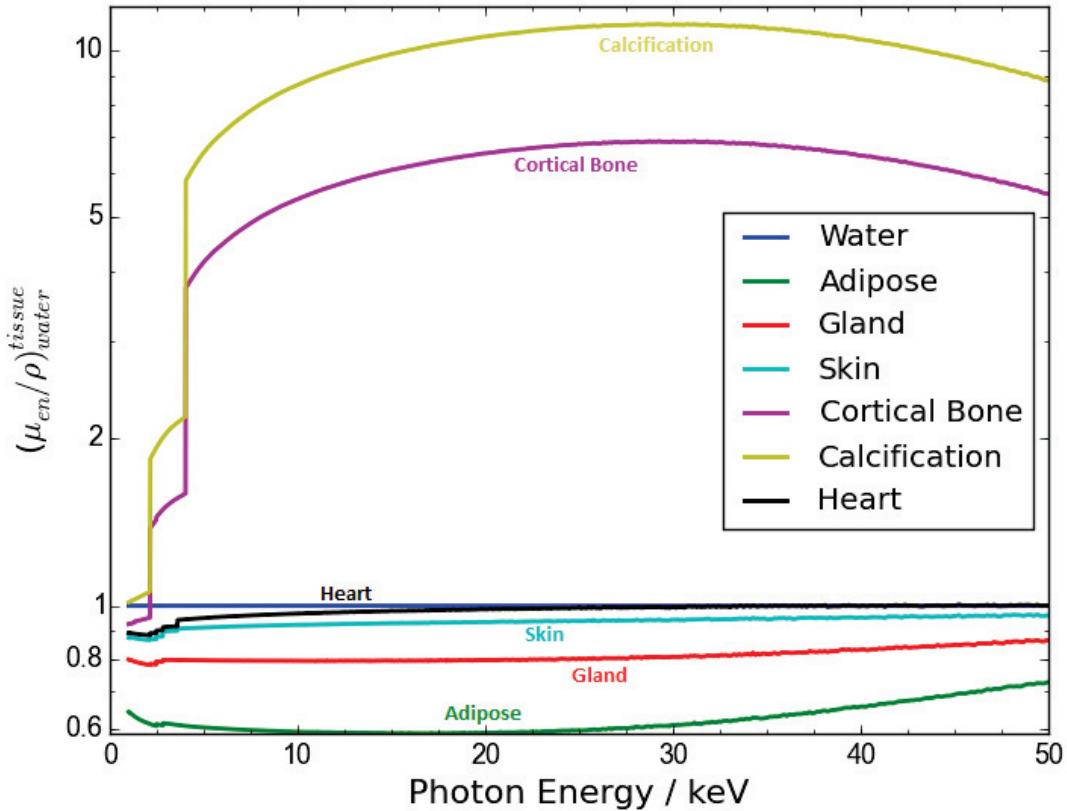


Figure 1.2: Mass-energy absorption coefficients for several important tissue compositions used in the thesis, normalized to the mass-energy absorption value of water. The energy range shown spans typical energies for PBSI brachytherapy treatments.

200 brachytherapy source introduces additional high-Z materials into the field of photon fluence, the presence of which is completely disregarded by the TG43 approach of superimposing pre-calculated single seed dose distributions.

1.4 Model-based dose calculation algorithms

Due to the shortcomings of TG43-based dose calculation methods, a relatively recent report by AAPM Task Group 186 endorsed the use of Model-Based Dose Calculation Algorithms (MBDCAs) for brachytherapy applications¹⁸. One of the most promising

possible approaches to MBDCAs is the use of Monte Carlo (MC) techniques to simulate radiation propagation and energy deposition. Patient-specific treatment models are created using advanced geometry packages and combined with MC radiation transport software, allowing for the accurate simulation of detailed patient geometries. In egs_brachy¹⁹, the MBDCA used in this work, patient models are constructed from a large number of voxels (volumetric-pixels). Voxels serve as model building blocks and are assigned an elemental tissue composition and mass density based on CT imaging (elaboration can be found in Section 2.2.2). Simulation geometries also include detailed models of sources and applicators, a necessary addition for the simulation of detailed treatments. Currently, the published literature also describes several different MC codes able to perform dose calculations using these patient-specific models, including PTRAN²⁰, Brachydose²¹, and ALGEBRA²².

Some early MC studies quantified the importance of considering non-water tissue and interseed attenuation when performing dose calculations for different treatments. For an electronic Xoft x-ray source in breast tissue, Taylor et al²³ found that accounting for the effects of non-water media leads to dose decreases of greater than 10% within 1 cm of the source. With a ¹⁰³Pd treatment plan in prostate tissues, Chibani and Williamson²⁴ showed that the minimum dose delivered to 100% of the prostate volume (D_{100}), was 6% lower when the prostate was modeled as soft tissue, as opposed to pure water. Using patient data, Carrier et al²⁵ found differences of 7% between the clinical TG43 techniques and their MC results over a retrospective dosimetry study of 28 prostate patients, concluding that TG43 based techniques were consistently overestimating the dose received by the prostate and surrounding organs.

Research has also begun to investigate the use of MBDCAs in the planning and evaluation of breast brachytherapy treatments. Early work often focused on determining the impact of accurately modeling the breast. Initially approximated as a 50/50

adipose/gland mixture in x-ray and dosimetry studies, work by Yaffe et al²⁶ showed this to be a poor estimation of realistic breast tissue, finding mean breast compositions to be primarily adipose (74.4% - 86.3%), but with large variations between women. These inter-patient variations in adipose proportion have been shown to have significant dosimetric effects^{27,28,29} in blended adipose-gland breast models, where a uniform adipose-gland mixture is assigned to every voxel in the breast. However, Sutherland et al³⁰ and Afsharpour et al²⁷ suggest that these blended tissue compositions are also not accurate representations of an actual breast, suggesting models with realistically segmented adipose-gland tissues, where each voxel is assigned either gland or adipose (not a mixture), should be used.

Recent MCBDA breast brachytherapy PBSI studies have further improved the accuracy of virtual breast models and begun to catalog the shortcomings of TG43-based dosimetry. Patient-specific, adipose-gland segmented phantoms have become more common^{31,32,33,34}, using patient CT data to create individualized patient models for specific treatment plans. Miksys et al^{31,32} provided guidelines for breast model creation, giving insight into the application of metallic artifact reduction techniques and investigating the sensitivity of patient dose distributions to tissue modeling choices. Adipose-gland segmentation has been performed using fixed density boundaries to delineate adipose and gland tissue, defined either by cohort CT data³³ or literature review³² as well as individualized patient-specific boundaries, defined on a patient-by-patient basis through the analysis of CT data³⁵. Dose distributions generated using detailed tissue patient-specific models were compared to those using TG43-based models, noting that TG43-based simulations consistently overestimate the dose to the target region by large amounts, while simultaneously underestimating skin dose^{31,32,33,34}. The existing literature confirms the importance of modeling non-water tissue and interseed attenuation, justifying the need for further research into the use of model-based dose calculation

algorithms.

1.5 Thesis purpose

Recent works by Miksys et al^{31,32} and Afsharpour et al^{33,34} have created detailed patient-specific models for use in calculating PBSI brachytherapy dose distributions. These studies have demonstrated that TG43 based models overestimate target dose metrics³² and underestimate doses to the skin³², as well as analyzing the impact of accurate dosimetry when evaluating radiobiological indices³⁵. But aside from research performed on a small, 4 patient cohort by Miksys et al in 2016³², little work has been published examining the sensitivity of model-based dose distributions to uncertainties in several important aspects of patient virtual model creation. Furthermore, implant practices may vary considerably between institutions, as few standards exist for treatment planning, surgical implant techniques, number and strength of seeds, and definition of the target. In moving towards the clinical implantation of MBDCA methods, further research into the dosimetry of patient-specific MC modeling is essential.

This thesis explores MC dosimetry for a cohort of 35 PBSI patients recently treated at the BC Cancer Agency (BCCA). It is the first dosimetric study to use egs_brachy, a new MC code specifically for brachytherapy purposes. By demonstrating the ability of egs_brachy to perform accurate MC simulations of PBSI patients, this work hopes to provide an important intermediate step towards the potential future implementation of egs_brachy into clinical treatment planning systems. Detailed virtual models are developed alongside traditional TG43 water-based models, and a comprehensive comparison of dose metrics is undertaken to evaluate the ability of the MC models to predict the brachytherapy radiation dose delivered to the target and surrounding tissues. As the BCCA has only recently (2012³⁶) begun to perform PBSI treatments, this will be the first use of detailed tissue dose distributions to evaluate their current surgical and treat-

ment planning procedures. To conduct this evaluation, an exhaustive number of dose metrics are extracted, including heart, lung, and rib dose metrics not previously examined by any MC PBSI study. Lastly, an investigation of dose distribution sensitivity to decisions in model-creation is performed for the first time with a moderately sized cohort. The choice of a fixed-threshold or variable-threshold approach to adipose-gland segmentation is explored. Three different seed orientations are examined in order to investigate the dosimetric impact of accurately modeling seed alignment. Finally, a preliminary investigation into the dosimetric influence of a bra-inserted lead shield specific to the BCCA is performed. In summary, the goals of this thesis are to:

- develop a patient-specific MC model to simulate patient PBSI doses;
- compare the dosimetric results of full-tissue, detailed MC modeling to standard water-based TG43 models;
- assess the dosimetric influence of fixed versus individualized adipose-gland threshold boundaries;
- determine the effects of varying seed orientation on patient dose distributions;
- investigate the potential impact of a lead bra-insert on patient skin dose.

1.6 Thesis outline

Chapter 1 has provided a brief review of some of the medical physics concepts required for understanding the work presented by the thesis. An introduction to breast PBSI brachytherapy has been provided and some current PBSI modeling techniques are touched upon. **Chapter 2** provides the methods used in the thesis, outlining the techniques required to create accurate MC brachytherapy dose distributions. Virtual breast models are created for each patient, the MC algorithm egs_brachy is introduced,

and the extraction of clinical dose metrics is explained. **Chapter 3** presents the results of a dosimetric analysis. Beginning with an individual patient example, patient doses from a TG43-based and a detailed reference model are compared. Results for the full cohort are then presented, comparing water-based and tissue-based models. Variations in tissue assignment, seed orientation, and lead shielding are also explored. **Chapter 4** provides a discussion of the reported results. Comparisons are made to the published PBSI literature, treatment performance is evaluated, and the limitations of current model-creation procedures are highlighted. **Chapter 5** concludes the thesis, summarizing the work's major findings and providing insight into future research opportunities in the field of MC PBSI modeling.

Chapter 2

Methods

2.1 Patient cohort database

The patient cohort for this work consists of 35 patients treated with permanent ^{103}Pd breast seed implants at the BC Cancer Agency - Southern Interior. Patient data use in this study has been approved by the UBC BC Cancer Agency Research Ethics Board, and was reviewed by the Carleton University Research Ethics Board. A database of post-operative patient data is created according to the DICOM (Digital Imaging and Communications in Medicine) standard and securely transferred to Carleton servers. Anonymized, post-implant CT data, taken one month after surgery, are composed of 71-240 torso slices of 2 mm thickness, each made up of a 512 x 512 grid of 0.977-1.25 mm square pixels. The patient cohort was not pre-screened for the presence of breast calcifications.

For each patient, data from physician-drawn organ contours are included in the database. These structures include the clinical target volume (*CTV*), planning target volume 0.5 (*PTV0.5*), planning target volume 1.0 (*PTV1.0*), breast, ribs, skin, ipsilateral lung, heart, and chest wall. For this work, the *CTV* is defined as the surgical seroma, a pocket of bodily fluid formed around the region of removed tissue. The *PTV0.5* is defined as the *CTV* plus an additional 5 mm buffer. For the BC Cancer Agency, this *PTV0.5* contour defines the target for all PBSI radiation therapy treatment

planning, and will be referred to as the target throughout this work. The *PTV1.0* is the largest target region, defined as the *CTV* with an extra 10 mm buffer. Locations of the 52-118 Theragenics Co., Theraseed 200 ^{103}Pd radioactive seeds are recorded, along with the corresponding air kerma strengths and angles of surgical insertion. This is all post-operative information required to recreate and evaluate the treatment received by each patient. The goal of these treatments is to deliver a prescription minimum dose of 90 Gy to the target (*PTV0.5*), while minimizing the dose received by the skin and other normal tissues.

2.2 Development of virtual patient models

To create virtual patient models from raw CT images, several steps need to be taken (Figure 2.1). First, a metallic artifact reduction technique must be applied. The presence of brachytherapy seeds inside a patient breast during CT imaging creates high-density CT artifacts. These artifacts are caused by the high-Z, high-density seed materials sharply increasing photon attenuation and scattering around the source. This disruption of photon fluence is captured by the CT scanner, presenting as high-density artifacts. As these artifacts are located in or around targeted breast regions, they can lead to large errors in dose^{37,38}. To mitigate the dosimetric effects of seed artifacts, a metallic artifact reduction (MAR) technique (Section 2.2.1) is applied to the CT data prior to the next step in the model creation process.

Next, MAR-corrected, post-implant CT data are used to create patient-specific voxelized virtual models, known as phantoms. CT pixels are one-to-one mapped to a corresponding phantom voxel, providing information necessary to assign voxel tissue compositions and densities. This tissue assignment is guided for each model by its tissue assignment scheme (TAS, Section 2.2.2). To assign voxel tissue compositions, the TAS checks each phantom voxel position against all known organ locations, deter-

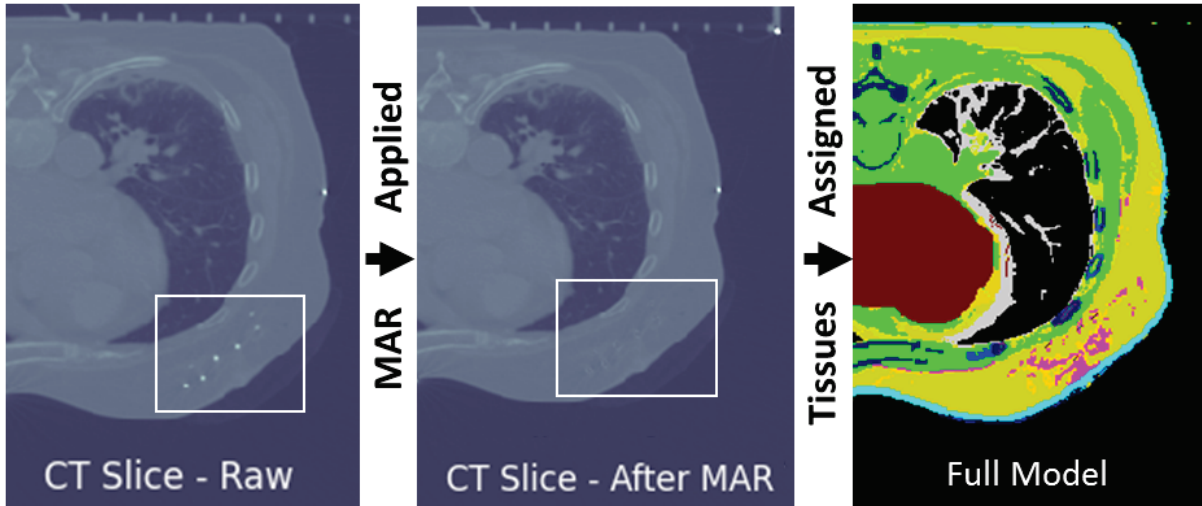


Figure 2.1: Starting from a sample raw DICOM-CT image (left), a Metallic Artifact Reduction technique is applied to prepare for model creation (middle). Tissues are assigned on a voxel-by-voxel basis to create a full tissue egs-brachy patient model (right), with skin (teal), gland (pink), adipose (yellow), heart (red), lung (gray), and bone (blue) tissues visible.

mined by comparing the voxel center position to the volumes enveloped by the provided physician-drawn contours. Once an organ is specified, voxel tissue composition is assigned by comparing the CT-pixel’s density against the scheme’s list of tissue types and densities for said organ. A list of tissues available for assignment, along with composition information, is found in Table 2.1. To assign voxel mass density (required for MC simulation of radiation transport and energy deposition), CT-derived density values are assigned to the phantom on a voxel-by-voxel basis in all detailed models (ie., models with non-water tissues assigned) used in this work. As CT data is in Hounsfield Units, a conversion to pixel density is required, determined by a machine-specific CT calibration curve acquired through routine quality assurance (Appendix A).

2.2.1 Metallic artifact reduction

If left uncorrected, a detailed tissue assignment scheme will assign high density, high μ_{en}/ρ calcification to existing CT artifact voxels. As these calcifications are located immediately around the seed, photon fluence will be reduced throughout the breast,

considerably changing dose distributions in the phantom. To mitigate this, several approaches to MAR have been suggested in the literature, such as Standard Threshold Replacement (STR)^{31,38,39}, median filter^{31,38,40}, and fan beam virtual sinogram^{31,39,41,42} approaches. For this thesis, STR is used, as recommended by Miksys et al³² for its straightforwardness and effectiveness. STR has been shown to prevent the false assignment of dense, calcification media in sensitive areas, while preserving the assignment of real calcification tissue and retaining the segmentation between gland and adipose tissue inside the breast.

An in-house Python script was created to perform STR on PBSI patient images. All voxels within a 0.5 cm radius cylinder, extending two slices above and below, of all recorded seed positions are checked against a chosen STR cutoff density of 1.16 g cm^{-3} , defined by the calcification assignment boundary in breast tissue outside of STR-checked regions. If a voxel density exceeds this 1.16 g cm^{-3} cutoff, it is flagged as artifact. All artifact voxels are replaced with the mean density of patient target tissue, 0.917 g cm^{-3} , leading to an eventual tissue assignment of adipose. A low density cutoff of 0.800 g cm^{-3} , well below the range of normal breast tissue density, is also applied to all voxels inside the breast contour to mitigate any possible dark streaking seed artifacts. For clarity, the STR procedure is outlined in Figure 2.2.

Table 2.1: Elemental compositions and mass density values for phantom assigned tissues^{43,44,45}. Regions associated with each tissue are indicated as: (B)reast, (C)hest Wall, (H)eart, (L)ung, (R)ibs, (S)kin, (E)lse.

Tissue	ρ (g cm ⁻³)	Composition (Mass %)				
		H	C	N	O	Other
Adipose1 ⁴⁴ (B,C,R)	0.970	11.2	51.7	1.3	35.5	Na(0.1), S(0.1), Cl(0.1)
Adipose2 ⁴⁴ (B,C,R)	0.950	11.4	59.8	0.7	27.8	Na(0.1), S(0.1), Cl(0.1)
Adipose3 ⁴⁴ (B,C,R)	0.930	11.6	68.1	0.2	19.8	Na(0.1), S(0.1), Cl(0.1)
Air (L,S,E) ⁴⁵	0.001	0.07	0.01	75.0	23.6	Ar(1.27)
Bone ⁴⁴ (C,R,E)	1.920	3.4	15.5	4.2	43.5	Na(0.1), Mg(0.2), P(10.3), S(0.3), Ca(22.5)
Cartilage ⁴⁴ (C)	1.100	9.6	9.9	2.2	74.4	Na(0.5), P(92.2), S(0.9), Cl(0.3)
Calcification (B) ⁴³	3.060	0.3	1.6	0.5	40.7	P(18.7), Ca (38.2)
Gland1 ⁴⁴ (B)	0.990	10.9	50.6	2.3	35.8	Na(0.1), P(0.1), S(0.1), Cl(0.1)
Gland2 ⁴⁴ (B)	1.020	10.6	33.2	3.0	52.7	Na(0.1), P(0.1), S(0.2), Cl(0.1)
Gland3 ⁴⁴ (B)	1.060	10.2	15.8	3.7	69.8	Na(0.1), P(0.1), S(0.2), Cl(0.1)
Heart ⁴⁴ (H)	1.050	10.4	13.9	2.9	71.8	Na(0.1), P(0.2), S(0.2), Cl(0.2), K(0.3)
Lung ⁴⁴ (L)	1.050	10.3	10.5	3.1	74.9	Na(0.2), P(0.2), S(0.3), Cl(0.3), K(0.2)
R. Marrow ⁴⁴ (R)	1.030	10.5	41.4	3.4	43.9	P(0.1), S(0.2), Cl(0.2), K(0.2), Fe(0.1)
Y. Marrow ⁴⁴ (R)	0.980	11.5	64.4	0.7	23.1	Na(0.1), S(0.1), Cl(0.1)
Muscle ⁴⁴ (C,E)	1.050	10.2	15.8	3.7	69.8	Na(0.1), P(0.1), S(0.1), Cl(0.1)
Skin1 ⁴⁴ (S)	1.090	10.0	25.0	4.6	59.4	Na(0.2), P(0.1), S(0.3), Cl(0.3), K(0.1)
Skin2 ⁴⁴ (S)	1.090	10.0	20.4	4.2	64.5	Na(0.2), P(0.1), S(0.2), Cl(0.3), K(0.1)
Skin3 ⁴⁴ (S)	1.090	10.0	215.8	3.7	69.5	Na(0.1), P(0.1), S(0.2), Cl(0.3), K(0.1)
Water ⁴⁵ (E)	0.998	11.2	0	0	88.8	-

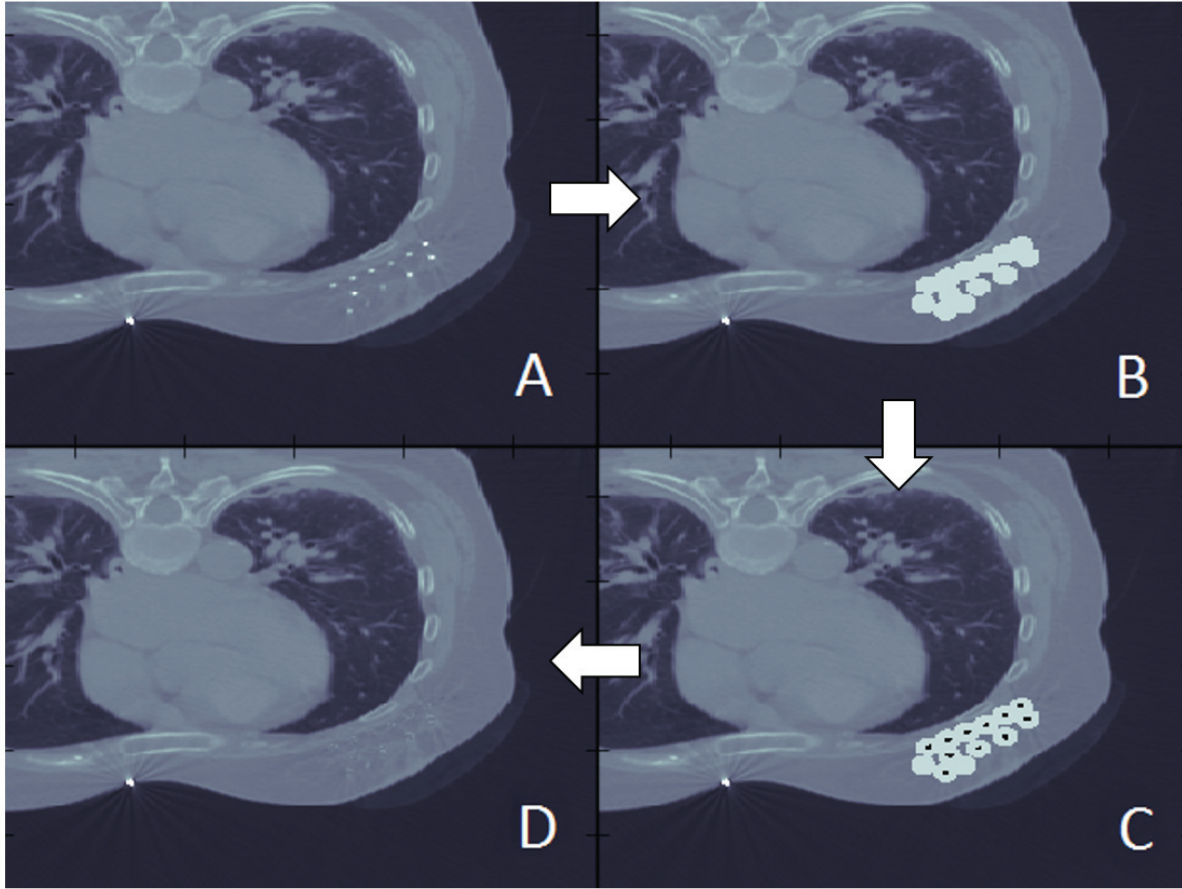


Figure 2.2: An example of the simple threshold replacement artifact reduction technique. Beginning with an initial CT image (A), voxels near seed positions (gray) are checked for possible artifacts (B). Identified artifact voxels, shown in black, (C) are then replaced to produce a STR processed CT slice (D).

2.2.2 Tissue assignment schemes

In this thesis, 3 different tissue schemes are presented: MCref, MCfixed, and TG43sim. MCref is modeled to serve as our reference MBDCA model, TG43sim to provide a TG43-analog for the evaluation of current treatment planning system methods, and MCfixed is modeled to investigate uncertainties in adipose-gland segmentation during tissue assignment. To investigate the effect of seed orientation on patient dose distributions (Section 2.3), the MCref phantom is used for multiple simulations.

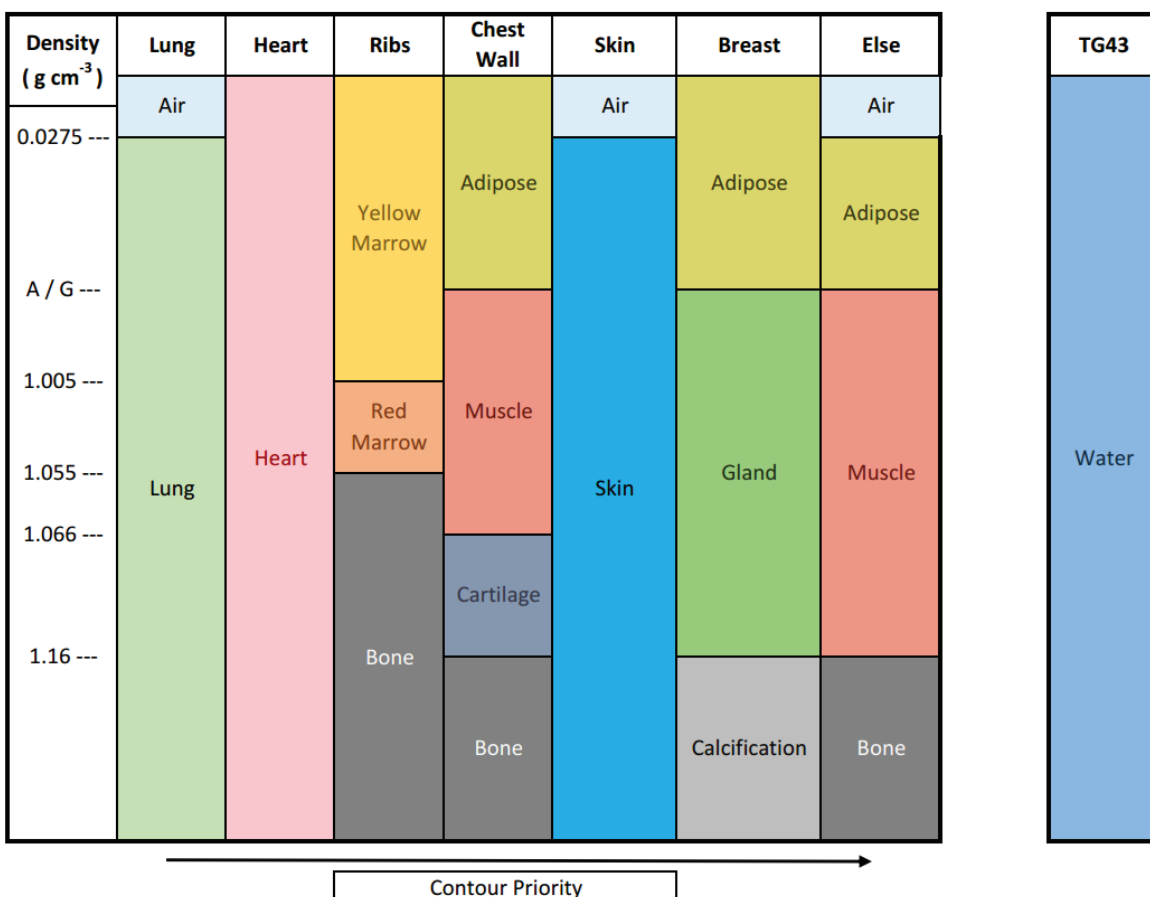


Figure 2.3: Overview of tissue assignment schemes used to create MCref, MCfixed, and TG43sim. Vertical axis density values are not to scale. In MCfixed, the floating A / G bound is fixed at 0.9476 g cm^{-3} . Tissue compositions are found in Table 2.1.

MCref

To construct MCref, voxels found inside of provided lung, heart, and skin contours are assigned ‘Lung–blood-filled’, ‘Heart 2’, and ‘Skin 2’⁴⁴ respectively, as recommended by TG186¹⁸. Skin and lung contours may also contain air, so low density voxels found in these contours, along with those along the exterior of the phantom, are assigned ‘Air’, a standard⁴⁵ air composition at 40% humidity. Inside rib contours, ‘skeleton– cortical bone’, ‘skeleton–red marrow’ and ‘skeleton–yellow marrow’⁴⁴ are assigned based on voxel density. A provided chest wall contour allows ‘skeleton–cartilage’ to be assigned, along with ‘Adipose 2’, ‘Muscle – skeletal 2’, and ‘skeleton– cortical bone’⁴⁴. Any voxels outside of these contours are considered to be in the Else contour, where adipose, muscle, air, and bone tissues are assigned, in line with TG186 recommendations.

The assignment of breast tissue composition is a source of considerable variation among models presented in the literature. PBSI MBDCA literature indicates that the segmentation of adipose and gland tissues in the breast is required for the accurate simulation of patient dose distributions^{18,30,33}, but several different methods to determine a density boundary for breast tissue segmentation have been presented^{32,33,35,46,47}. These methods can result in large composition variations in the immediate vicinity of seeds, the area most likely to affect photon fluence throughout the breast. Some recent brachytherapy breast models, used in work by Afsharpour et al (2012)³⁵ and White et al (2014)⁴⁷, were created using patient-specific density boundaries, derived from a patient-specific analysis of breast CT numbers.

For each patient, a voxel density histogram of the breast is created (Figure 2.4). A double-peaked Gaussian fit is performed on the resulting distribution, assuming that the densities of adipose and gland tissues follow a Gaussian distribution. Breaking the fit into the two component distributions, representing the volume of adipose and gland tissue present, the density values at the peak of the component adipose and gland

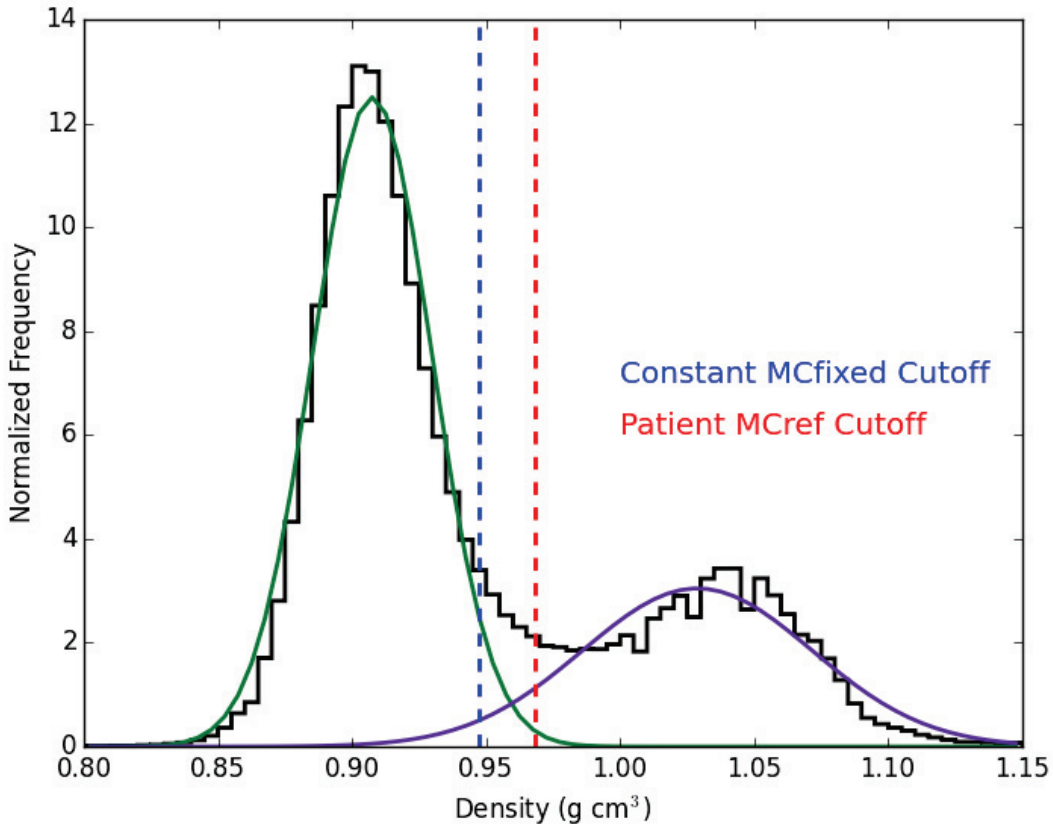


Figure 2.4: Normalized mass density histogram of breast voxels in an example patient. Adipose (purple) and gland (green) Gaussians are fitted and displayed, with the individualized and fixed adipose-gland boundaries overlaid.

distributions are taken. The halfway point between these two density values is taken to be the patient specific adipose-gland boundary (Figure 2.4). Several other methods of extracting the boundary value were investigated, based on various combinations of the component distribution variables (such as distribution σ , maxima, and statistical values α and β (type-I and type-II errors)), but the chosen method consistently demonstrated the best delineation of adipose-gland tissues, with the additional benefit of being simple to implement. These created adipose-gland boundaries range from 0.9179 to 0.9700 g cm^{-3} , with a mean value of 0.9476 g cm^{-3} .

The resulting boundary is then used to assign ‘Adipose 2’ and ‘Gland 2’ in the

breast⁴⁴. As the cohort was not pre-screened for the presence of calcification, 'Calcification'⁴³ tissue is also assigned in the breast. However, any calcification tissue remaining after the MAR treatment accounts for less than 0.2% of the overall breast volume in all patients, so this assignment has little effect. The complete MCref tissue assignment scheme is outlined in Figure 2.3.

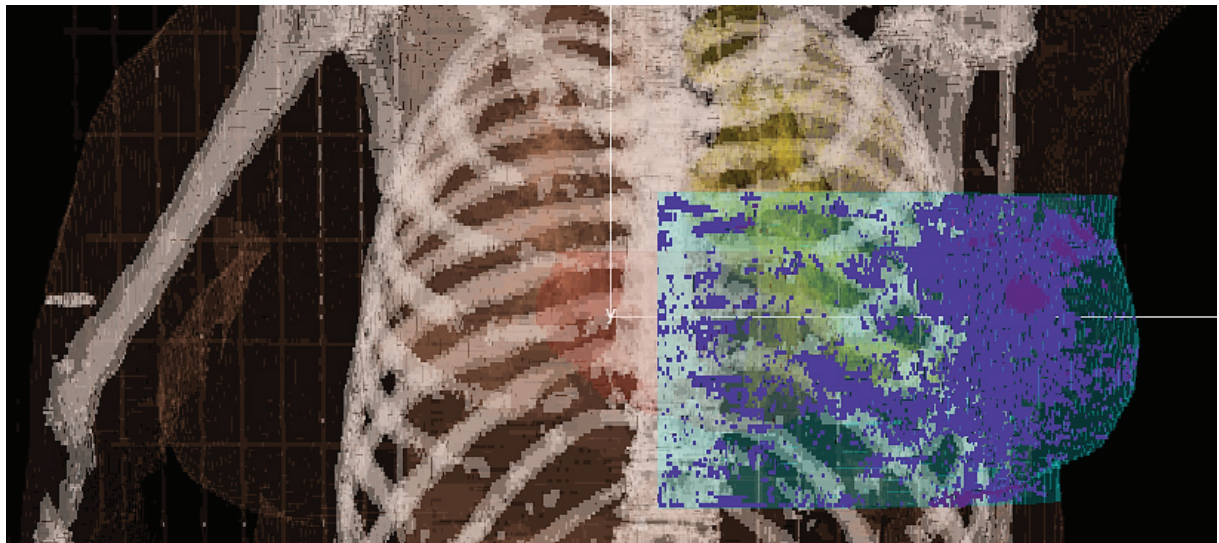


Figure 2.5: Sample MCref patient model imaged in egs-view, a package for viewing egs++ geometries. Several tissues and organs have made completely or partially transparent to allow for a clear view of internal tissues. Segmented adipose (semi-transparent green) and gland (purple) tissues are visible shown in purple).

MCfixed

To investigate the sensitivity of dose distributions to the adoption of a patient-specific adipose-gland cutoff for breast segmentation, an alternative MCfixed model is created. MCfixed uses a fixed adipose-gland cutoff boundary of 0.9476 g cm^{-3} , representing the mean value of the 35 individualized MCref boundaries, to segment adipose and gland tissues in the entire patient cohort. This value is comparable to other fixed-density adipose-gland density boundary values found in the literature, such as Afsharpour et al³³, who chose a value of 0.949 g cm^{-3} based on a density analysis of the

non-treated breast in ten randomly chosen patients and Miksys et al³², who examined two literature-based density values, 0.956 g cm^{-3} and 0.985 g cm^{-3} .

As the MCref gland-adipose density boundaries can vary between 0.9179 and 0.9700 g cm^{-3} , significant differences in breast adipose proportions between MCref and MCfixed models may occur. In patient #24, with an individualized boundary of 0.9179 g cm^{-3} , changing to the fixed 0.9476 g cm^{-3} adipose-gland boundary results in a percentage of breast assigned adipose increase of 19.8% (from 44.4% to 64.3%) in the *PTV0.5*. For the patient with the highest individualized adipose-gland boundary (#8), the change away from an adipose-gland boundary of 0.9700 g cm^{-3} results in a decrease of 12.7% in the proportion of *PTV0.5* voxels assigned adipose (from 43.1% to 30.4%). While these two patients represent the largest boundary differences, and therefore the largest shifts in composition, many other patient models shift by 5-15% in their adipose and gland breast proportions when transitioning between the MCref and MCfixed models (Table 2.2).

TG43sim

In order to allow for a direct comparison of MCref to TG43 conditions, the model TG43sim is also created. The TG43sim TAS assigns water media to all phantom voxels, and all voxel mass densities are overwritten, instead assigning a density of 0.998 g cm^{-3} ⁴⁵. When simulations using the TG43sim model are performed, the egs_brachy ‘Superposition’ run mode option is enabled¹⁹. This option allows egs_brachy to ignore interseed effects, as any non-photon emitting seeds are replaced with water for each history.

Table 2.2: Percentage of *CTV* and *PTV0.5* regions assigned adipose tissue from MCref and MCfixed tissue assignment schemes. Δ represents the difference in adipose percentage between the two schemes (MCref - MCfixed).

Patient Number	<i>CTV</i>			<i>PTV0.5</i>		
	MCref	MCfixed	Δ	MCref	MCfixed	Δ
1	11.4	9.9	1.5	32.5	28.7	3.8
2	18.5	11.7	6.8	44.1	33.0	11.2
3	23.4	32.1	-8.7	48.9	60.1	-11.2
4	15.1	14.5	0.6	24.7	22.8	1.9
5	11.0	9.3	1.7	38.7	34.4	4.3
6	26.5	20.1	6.4	37.8	29.7	8.1
7	4.9	3.6	1.3	31.1	24.4	6.7
8	15.7	9.5	6.2	43.1	30.4	12.7
9	15.3	17.8	-2.5	38.2	41.9	-3.7
10	15.1	13.3	1.7	33.7	28.0	5.7
11	17.2	15.9	1.2	37.5	34.8	2.7
12	16.6	18.5	-1.9	40.7	43.9	-3.2
13	14.6	15.4	-0.7	44.9	45.9	-1.0
14	13.6	12.4	1.2	31.8	29.6	2.2
15	3.4	3.4	0.0	25.5	25.5	0.0
16	14.7	15.5	-0.8	31.5	32.6	-1.2
17	32.0	26.4	5.7	50.5	43.0	7.5
18	14.4	23.1	-8.7	37.7	51.0	-13.4
19	14.7	17.3	-2.6	40.9	46.8	-5.8
20	16.2	15.5	0.8	39.8	38.2	1.6
21	18.1	25.0	-6.9	36.1	45.7	-9.6
22	10.2	12.7	-2.6	30.3	36.7	-6.4
23	14.4	14.8	-0.3	32.3	32.7	-0.4
24	27.1	45.8	-18.7	44.5	64.3	-19.7
25	6.6	9.3	-2.7	23.5	30.9	-7.3
26	18.4	20.8	-2.4	41.1	48.3	-7.2
27	55.4	69.6	-14.1	60.5	71.6	-11.1
28	26.3	21.4	5.0	36.2	30.8	5.4
29	13.3	14.7	-1.4	29.8	33.1	-3.3
30	34.0	20.8	13.2	58.0	45.3	12.7
31	18.2	15.8	2.4	37.9	33.8	4.1
32	36.6	31.8	4.8	57.5	52.2	5.2
33	12.6	10.7	1.9	35.8	30.9	5.0
34	4.8	6.9	-2.1	27.2	35.7	-8.5
35	13.4	12.3	1.1	45.5	44.1	1.4

2.3 Seed positioning within patient models

Before egs-brachy simulations can be performed, Theraseed 200 ^{103}Pd seed models must be inserted into all patient models. Modeled seed geometries are taken from the egs-brachy CLRP seed database¹⁹, having been benchmarked against previously published TG43 dosimetry parameters. As the superimposing of seed geometries into phantoms is separate from the phantom creation process, the same phantom can be simulated with several different seed configurations to test the effect of seed orientation on patient dose distributions and clinical dose metrics.

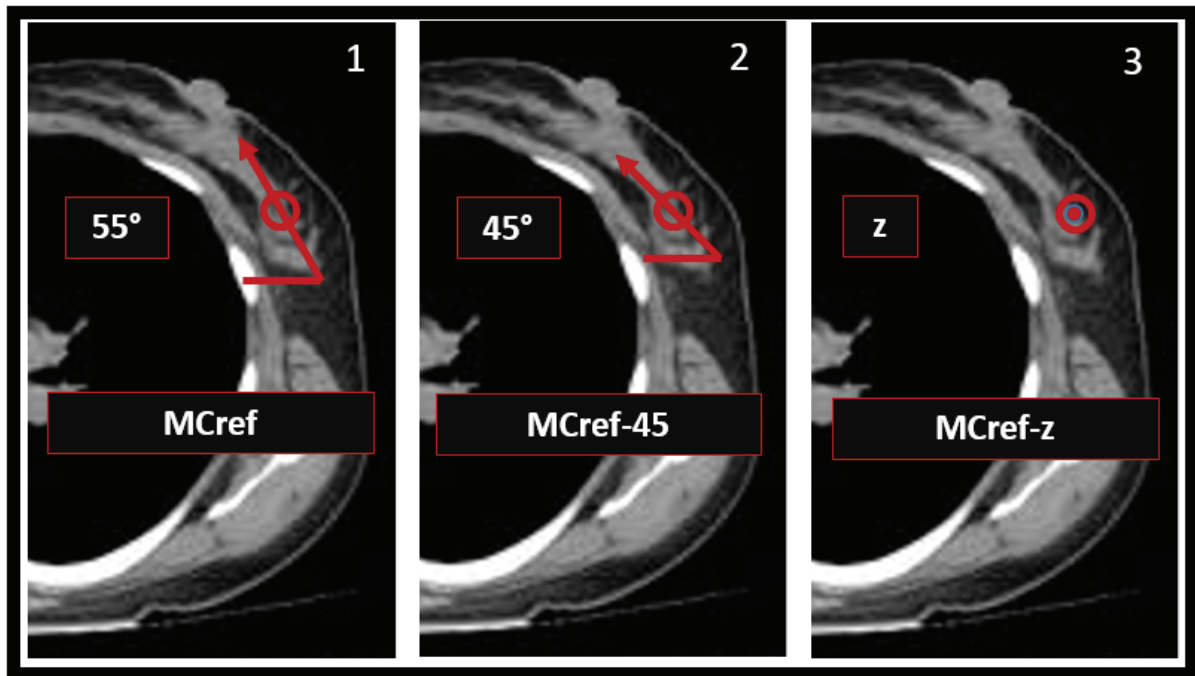


Figure 2.6: Visualization of the three different seed implant orientations used in the different schemes (MCref, MCref-45, and MCref-z) analyzed in this thesis.

In this study, three different seed orientations are simulated in the MCref phantoms, as seen in Figure 2.6. Designated as MCref-X, these simulations keep all non-orientation

factors constant, allowing the impact of seed orientation to be isolated. The first orientation option, MCref-z, has all seeds aligned along the z-axis (superior-inferior alignment relative to the patient). This is the default setting for brachytherapy simulations in egs-brachy, but a poor approximation of clinical reality, as the surgical implantation needle is inserted laterally, not vertically, into the breast. A second orientation option, MCref-45, also keeps a constant seed orientation across all patients, but positions the seeds at a 45° angle across the transverse plane. This approximates the actual possible angles of surgical insertion, without requiring the MBDCA end user to have access to detailed surgical information. The third approach, used in MCref (and thus having no suffix), models the seeds at the actual recorded angle of fiducial needle insertion. These angles are constant for all seeds in a single treatment, but each angle can differ significantly from the 45° approximation, varying between 10° and 70° depending on the location of the tumor relative to the breast, chest wall, and skin. The MCref orientation is our best estimation of actual patient seed angles. However, errors in orientation are unavoidable when using pre-recorded needle angles. Clinical treatment planning systems have internal 1° errors, in addition to further deviations occurring due to needle deflections while traveling through the breast tissue. As the best approximation of actual seed alignment, the MCref orientation is used in all models investigating sensitivity to tissue assignment schemes and the influence of lead shielding.

2.4 Lead shield modeling

To alleviate concerns about the possibility of mild radiation exposure to family and friends, many patients who undergo PBSI treatment at the BC Cancer Agency choose to wear a radioprotective lead shield (constructed in-house) for a short time after treatment. The shield is a 120 mm diameter bra-insert, consisting of a 0.15 mm lead portion surrounded on both sides by 0.4 mm of vinyl. In order to better understand the po-

tential dosimetric effects such a shield may have on target and skin dose, virtual shield models are individually created for each patient.

To create these patient shield models for a patient, an in-house python script was created. In each patient, the (x,y,z) coordinates for the mean seed position were found. A cylinder of 120 mm diameter is centered at this position, extending through the patient along the anterior-posterior (y) axis. Starting from air voxels on the anterior (+y) side of the patient, the script searches backwards (-y direction) until the first skin voxel is found. If said skin voxel is contained inside the bounding cylinder, it is overlaid with a voxel-sized portion of shield (modeled as a thin lead layer with a double-sided vinyl covering with accurate dimensions) on its air-facing side. This process is repeated for all voxels on the patient's anterior side (x-z plane), resulting in the construction of a individual lead shield model for each patient in the cohort. The resulting lead shields are overlaid on top of MCref patient models to create MCref-Pb. This new model allows for direct comparison to patient skin doses in MCref, forming the basis for a preliminary investigation into the effects of radioprotective lead shielding in PBSI brachytherapy.

2.5 Dose calculations with egs_brachy

In order to perform simulations with the newly created virtual models, a dose calculation algorithm is needed. For this work, egs_brachy (version 2016.09.01) is the chosen MBDCA. egs_brachy is a new, flexible EGSnrc MC user-code developed by the Carleton Laboratory of Radiotherapy Physics, capable of accurately calculating brachytherapy dose distributions in voxelized virtual patient models for a wide range of possible brachytherapy treatments¹⁹. It utilizes the EGSnrc code system⁴⁸ (v2016) to simulate photon and electron transport, and built-in and egs++ geometry libraries to model complex geometries. To verify accuracy, egs_brachy has been benchmarked against several other popular MC codes¹⁹.

Photons are simulated down to energies of 1 keV, effectively modeling photoelectric absorption, Rayleigh and Compton scattering, and the fluorescent emission of characteristic x rays. Initial photon energies are generated using a raw ^{103}Pd spectrum taken from TG43 published data⁴⁵. Photon cross sections are based on those from the National Institute of Standards and Technology XCOM database⁴⁹. To score dose, mass-energy absorption coefficients are pre-calculated using g , a separate EGSnrc user code, to be used with a collision kerma tracklength scoring estimator. This tracklength estimator scores dose to the i th voxel as:

$$D^i = K_{col}^i = \frac{1}{V_i} \sum_{k=1}^n E_k t_k (\mu_{en}(E_k)/\rho)_i \quad (2.1)$$

where V_i is the volume of the i^{th} voxel, E_k is the energy of the k^{th} photon, t_k is the length of the k^{th} photon track through the voxel, and $(\mu_{en}(E_k)/\rho)_i$ is the mass-energy absorption energy coefficient of the medium in the i^{th} voxel at energy E_k . The contribution from each photon is then summed over n photon histories. Although collision kerma is not the same as dose, the two are equivalent in brachytherapy simulations due to the short range of electrons involved relative to voxel dimensions.

All PBSI model simulations are performed with 10^9 photon histories on the Carleton University Physics Research Computer Cluster, leading to sub-1% statistical uncertainties in all target regions. In the skin, these uncertainties are sub-1% in 32 of 35 patients, sub 2-% in all patients (for skin voxels included in calculations of D_{1cm^2} , as defined in Section 2.6). Heart D_{1cm^2} voxels have statistical uncertainties below 1.5% for all patients with D_{1cm^2} values above 1 Gy (27/35). To reach these statistical uncertainties, simulations require between 8.4 and 12.0 computational hours, dependent on the size of the patient phantom, number of seeds implanted, and core speed. Other sources of uncertainty are also present in treatment simulations, often leading to greater dose

uncertainties than the statistical uncertainty alone. An estimation of the uncertainties introduced by interaction cross sections and seed geometries is difficult, but conservative estimates produce a value of 2%^{45,50}. Elemental composition of assigned tissues can differ between sources, introducing additional uncertainty into tissue μ_{en}/ρ values and created dose distributions³². For comparison, some available alternative gland, adipose, and skin compositions are presented in Table 2.1. Physician drawn contours introduce an element of human error, creating additional uncertainty in the assignment of tissues. Collectively, these additional uncertainties outweigh the relatively small statistical uncertainties on voxel dose.

Doses are scored to the local voxel medium as dose per simulated history. To calculate absolute dose, the use of a dose scaling factor is required, such that

$$D_{absolute} = \left(\frac{\tau \cdot S_{K,ref}}{S_{K,egs-brachy}^{hist}} \right) \cdot D_{egs-brachy} \quad (2.2)$$

where τ is the mean lifetime of the radionuclide used (16.991 days for ^{103}Pd ⁴⁵), $S_{K,ref}$ is the reference air-kerma rate, as measured by the clinic prior to implantation (ranging from 2.30 - 2.80 $\mu\text{Gy hr}^{-1}$ at 1 m), and $S_{K,egs-brachy}^{hist}$ is the egs-brachy air-kerma strength per history for the specific source model used in treatment, as calculated in separate egs-brachy simulations ($6.4255 \cdot 10^{-14} \text{ Gy cm}^2 / \text{history}$ for a TheraSeed 200 ^{103}Pd source).

2.6 Analyzing dose distributions

egs-brachy outputs simulation results in the form of a *3ddose* file, containing the dose delivered to each voxel, as well as the statistical uncertainties of voxel dose. To extract clinical dose metrics, dose volume histograms⁵¹ are constructed using an in-house python script, providing a graphical representation of the dose delivered to all voxels

contained in a specific region or organ of interest. These dose volume histograms are complementary cumulative distribution functions and allow for the extraction of important dose metrics, designated as D_X , the minimum dose received by $X\%$ of the defined region volume. In non-target regions, dose metrics can also be measured in absolute, rather than fractional, volume. These metrics will be indicated by using units cc (cubic centimeters). An example extraction of D_{90} is presented in Figure 2.7. For brachytherapy treatments, these D_{90} values are highly relevant to clinical medical physicists, as they allow for a direct comparison to the physician prescribed dose of 90 Gy. This provides a simple, effective technique for the evaluation of treatment plan efficacy.

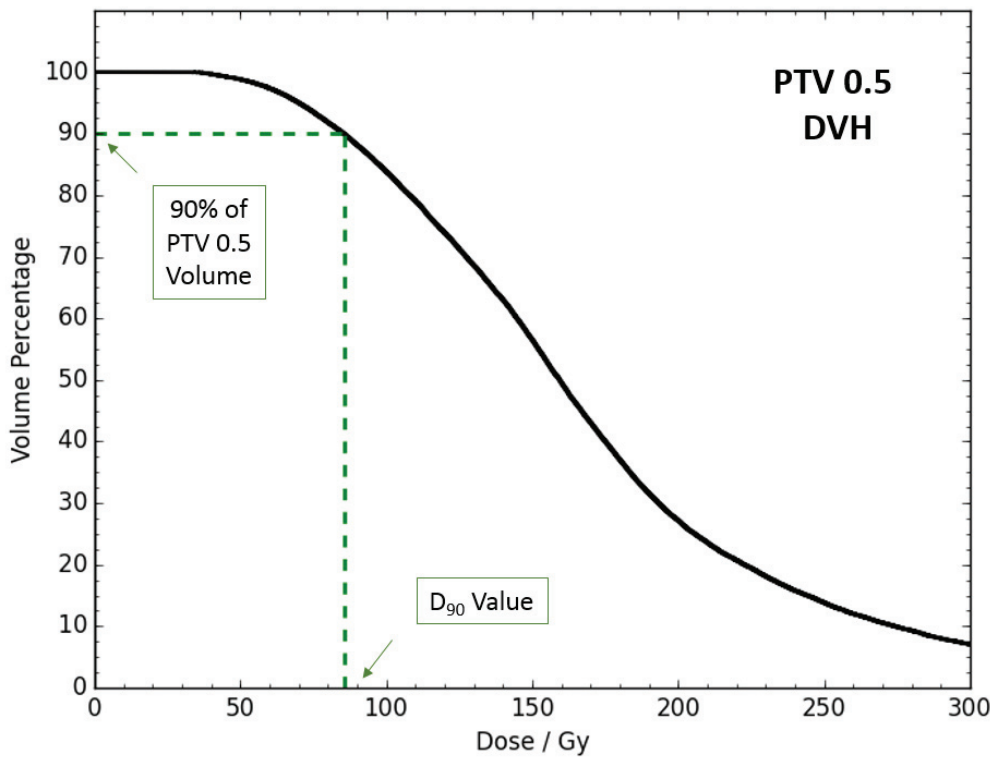


Figure 2.7: Sample extraction of a D_{90} metric from a patient $PTV0.5$ dose volume histogram.

For organs at risk, it is useful to define an additional dose metric, D_{1cm^2} . This metric is used when complications may be caused by dose hot spots, not necessarily a uniform irradiation of normal critical structures. D_{1cm^2} is defined as the highest dose received by a contiguous 1 cm^2 area in a region, but is usually approximated as

the minimum dose received by the hottest 0.2 cm^3 (approximately 100 voxels) of the structure.

Volume metrics, V_X , represent the fraction of a specified region receiving X percentage of the prescribed dose. Volume dose metrics can identify the percentage of successfully treated volume (V_{90} and V_{100}), regions of high target dose (V_{150} and V_{200}), and quantify the dosage to healthy, non-targeted organs (eg. $V_{10}(Heart)$).

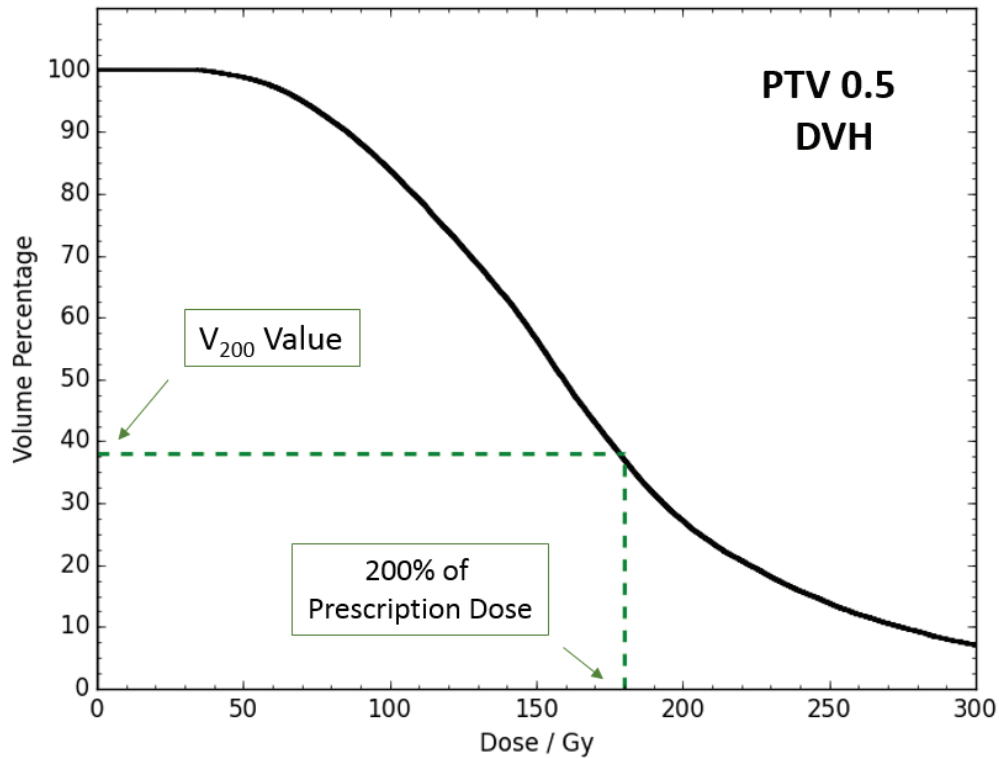


Figure 2.8: Sample extraction of a V_{200} metric from a patient $PTV0.5$ dose volume histogram.

Homogeneity and conformity indices are also used in the evaluation of PBSI treatments. The homogeneity index (HI), defined as

$$HI = 1 - \frac{V_{150}(PTV0.5)}{V_{100}(PTV0.5)}, \quad (2.3)$$

is a measure of the treatment plan's ability to homogeneously deliver a treatment dose without the creation of hot spots in the target. To examine how conformal the delivered

dose is to the target, the conformity index (CI) is defined as

$$CI = \frac{V_{100}(PTV0.5)}{(1 - V_{100}(PTV0.5)) + V_{100}(Body)}, \quad (2.4)$$

where the *Body* suffix indicates the entire patient body is considered.

This work often compares dose metrics produced by simulations of the reference model (MCref) with those extracted from alternative models (Alt), making it useful to define a standard formula for finding percentage differences ($\% \Delta$) of given metric (M) between models

$$\% \Delta = \frac{M_{MCref} - M_{Alt}}{M_{MCref}} \times 100\%. \quad (2.5)$$

As the absolute value of the difference is not taken, this formula can lead to negative $\% \Delta$ values, indicating that the alternative model resulted in an increase in the chosen dose metric.

Chapter 3

Results

3.1 Comparison of MCref and TG43sim models

Before presenting results for the comparison of MCref and TG43sim model dose metrics over the complete cohort, results for a single example patient are presented. Patient #14 is used, having near average dose metrics for both MCref and TG43sim, along with having easily distinguishable tissue types around the treatment area. To help visualize differences in dose distributions throughout the patient, a dose ratio colourwash is created by plotting the ratio of voxel doses (MCref/TG43sim) across a single CT slice (Figure 3.1). For consistency, this is the same slice from Patient #14 previously shown in both Figure 2.1 and Figure 2.2.

To understand the differences between MCref and TG43sim dose distributions (Figure 3.1), it is important to recall some of the concepts outlined in Section 1.3. Defined in Eq.(1.3), collision kerma in a medium is dependent on the product of photon energy fluence (Ψ) and energy dependent mass-energy absorption coefficient ($\mu_{en}(E_p)/\rho$). As collision kerma and dose are approximately equal in brachytherapy simulations, differences in voxel dose between models can be attributed to a change in one or both of these factors.

MCref target doses are generally lower than in TG43sim (Figure 3.2). In the breast,

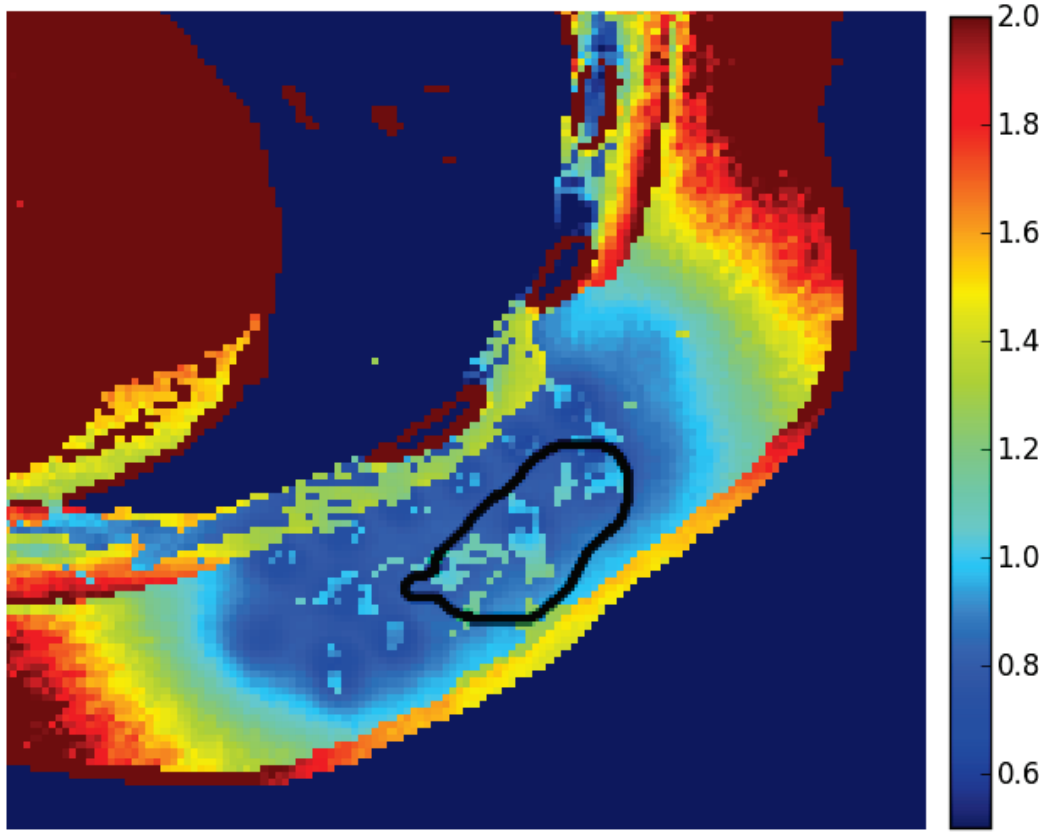


Figure 3.1: A colourwash of MCref/TG43sim dose ratios. The $PTV_{0.5}$ is outlined in black. For clarity in the skin and target regions, air and lung doses have been set to zero.

MCref assigns adipose and gland tissues instead of the homogeneous water found in TG43sim. At 20.7 keV (the average photon energy leaving a TheraSeed 200 source¹⁷) μ_{en}/ρ values decrease from $0.496 \text{ cm}^2/\text{g}$ in water to $0.293 \text{ cm}^2/\text{g}$ and $0.396 \text{ cm}^2/\text{g}$ in adipose and gland, respectively, resulting in less energy deposited in the target region. This also allows for the discrimination between gland and adipose tissue in Figure 3.1, as the differences in dose ratio due to μ_{en}/ρ value is not quite so large in glandular tissue. For some patients, dose received by some gland tissue is higher in MCref than in TG43sim (Figure 3.3). For gland tissue located distant from source positions, there may be sufficient increases in photon fluence (due to less attenuation in intervening breast tissue) to result in a higher dose to gland in MCref (than TG43sim), despite

the lower μ_{en}/ρ for gland compared to water. Despite this potential increase in MCref target dose, MCref target metrics are lower than the corresponding TG43sim metrics for all patients in the cohort, indicating that only small volumes of gland are affected.

The assignment of calcification media to voxels would strongly increase the dose delivered to those voxels (calcification has a very large $\mu_{en}(E_p)/\rho$ - Figure 1.2), but this effect is negligible due to the lack of calcification in post-MAR CT images. In the example patient (#14), calcification is assigned to just 0.02% of voxels. Lastly, the high-Z materials present in MCref modeled seeds cause dose ‘shadowing’ to occur. Photons are blocked or absorbed by the seed material, reducing photon fluence on the seed’s posterior side and lowering the amount of energy transferred to breast tissue.

Cumulatively, these phenomena create significant differences in target voxel doses, leading to large differences in target dose metrics (Figure 3.2 and Table 3.1). Patient *CTV*, *PTV0.5*, and *PTV1.0* D₉₀ values decrease between TG43sim and MCref by 7.7%, 12.5%, and 15.9%, respectively. In the *PTV0.5*, V₉₀, V₁₀₀, V₁₅₀, and V₂₀₀ values are decreased by 3.7, 4.6, 11.7, and 37%. A noticeable increase in D₉₀ %Δ occurs as the size of targeted region increases (from *CTV* to *PTV0.5* to *PTV1.0*). This is caused by an increase in the proportion of the target composed of adipose. In example patient #14, breast composition increases from 14% adipose in the *CTV* to 32% in *PTV0.5* to 44% in the *PTV1.0*, resulting in a higher fraction of the target comprised of lower μ_{en}/ρ media. From a biological perspective, an increase in adipose as the target region includes more peripheral tissue makes sense. DCIS forms in the glandular milk ducts of the breast, so any treatment of this disease is most likely centered (*CTV*) around the regions of highest gland composition.

In the skin, accurate media assignment has the opposite effect, as simulations using TG43sim underestimate the dose to skin (Figure 3.1). For low- energy photons, the density and mass-energy absorption coefficients of skin and water are much more

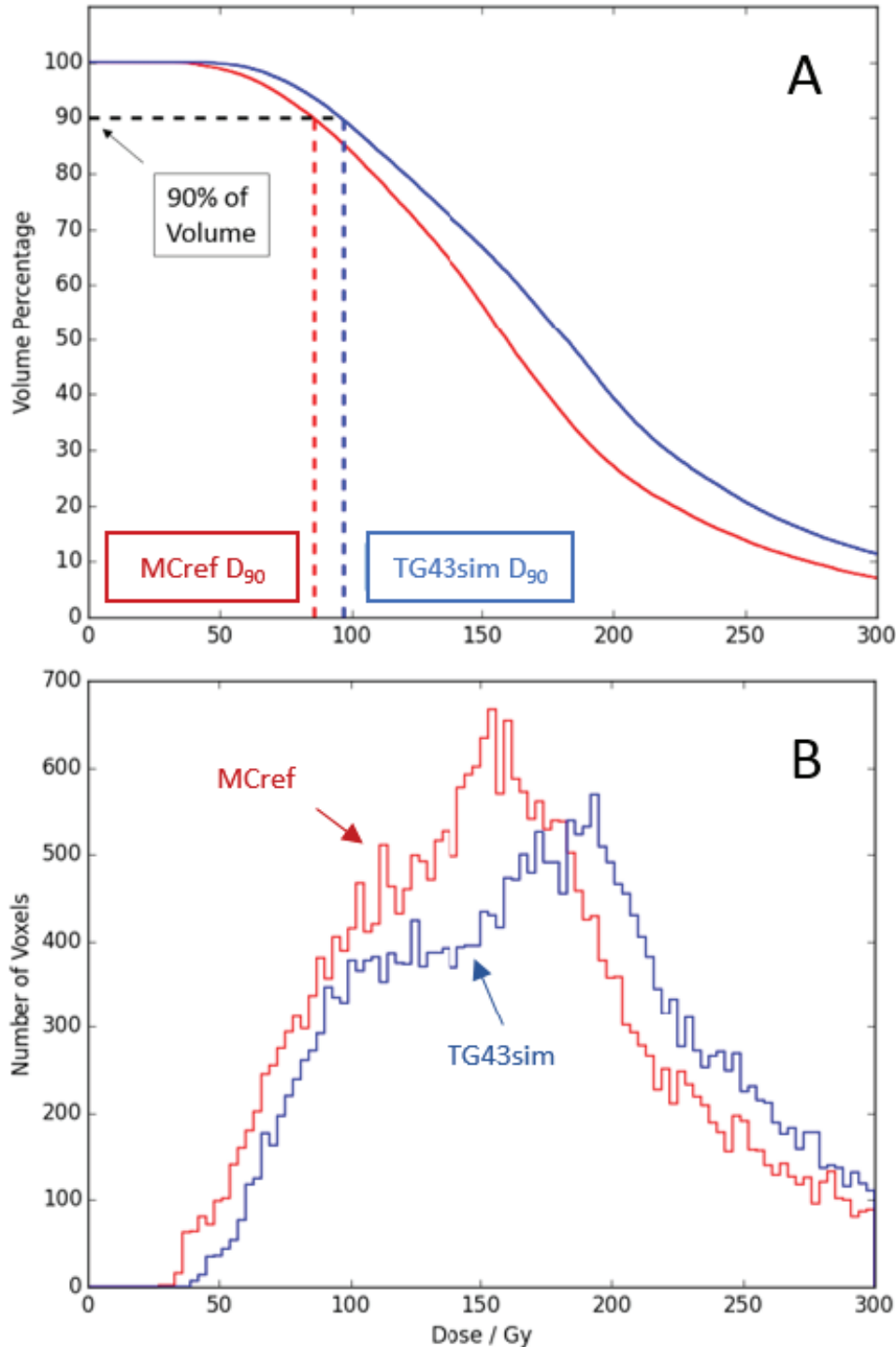


Figure 3.2: (A) Dose volume histogram for the $PTV0.5$ in patient #14. Differences in D_{90} value between MCref and TG43sim are indicated. (B) Differential dose volume histogram visualizing the change in $PTV0.5$ voxel dose between MCref and TG43sim for patient #14.

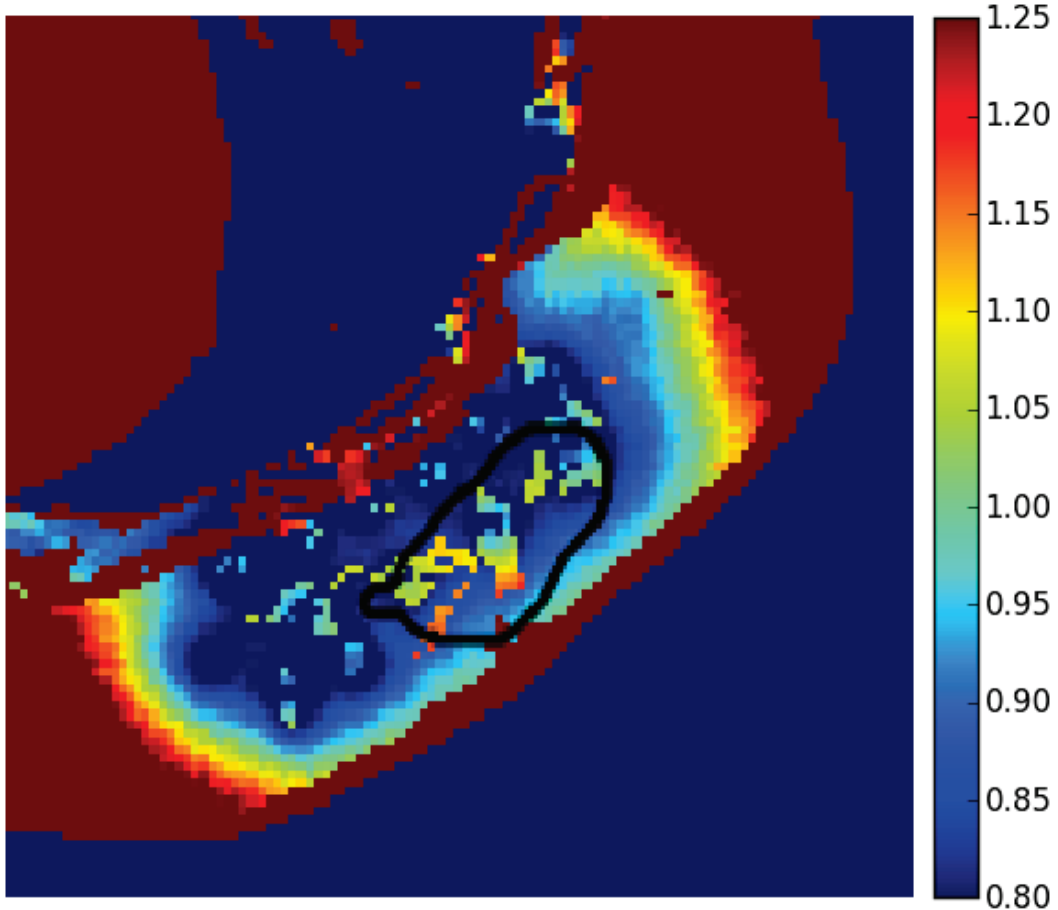


Figure 3.3: A colourwash of MCref/TG43sim dose ratios. The $PTV_{0.5}$ is outlined in black. For clarity in the skin and target regions, air and lung doses have been set to zero. The scale of the dose ratio difference has been changed from Figure 3.1 to emphasize dose ratio differences in gland.

comparable than adipose or gland (Figure 1.2), with skin μ_{en}/ρ being just 7% lower (skin and water μ_{en}/ρ values are 0.459 and 0.496 cm^2/g respectively at 20.7 keV). Decreased breast μ/ρ in MCref leads to fewer photon interactions occurring in the breast tissue. While this lowers target doses, reducing photon attenuation in the tissues located between the seeds and the skin results in an increased photon fluence reaching the skin region. This increases the dose delivered to the skin. Lastly, another change in photon fluence is caused by the existence of an air interface on the patient exterior in MCref. The presence of air with its low density results in reduced photon backscatter when compared to the water present in TG43sim. Thus, the final change in MCref skin

Table 3.1: Summary of dose metrics for MCref and TG43sim virtual models in patient #14.

Dose Metric	MCref	TG43sim	%Δ
$CTV D_{90}$ [Gy]	121.35	130.70	-7.70
$PTV0.5 D_{90}$ [Gy]	85.8	96.55	-12.52
$PTV1.0 D_{90}$ [Gy]	56.75	65.80	-15.94
$PTV0.5 V_{90}$	0.916	0.951	-3.76
$PTV0.5 V_{100}$	0.883	0.924	-4.61
$PTV0.5 V_{150}$	0.665	0.742	-11.70
$PTV1.0 V_{200}$	0.383	0.525	-37.33
Skin D_{1cm^2} [Gy]	116.5	91.1	21.80
Rib Volume > 90 Gy [cm^3]	2.97	0	100.0
Lung V_{10}	0.0894	0.0687	23.2
Heart D_{1cm^2}	7.19	6.21	13.6

dose compared with TG43sim is a result of the interplay of three factors: an increased fluence from lower breast μ/ρ , the decreased backscatter from the air interface, and the decreased energy deposition due to skin μ_{en}/ρ . When all these variables are considered for patient #14, the increased fluence from low breast μ/ρ dominates, increasing collision kerma (Eq. (1.3)), which results in a higher skin dose in MCref, as seen by the yellow/red skin voxels in Figure 3.1.

Increases in dose due to MCref modeling (compared to TGsim) are large in the ribs and chest wall (Table 3.1). Similarly to the skin, accurate breast tissue assignment leads to an increased photon fluence in the chest wall/rib region. Combined with the high density and mass-energy absorption coefficients of cortical bone, energy deposition is substantially increased, causing large increases in MCref rib metrics when compared to TG43sim simulations. As the ribs and chest wall share many of the same voxels, a similar effect occurs in the chest wall. For the heart and lungs, differences in fluence existing between the MCref and TG43sim models again causes increased energy deposition in MCref (Table 3.1).

Now that the dosimetric differences between MCref and TG43sim have been established in-depth for a single example patient, the study can be expanded to look at the full patient cohort. Although the trends in dose difference seen in patient #14 consistently repeat themselves across the patient cohort, these differences can vary greatly patient-by-patient, justifying the need for a larger statistical sample size.

3.1.1 Cohort target dose metrics

In all three target regions (*CTV*, *PTV0.5*, and *PTV1.0*), TG43sim consistently overestimates the dose delivered by PBSI treatments (Figure 3.4 and Table 3.2). As previously explained, these differences are largely caused by the assignment of low μ_{en}/ρ adipose and gland in the MCref breast, in addition to attenuation caused by seed material. In the *CTV*, TG43sim D₉₀ values are higher than those found using MCref in 34/35 patients. Differences in *CTV* D₉₀ between MCref and TG43sim values have large variations between patients, with differences ranging from 0.14% to 25.6%. In larger target regions (*PTV0.5* and *PTV1.0*), differences between MCref and TG43sim are even more pronounced across the whole patient cohort; TG43sim overestimates D₉₀ by 14.1% (*PTV0.5*) and 14.3% (*PTV1.0*) on average, representing differences in absolute target dose of 13.4 and 9.8 Gy respectively.

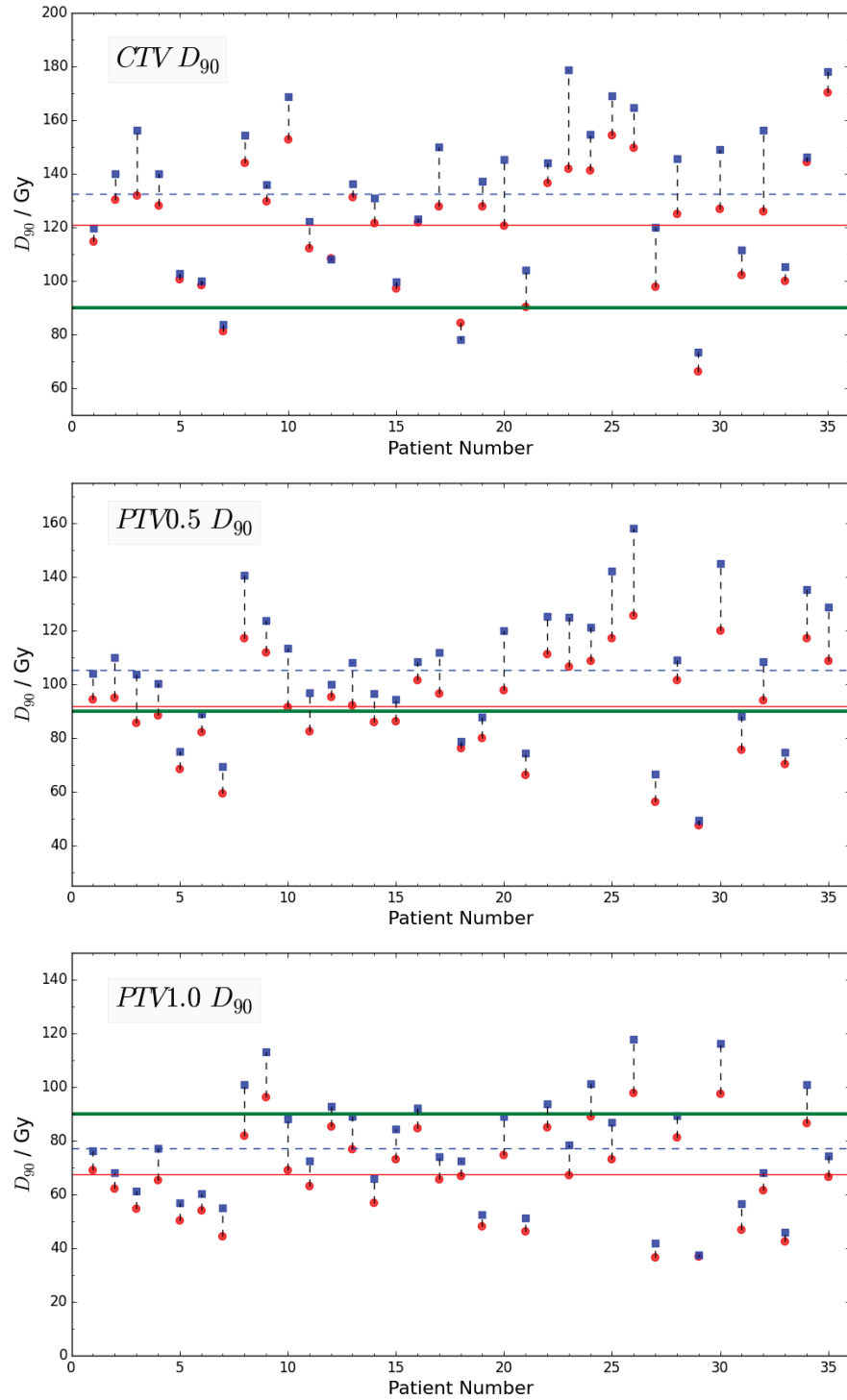


Figure 3.4: D_{90} values generated using MCref (red, circle) and TG43sim (blue, square) models. Individual patient D_{90} for CTV , $PTV0.5$, and $PTV1.0$ are presented, along with lines indicating the prescription dose (green), mean TG43sim D_{90} (blue, dashed), and mean MCref D_{90} (red, solid).

Table 3.2: Individual patient D_{90} values (in Gy) for the CTV , $PTV0.5$, and $PTV1.0$ for simulations of MCref and TG43sim (TG43). Percentage differences between models is stated by $\% \Delta$. Mean and standard deviation values across the whole cohorts are given for D_{90} and $\% \Delta$. Performing a paired t-test, p-values are below 0.05 for all cases, indicating the models are different with 95% confidence.

Pt. #	$CTV D_{90}$			$PTV0.5 D_{90}$			$PTV1.0 D_{90}$		
	MCref	TG43	$\% \Delta$	MCref	TG43	$\% \Delta$	MCref	TG43	$\% \Delta$
1	114.6	119.4	-4.19	94.3	104.0	-10.23	68.9	76.0	-10.31
2	130.1	139.8	-7.46	94.7	109.8	-15.95	61.9	67.9	-9.61
3	131.6	156.2	-18.66	85.5	103.8	-21.35	54.5	61.2	-12.29
4	127.9	140.0	-9.46	88.4	100.1	-13.24	65.3	77.0	-17.84
5	100.5	102.7	-2.19	68.3	74.8	-9.60	50.3	56.7	-12.62
6	98.2	99.8	-1.68	82.1	89.0	-8.41	54.0	60.1	-11.20
7	81.0	83.7	-3.40	59.3	69.2	-16.69	44.3	54.8	-23.84
8	143.9	154.3	-7.26	117.0	140.4	-19.96	81.6	100.8	-23.53
9	129.6	135.8	-4.79	111.7	123.7	-10.70	96.2	112.9	-17.36
10	152.7	168.5	-10.35	91.3	113.4	-24.15	69.0	88.0	-27.63
11	112.1	122.0	-8.84	82.5	96.6	-17.16	63.1	72.4	-14.75
12	108.2	108.1	0.14	95.2	99.8	-4.83	85.2	92.8	-8.98
13	131.3	136.2	-3.77	92.2	107.9	-17.04	76.8	89.0	-15.82
14	121.4	130.7	-7.70	85.8	96.6	-12.53	56.8	65.8	-15.95
15	97.1	99.5	-2.42	86.1	94.3	-9.52	73.0	84.2	-15.34
16	121.8	123.1	-1.07	101.5	108.2	-6.55	84.7	92.0	-8.62
17	127.8	149.8	-17.26	96.5	111.9	-15.97	65.5	73.8	-12.76
18	84.3	78.0	7.42	76.0	78.7	-3.55	66.6	72.4	-8.71
19	127.6	137.1	-7.45	80.0	87.8	-9.75	48.1	52.5	-9.16
20	120.4	145.3	-20.68	97.8	119.9	-22.55	74.6	89.1	-19.37
21	90.1	103.8	-15.27	66.0	74.3	-12.59	46.3	51.2	-10.70
22	136.6	143.9	-5.35	111.3	125.2	-12.49	84.8	93.6	-10.44
23	141.8	178.5	-25.88	106.4	125.0	-17.49	67.0	78.3	-16.88
24	141.0	154.5	-9.61	108.6	121.1	-11.52	88.8	101.2	-13.96
25	154.1	168.9	-9.57	117.0	142.1	-21.46	73.1	86.8	-18.74
26	149.5	164.6	-10.14	125.5	158.1	-26.03	97.6	117.8	-20.71
27	97.7	119.8	-22.63	56.3	66.6	-18.31	36.6	41.9	-14.50
28	124.9	145.5	-16.54	101.6	108.9	-7.19	81.0	89.4	-10.38
29	66.2	73.3	-10.73	47.3	49.2	-4.02	36.9	37.5	-1.63
30	126.8	149.0	-17.51	119.7	144.7	-20.89	97.4	116.2	-19.36
31	102.1	111.5	-9.21	75.4	88.1	-16.92	46.9	56.6	-20.70
32	125.9	156.1	-24.00	94.0	108.3	-15.21	61.4	67.9	-10.50
33	100.0	105.1	-5.15	70.1	74.6	-6.35	42.5	45.9	-8.00
34	144.1	146.2	-1.46	117.0	135.3	-15.60	86.4	100.7	-16.56
35	170.3	178.0	-4.49	108.7	128.6	-18.36	66.4	74.1	-11.68
Mean	120.9	132.2	-9.10	91.7	105.1	-14.12	67.2	77.0	-14.30
σ	22.7	27.4	7.4	19.0	24.4	5.8	17.0	20.6	5.3

Target volume metrics also have clear systematic differences between TG43sim and MCref generated dose distributions (Table 3.3). In the four extracted volume metrics (V_{90} , V_{100} , V_{150} , V_{200}) across three target regions (CTV , $PTV0.5$, and $PTV1.0$), the TG43sim volume metric value is higher than its MCref counterpart in 99.5% of cases. A noticeable trend is that as the size of the targeted region grows (CTV to $PTV1.0$), so too does the discrepancy between the target metrics ($\% \Delta$). For example, the average $\% \Delta$ in $PTV1.0$ V_{150} (26.0%) values is larger than that for $PTV0.5$ V_{150} (17.6%), which is in turn greater than that in the CTV (8.3%). This is due to an increase in the proportion of adipose in the region considered (Table 2.2), as adipose has the lowest mass-energy absorption coefficient of any breast tissue.

Table 3.3: Mean cohort volume metrics for targeted regions in simulations of MCref and TG43sim.

Target Region	Metric	MCref	TG43sim	$\% \Delta$
CTV	V_{90}	0.983	0.986	-0.36
	V_{100}	0.967	0.975	-0.84
	V_{150}	0.782	0.848	-8.34
	V_{200}	0.448	0.554	-23.75
$PTV0.5$	V_{90}	0.926	0.951	-2.71
	V_{100}	0.894	0.928	-3.85
	V_{150}	0.637	0.748	-17.56
	V_{200}	0.341	0.474	-38.92
$PTV1.0$	V_{90}	0.823	0.871	-5.84
	V_{100}	0.775	0.835	-7.71
	V_{150}	0.495	0.624	-26.03
	V_{200}	0.260	0.382	-47.15

3.1.2 Cohort normal tissue dose metrics

As the skin is the healthy organ most likely to develop negative side-effects from incidental dosage during PBSI treatments, accurate skin dosimetry is of particular importance. Two dose metrics, peak skin dose and D_{1cm^2} , are extracted in an attempt to quantify the skin dose levels caused by PBSI treatments (Figure 3.5). Peak skin dose, defined as

the highest dose received by a single skin voxel, varies dramatically between patients, ranging from 7.5 Gy (Patient #2) to 892 Gy (Patient #8) when using MCref (Table 3.7). These variations occur due to differences in patient anatomy and implant location, as large differences in breast size and tumour-skin proximity exist. Differences between TG43sim and MCref peak skin doses show different trends depending on the absolute dose values involved (Figure 3.5). Patients receiving an extremely high peak skin dose (>200 Gy) often show a decrease in peak dose when a MCref tissue assignment scheme is used (relative to the TG43sim scheme). High skin dose voxels result from treatments with seeds located directly beside the skin. In these cases, the slight increase in $(\mu_{en}/\rho)_{water}$ compared to $(\mu_{en}/\rho)_{skin}$ is more impactful than the increased photon fluence resulting from lower density and μ_{en}/ρ breast tissue. Patients with seeds located further from the skin have lower peak doses, but the increased photon fluence through the skin in MCref increases energy absorption by more than the small change in μ_{en}/ρ decreases it, leading to an overall increase in peak skin dose.

As peak skin doses can be affected by one anomalously high dose voxel, D_{1cm^2} is often seen as a more reliable assessment of patient skin dose. For this 35 patient cohort, the mean D_{1cm^2} skin value in a MCref model is 84.4 Gy (Table 3.7), almost equivalent to the prescribed treatment dose. MCref D_{1cm^2} values are higher than TG43sim D_{1cm^2} in all patients (Figure 3.5), with an average percentage increase of 22.2%. By considering an increased volume of skin, the dose increasing effects of greater photon fluence are always more substantial than the dose reducing effect of lower skin μ_{en}/ρ in MCref (compared to water in TG43sim).

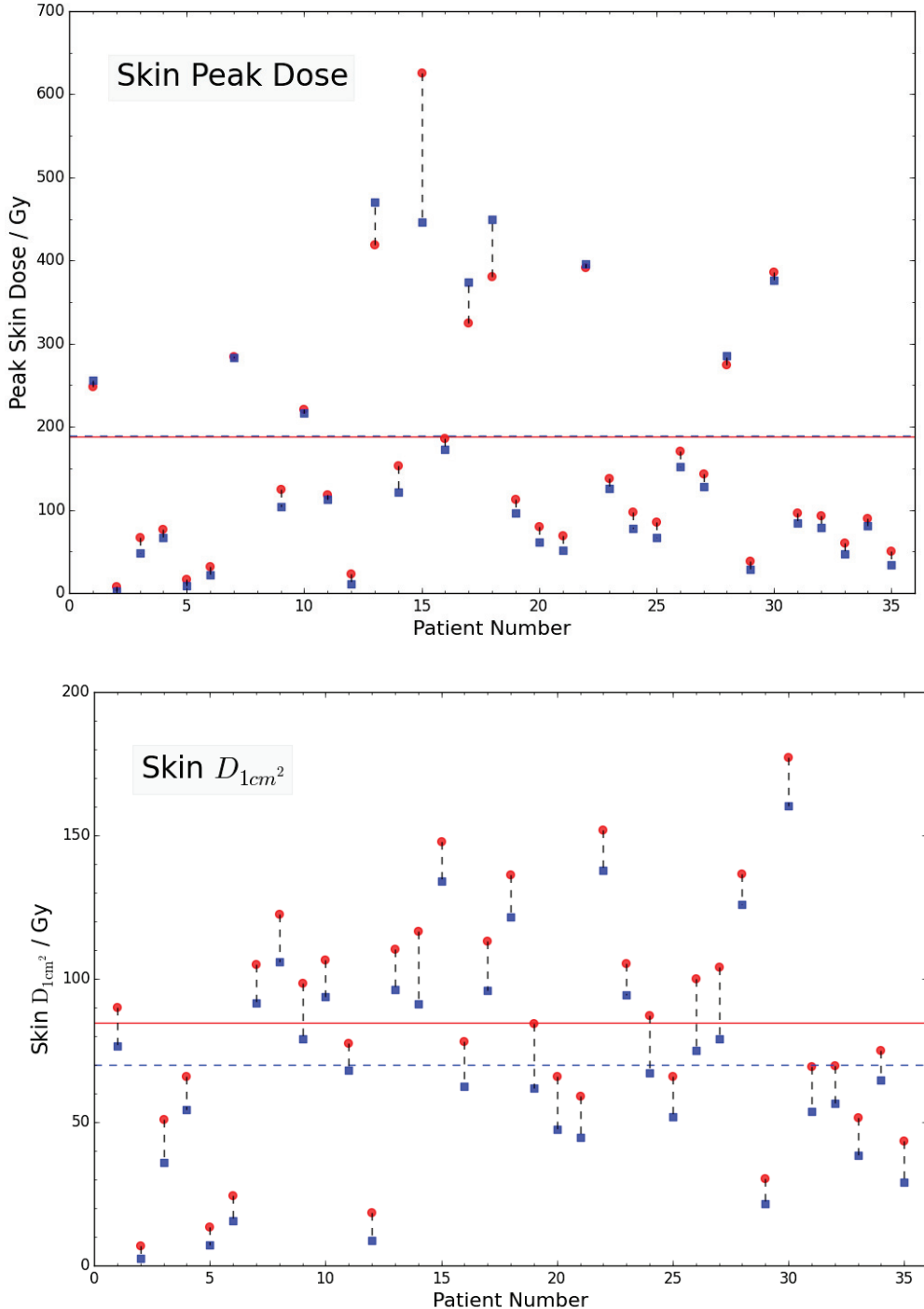


Figure 3.5: Comparison of skin dose metrics for all MCref (red, circle) and TG43sim (blue, square) modeled patients. Mean cohort values for MCref (red, solid) and TG43sim (blue, dashed) are given. For peak skin dose, patient #8 is above the visualized scale.

Table 3.4: Table of the individual patient skin dose metrics in simulations of MCref and TG43sim. Percentage differences between models is stated by $\% \Delta$. Mean and standard deviation values across the whole cohorts are given for D_{90} and $\% \Delta$. Performing a paired t-test, the obtained p-value is below 0.05 for the skin D_{1cm^2} , indicating a difference between models with 95% confidence. For peak skin dose, the p-value is large ($p=0.46$), so the same cannot be said.

Patient Number	Skin Peak Dose / Gy			Skin D_{1cm^2} / Gy		
	MCref	TG43sim	$\% \Delta$	MCref	TG43sim	$\% \Delta$
1	248.2	256.1	-3.2	89.8	76.3	15.0
2	7.5	2.7	64.4	6.6	2.2	66.5
3	66.5	48.6	27.0	50.8	35.8	29.5
4	76.6	66.8	12.9	65.6	54.2	17.4
5	16.6	9.1	45.0	13.1	7.1	46.1
6	31.8	21.6	32.2	24.3	15.6	36.0
7	284.0	283.7	0.1	105.0	91.5	12.8
8	891.9	1287.4	-44.3	122.3	105.8	13.5
9	124.9	103.5	17.1	98.2	79.0	19.6
10	220.8	216.1	2.1	106.4	93.7	11.9
11	117.9	112.1	4.9	77.3	68.1	12.0
12	23.2	11.1	51.9	18.3	8.5	53.3
13	418.6	469.8	-12.2	110.3	96.1	12.8
14	152.8	121.5	20.5	116.5	91.1	21.8
15	626.2	446.0	28.8	147.7	133.8	9.4
16	185.7	172.7	7.0	78.0	62.4	20.1
17	325.1	373.7	-14.9	113.0	95.6	15.3
18	381.0	449.6	-18.0	136.1	121.4	10.8
19	112.3	96.1	14.4	84.2	61.9	26.5
20	80.3	61.7	23.2	65.7	47.2	28.1
21	68.6	51.6	24.9	58.9	44.4	24.5
22	392.0	395.7	-0.9	151.8	137.7	9.3
23	138.0	126.0	8.7	105.3	94.1	10.6
24	97.1	77.2	20.5	87.1	67.2	22.9
25	85.8	66.9	22.0	65.7	51.6	21.5
26	170.2	152.0	10.7	99.9	74.9	25.0
27	143.7	127.9	11.0	103.8	78.9	23.9
28	274.7	285.8	-4.0	136.5	125.7	7.9
29	38.6	28.1	27.2	30.0	21.5	28.4
30	386.6	376.5	2.6	176.9	160.0	9.6
31	95.8	84.0	12.3	69.2	53.5	22.7
32	93.3	78.7	15.7	69.5	56.4	18.9
33	59.8	46.5	22.3	51.3	38.4	25.1
34	89.7	80.9	9.8	74.8	64.5	13.8
35	50.5	34.3	32.0	43.3	29.0	33.1
Mean	187.9	189.2	13.5	84.4	69.9	22.2
σ	184.4	234.2	20.0	40.3	38.3	12.7

Fifteen additional metrics are extracted from the MCref and TG43sim models to provide dosimetric information about the ribs, chest wall, breast, heart, lung, and the body as a whole (Table 3.5).

Table 3.5: Mean values of dose metrics over patient cohort for regions of interest in simulations of MCref and TG43sim models.

Region	Metric	MCref	TG43sim	$\% \Delta$
Ribs	Peak Dose [Gy]	746.32	168.81	77.38
	Volume > 90 Gy [cm ³]	2.99	0.48	83.92
Chest Wall	Peak Dose [Gy]	927.03	693.32	25.21
	Volume > 90 Gy [cm ³]	8.44	4.84	42.67
Breast	V_{150} [cm ³]	33.02	44.53	-34.86
	V_{200} [cm ³]	16.86	25.92	-53.69
Heart	V_{10} [%]	0.00	0.00	0.00
	V_{50} [%]	0.00	0.00	0.00
	Mean Dose [Gy]	0.19	0.08	60.74
	D_{1cm^2} [Gy]	4.38	2.05	53.26
Lung	V_5 [Fraction]	0.071	0.040	45.36
	V_{20} [Fraction]	0.0076	0.0073	5.89
Full Body	HI	0.365	0.257	16.4
	CI	0.451	0.470	-4.31
	V_{100} [cm ³]	70.54	76.32	-8.20

In the ribs and chest wall, peak doses are extracted, along with the volume (in cubic centimeters) of tissue receiving above 90 Gy of dose, with large discrepancies seen between the MCref and TG43sim dose metrics (Figure 3.6). Average patient rib (chest wall (Figure 3.7)) peak doses increase by 577 Gy (238 Gy) in MCref. The average volume above 90 Gy in the ribs (chest wall) increases by 83.9% (42.7%).

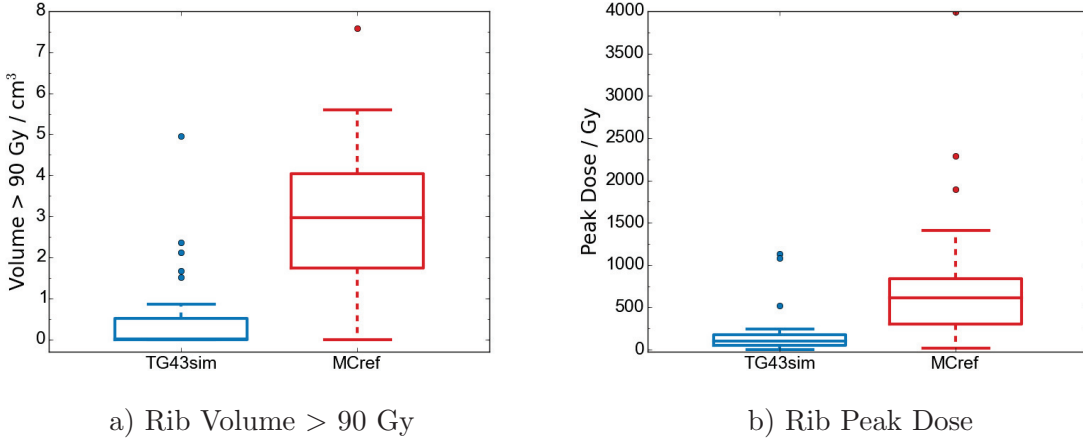


Figure 3.6: Box and whisker plots (boxplots) showing the distribution of patient rib dose metrics for TG43sim and MCref simulations. The median metric value is indicated as the box central line, along with the upper and lower quartiles. Outliers, defined as being outside the upper/lower quartile by more than 1.5 times the inner quartile range (upper minus the lower quartile), are displayed as individual points.

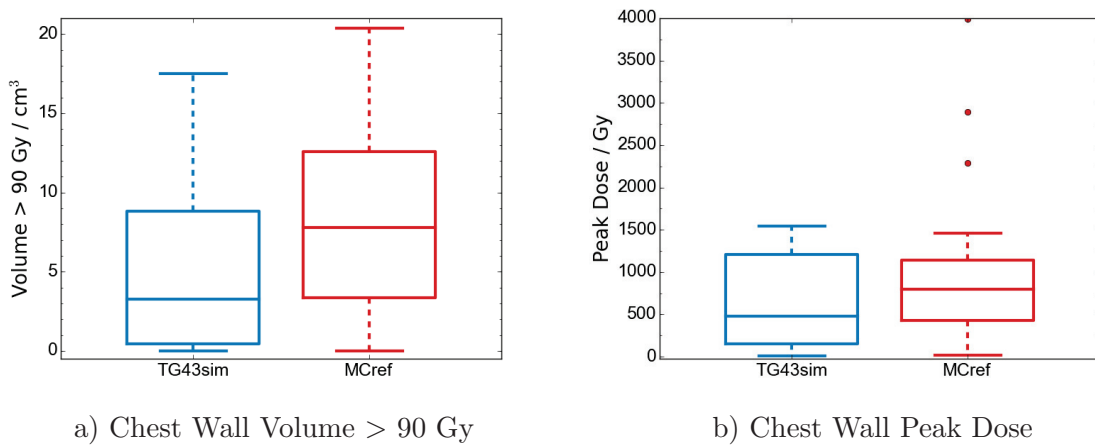


Figure 3.7: Chest wall dose metrics. See caption of Fig. 3.6 for an explanation of box and whiskers.

Heart doses are usually very low in BCCA PBSI treatments (Figure 3.8). No heart tissue voxel in any patient receives more than 50% (45 Gy) of the prescribed dose (V_{50}). Very few patients (6/35) have non-zero V_{10} measurements, with the highest recorded V_{10} fraction being only 0.007. While TG43sim mean heart dose levels are still quite low (0.01 - 0.45 Gy), accounting for accurate tissue modeling and seed geometries in MCref causes increases in mean heart dose of 12 - 93%. MCref heart D_{1cm^2} metrics are greater than those in TG43sim in all patients, by an average of 53.3%.

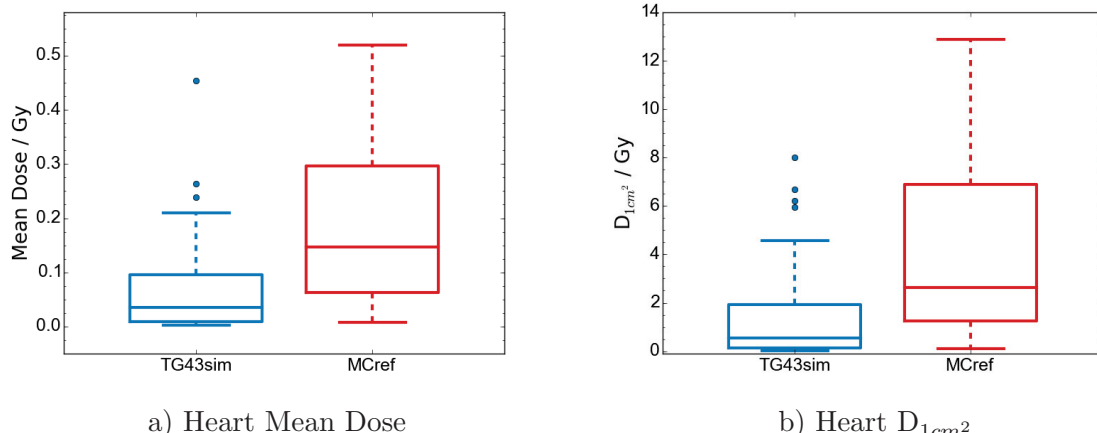


Figure 3.8: Heart dose metrics. See caption of Fig. 3.6 for an explanation of box and whiskers.

Distinguishing between patients with a left or right breast PBSI treatment provides additional information about heart dose, as seen in Figure 3.9. For both TG43sim and MCref models, patients with implants in their left breast consistently receive a higher mean heart dose. For right breast Pd-103 implants, percent differences between TG43sim and MCref heart doses are larger, caused by an increased distance between sources and the heart (when compared to left breast implants).

Doses to the lung are also very small. Extracted V_5 and V_{20} metrics see significant increases (45.4 and 5.9% on average) in the transition from TG43sim to MCref patient models, but the corresponding mean MCref V_5 and V_{20} values are very low, at only

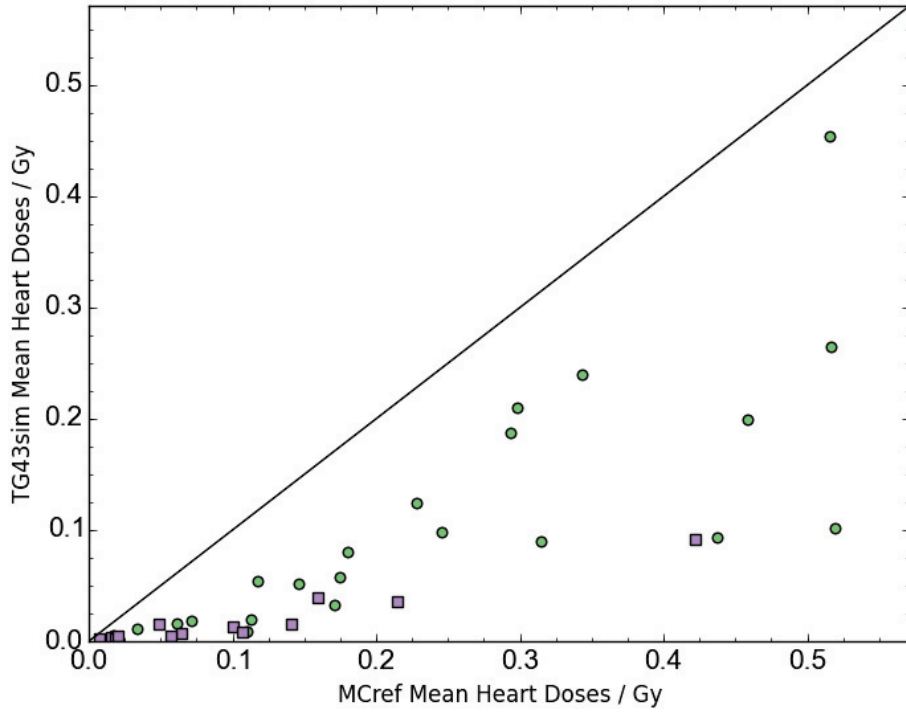


Figure 3.9: Scatter plot of the mean heart doses for MCref and TG43sim models. The plotted points distinguish between PBSI patients treated on the left (green, circular) or right (square, purple) breast. A diagonal line illustrates equivalent MCref and TG43sim metric values.

0.071 and 0.0076 respectively (Figure 3.10).

V_{150} and V_{200} metrics are calculated for the entire treated breast, as opposed to just the immediate lumpectomy region of the CTV , $PTV0.5$, and $PTV1.0$ (Figure 3.11). These metrics also are presented as the total volume exceeding the dose threshold, rather than a fractional value. As with the targeted regions, differences in density and μ_{en}/ρ cause TG43sim models to considerably overestimate volume metric values. Differences of up to 53% (V_{150}) and 68% (V_{200}) occur between the two models. A full body V_{100} metric is also calculated, accounting for all non-air tissue in the patient model. Full body V_{100} is also consistently overestimated by TG43sim, but by a smaller amount than

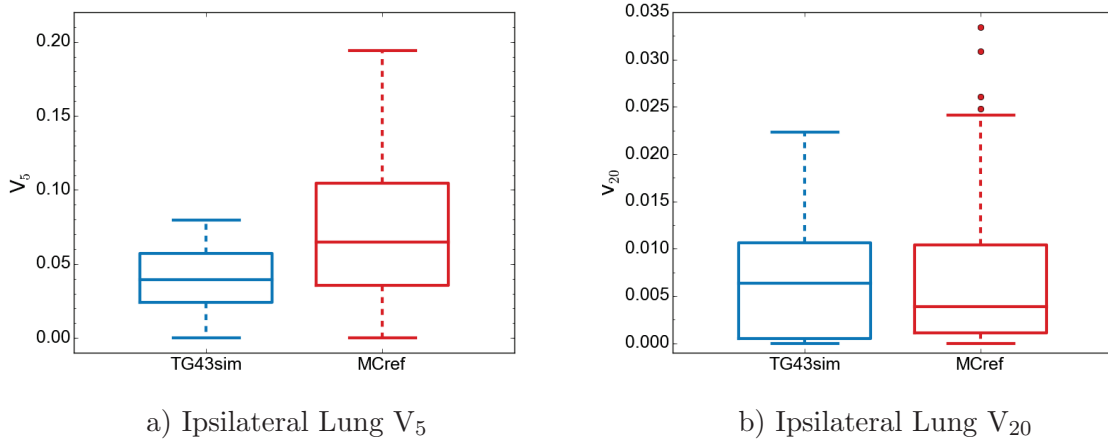


Figure 3.10: Ipsilateral lung dose metrics. See caption of Fig. 3.6 for an explanation of box and whiskers.

most volume metrics (8.3% on average).

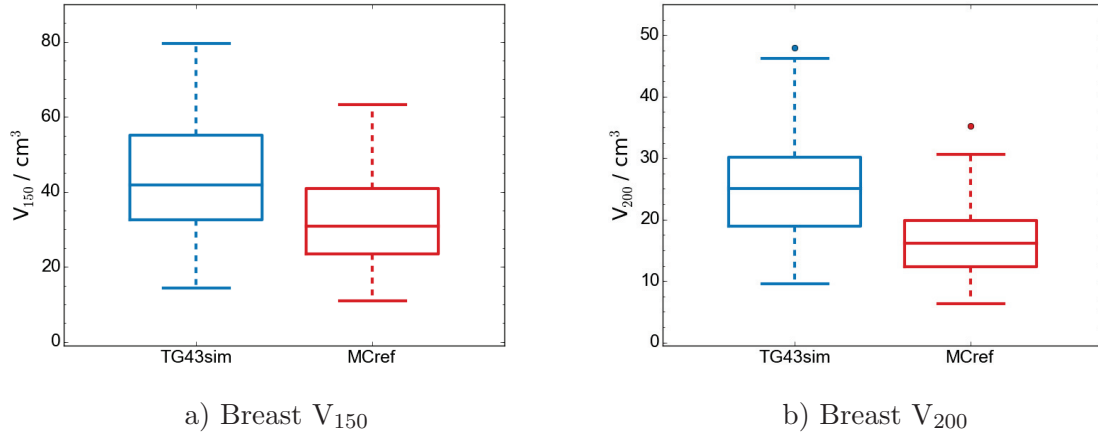


Figure 3.11: Full breast dose metrics. See caption of Fig. 3.6 for an explanation of box and whiskers.

Conformity and homogeneity indices are extracted (Figure 3.12 and Figure 3.13).

Across the whole patient cohort, TG43sim underestimates the homogeneity index by 7.2 - 31.1 %. The conformity index is not as predictable, with several MCref patient models showing lower CI values than in the TG43sim model. $\% \Delta$ values in conformity indices are also usually less than those seen in homogeneity indices, ranging from -6.0 to 10.5%. As these indices are functions of other dose metrics, their differences can be described

in terms of the component metrics. Increased TG43sim conformity indices (defined in Section 2.6) are due to the increases in TG43sim $PTV0.5 V_{100}$ values being more substantial than the accompanying increase in Full Body V_{100} . For the homogeneity index, the increase in $PTV0.5 V_{150}$ value is proportionally larger than that of $PTV0.5 V_{100}$ when TG43sim simulations are considered instead of MCref. This causes the ratio of $PTV0.5 V_{150}$ over V_{100} to increase in TG43sim simulations (compared to MCref), reducing the value of HI and creating notable differences between MCref and TG43sim .

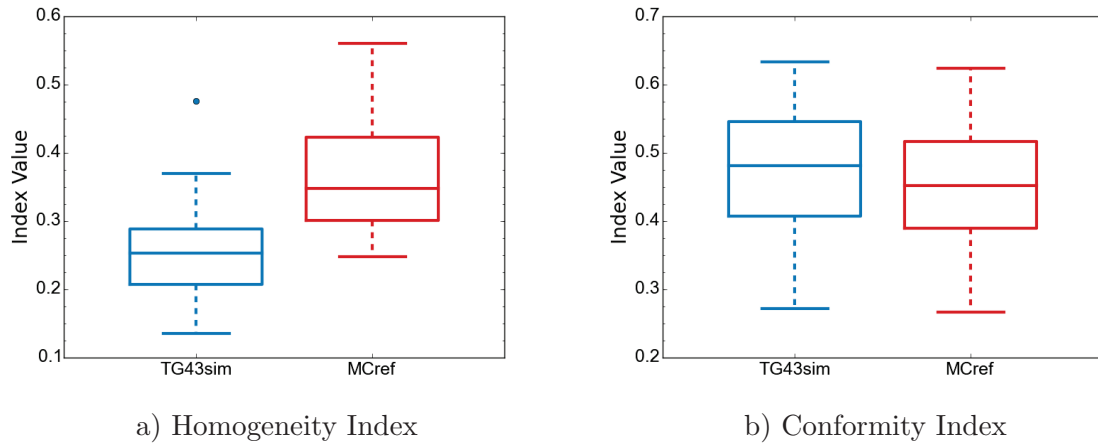


Figure 3.12: Homogeneity and conformity indices. See caption of Fig. 3.6 for an explanation of box and whiskers.

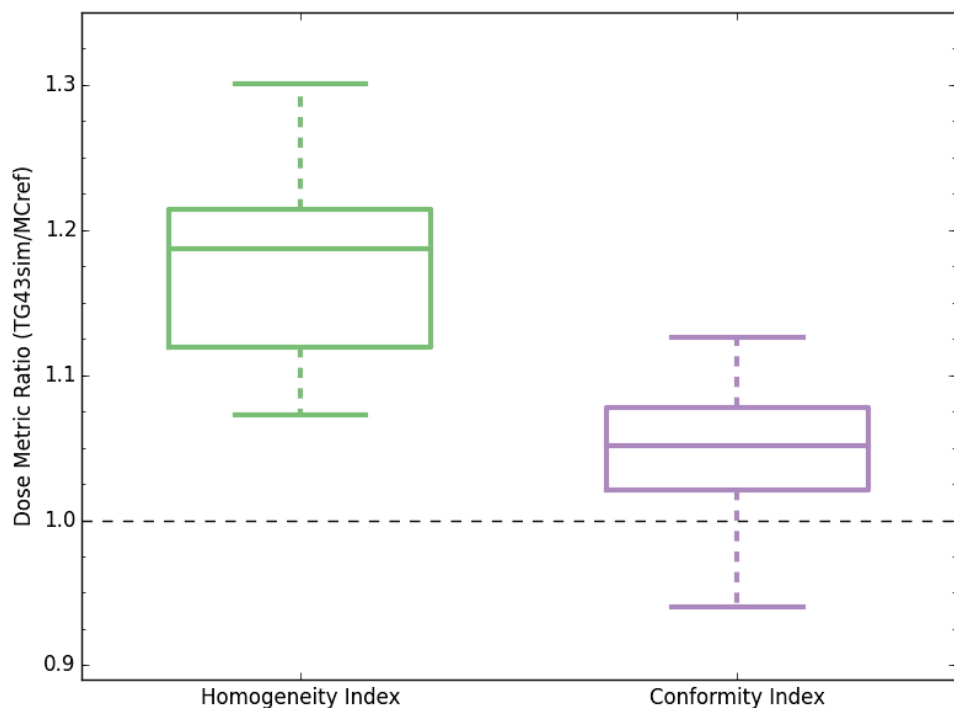


Figure 3.13: Boxplots of the patient-by-patient ratios of TG43sim and MCref homogeneity and conformity indices for the whole patient cohort. See caption of Fig. 3.6 for an explanation of box and whiskers.

3.2 Sensitivity to modeling choices

For the investigation into the sensitivity of dose distributions to changes in patient and treatment modeling, target and skin dose metrics are primarily emphasized, as they represent the most clinically relevant regions. In cases where other metrics provide particular insight, they are provided as well.

3.2.1 Adipose / Gland segmentation

In all three targeted regions, differences between MCfixed and MCref generated D₉₀ metrics are small. In the *PTV0.5 (CTV, PTV1.0)*, the mean absolute difference between the D₉₀ values is just 1.46% (1.16%, 0.68%). A few patients do show differences between the MCfixed and MCref models of greater than 3%, but only 2/105 of the total examined D₉₀ values (3 target regions across 35 patients) differ by more than 5%.

Table 3.6: Dose metrics for targeted regions in simulations of MCref and MCfixed

Pt #	CTV D ₉₀			PTV0.5 D ₉₀			PTV1.0 D ₉₀		
	MCref	MCfixed	%Δ	MCref	MCfixed	%Δ	MCref	MCfixed	%Δ
1	114.6	114.9	-0.22	94.3	94.6	-0.32	68.9	69.2	-0.51
2	130.1	131.9	-1.42	94.7	96.0	-1.37	61.9	62.2	-0.48
3	131.6	129.0	2.01	85.5	84.2	1.52	54.5	54.6	-0.18
4	127.9	128.0	-0.12	88.4	89.2	-0.91	65.3	65.6	-0.38
5	100.5	101.0	-0.55	68.3	69.5	-1.83	50.3	51.3	-1.89
6	98.2	97.5	0.66	82.1	84.0	-2.38	54.0	54.4	-0.74
7	81.0	80.5	0.62	59.3	61.3	-3.29	44.3	44.9	-1.36
8	143.9	147.2	-2.33	117.0	122.4	-4.62	81.6	82.8	-1.41
9	129.6	128.4	0.89	111.7	109.1	2.33	96.2	96.0	0.26
10	152.7	152.6	0.07	91.3	94.4	-3.34	69.0	69.8	-1.16
11	112.1	112.0	0.09	82.5	83.1	-0.73	63.1	63.1	0.00
12	108.2	107.3	0.83	95.2	93.6	1.68	85.2	84.4	0.94
13	131.3	130.8	0.34	92.2	91.9	0.27	76.8	76.9	-0.13
14	121.4	121.6	-0.16	85.8	86.3	-0.52	56.8	57.0	-0.35
15	97.1	97.3	-0.15	86.1	86.1	0.00	73.0	73.0	0.00
16	121.8	121.7	0.08	101.5	101.1	0.44	84.7	84.6	0.12
17	127.8	129.9	-1.64	96.5	96.7	-0.26	65.5	65.7	-0.31
18	84.3	82.8	1.72	76.0	75.0	1.32	66.6	65.2	2.18
19	127.6	127.6	0.04	80.0	78.6	1.75	48.1	47.5	1.25
20	120.4	120.6	-0.12	97.8	98.7	-0.87	74.6	74.7	-0.07
21	90.1	87.8	2.50	66.0	64.2	2.65	46.3	46.7	-0.86
22	136.6	136.2	0.29	111.3	109.7	1.39	84.8	83.6	1.42
23	141.8	141.3	0.39	106.4	106.0	0.33	67.0	66.8	0.22
24	141.0	132.8	5.82	108.6	105.8	2.58	88.8	88.7	0.17
25	154.1	152.4	1.14	117.0	113.0	3.38	73.1	72.1	1.44
26	149.5	147.6	1.24	125.5	123.7	1.43	97.6	97.2	0.36
27	97.7	96.3	1.43	56.3	56.0	0.44	36.6	36.6	0.00
28	124.9	126.2	-1.08	101.6	102.2	-0.59	81.0	81.3	-0.37
29	66.2	66.0	0.30	47.3	46.8	1.06	36.9	36.6	0.81
30	126.8	136.5	-7.69	119.7	121.9	-1.84	97.4	96.6	0.77
31	102.1	102.6	-0.44	75.4	75.7	-0.46	46.9	47.0	-0.32
32	125.9	122.1	2.98	94.0	92.1	2.07	61.4	60.7	1.22
33	100.0	100.4	-0.40	70.1	70.5	-0.50	42.5	42.7	-0.35
34	144.1	145.0	-0.62	117.0	114.1	2.52	86.4	84.9	1.68
35	170.3	170.4	-0.03	108.7	108.9	-0.18	66.4	66.5	-0.15

However, despite small average differences between MCref and MCfixed target D₉₀ values, a trend can be extracted from the results. As shown in Figure 3.14, the further away the patient's individual adipose-gland cutoff (used in MCref) is from the constant 0.9476 g cm⁻³ boundary (used in MCfixed), the greater the difference in D₉₀ value. The extra assignment of gland or adipose (depending on if the boundary is increased or decreased) to the target region results in a small, but fairly predictable change in D₉₀ value.

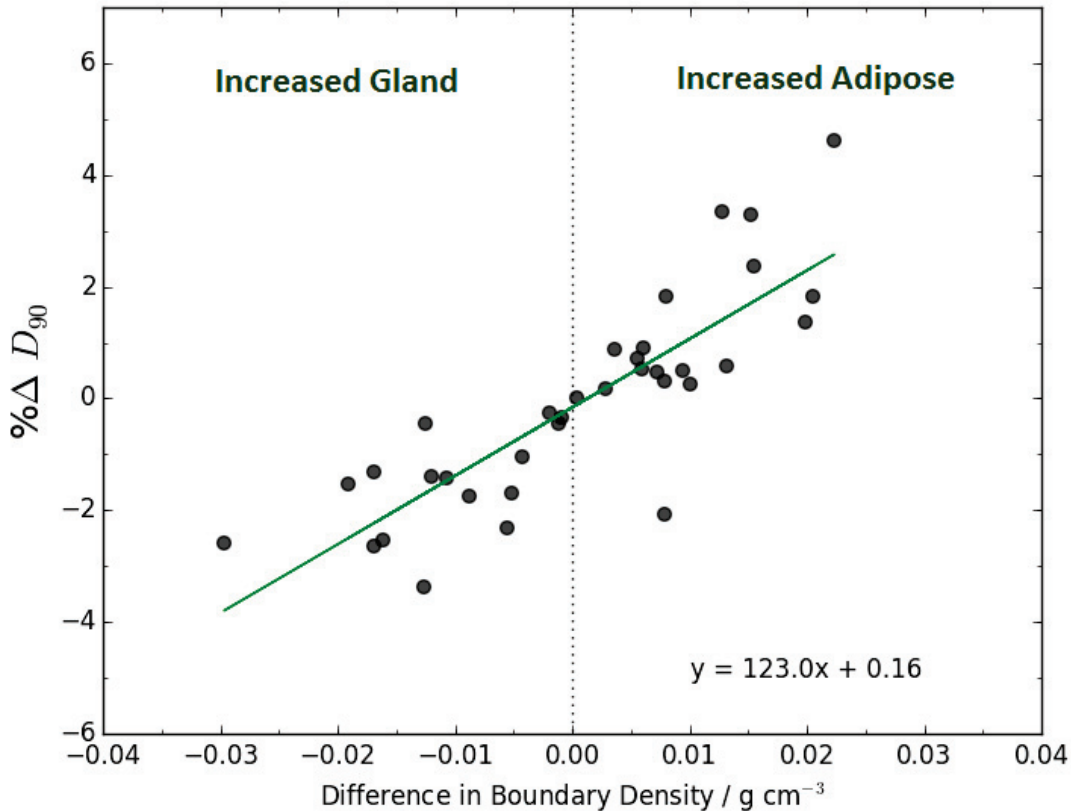


Figure 3.14: Changes in PTV0.5 D₉₀ due to differences in adipose-gland segmentation boundaries between MCref (variable density) and MCfixed (0.9476 g cm⁻³)

CTV volume metrics, along with PTV0.5 and PTV1.0 V₉₀ and V₁₀₀ metrics, follow the same pattern as D₉₀ values. Small sub-2% differences occur between MCfixed and MCref. These small differences are moderately predictable on a patient-by-patient basis,

with larger differences in the adipose-gland boundary creating larger changes in $\% \Delta V_x$ between MCref and MCfixed. Higher dose target volume metrics, V_{150} and V_{200} , do begin to show considerable discrepancies, especially in the larger target regions (Figure 3.15). $PTV0.5$ V_{150} and V_{200} values differ by up to 6.1% and 8.7% respectively, with differences in $PTV1.0$ V_{150} (V_{200}) of 6.8% (10.5%).

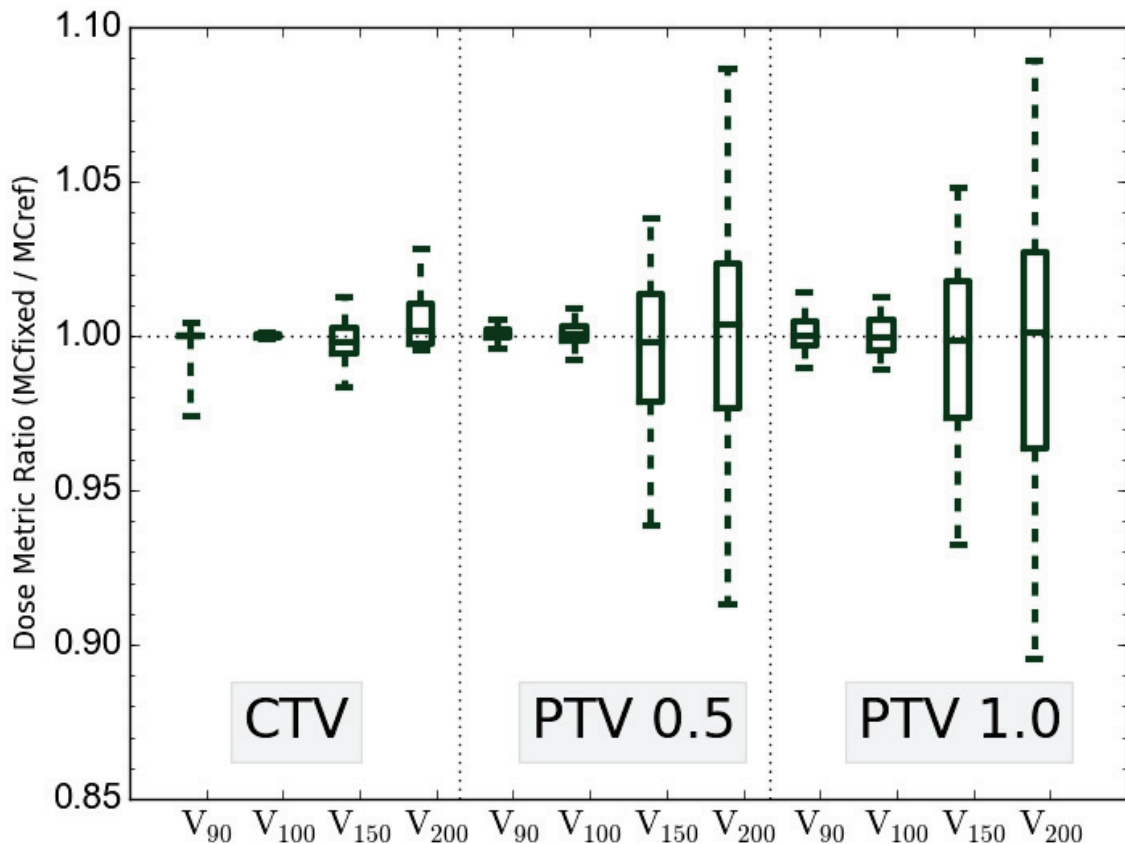


Figure 3.15: Boxplots of the patient-by-patient volume metric ratio. The changes in volume metrics are due to differences in adipose-gland boundaries between MCref (variable density) and MCfixed (0.9476 g cm^{-3})

A similar trend is seen in skin metrics. On a patient-by-patient basis, even smaller differences are seen between MCref and MCfixed peak dose and D_{1cm^2} metrics. The mean absolute percentage difference in peak dose (D_{1cm^2}) is just 1.07% (1.40%). Percentage differences between D_{1cm^2} values extracted from MCfixed and those extracted

from MCref are below 2% in 31 of 35 patients (Table 3.7). However, like D_{90} values, this difference in D_{1cm^2} metrics can still be correlated to a change in adipose-gland boundary density (Figure 3.16). Increasing the assignment of breast adipose directly reduces the number of photon interactions occurring in the breast. This causes a slight increase in the skin photon fluence, in turn increasing collision kerma and scored dose.

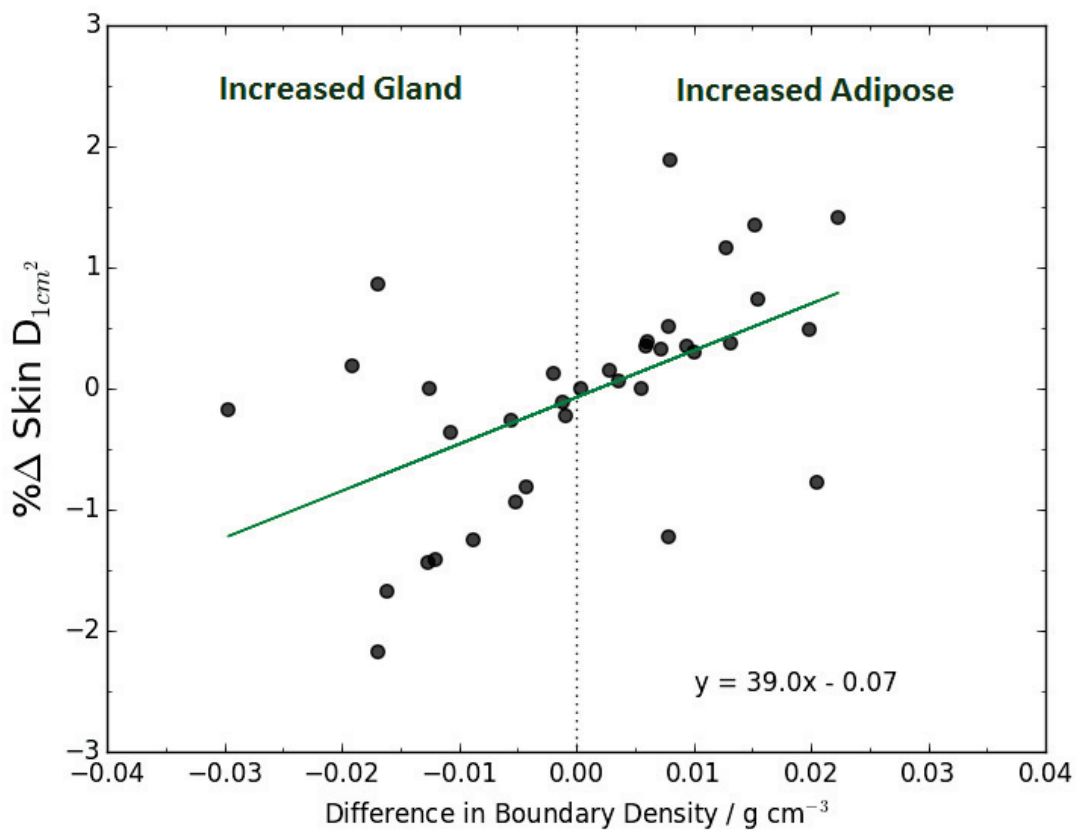


Figure 3.16: Changes in skin D_{1cm^2} due to differences in adipose-gland segmentation boundaries between MCref (variable density) and MCfixed (9476 g cm^{-3}).

Table 3.7: Skin dose metrics for MCref and MCfixed models

Patient Number	Skin Peak Dose / Gy			Skin D_{1cm^2} / Gy		
	MCref	MCfixed	% Δ	MCref	MCfixed	% Δ
1	248.2	247.4	0.33	89.8	89.3	0.56
2	7.5	7.3	2.72	6.6	6.4	3.34
3	66.5	67.0	-0.70	50.8	52.0	-2.45
4	76.6	76.2	0.54	65.6	65.2	0.65
5	16.6	16.6	-0.40	13.1	12.9	1.90
6	31.8	31.1	2.16	24.3	23.4	3.91
7	284.0	283.5	0.19	105.0	103.7	1.22
8	891.9	891.0	0.10	122.3	120.0	1.89
9	124.9	125.3	-0.38	98.2	98.6	-0.36
10	220.8	218.3	1.13	106.4	105.5	0.82
11	117.9	117.0	0.79	77.3	77.0	0.48
12	23.2	23.4	-0.88	18.3	18.5	-1.00
13	418.6	418.2	0.09	110.3	110.4	-0.11
14	152.8	150.4	1.59	116.5	115.7	0.72
15	626.2	626.2	0.00	147.7	147.6	0.09
16	185.7	186.6	-0.47	78.0	78.2	-0.19
17	325.1	323.3	0.58	113.0	111.6	1.22
18	381.0	382.1	-0.30	136.1	137.6	-1.07
19	112.3	113.9	-1.37	84.2	85.0	-0.94
20	80.3	79.9	0.57	65.7	65.5	0.19
21	68.6	70.6	-2.88	58.9	60.7	-3.03
22	392.0	392.9	-0.24	151.8	153.7	-1.24
23	138.0	137.6	0.29	105.3	105.4	-0.09
24	97.1	101.9	-4.92	87.1	90.7	-4.19
25	85.8	86.9	-1.37	65.7	66.8	-1.57
26	170.2	172.2	-1.19	99.9	101.4	-1.46
27	143.7	146.3	-1.79	103.8	105.9	-2.05
28	274.7	274.5	0.10	136.5	134.0	1.88
29	38.6	39.3	-1.83	30.0	30.5	-1.71
30	386.6	382.6	1.02	176.9	173.9	1.70
31	95.8	94.9	0.99	69.2	68.6	0.81
32	93.3	94.7	-1.45	69.5	71.3	-2.46
33	59.8	59.2	1.13	51.3	50.4	1.63
34	89.7	91.3	-1.75	74.8	76.2	-1.83
35	50.5	49.9	1.25	43.3	43.2	0.36

3.2.2 Seed orientation

To examine the effects of seed orientation in patient-specific MC modeling, dose metrics extracted from the MCref-z and MCref-45 patient dose distributions are compared to those extracted from MCref, where seeds are modeled at the angle of surgical needle insertion. Extracted D_{90} values are important to consider, so MCref, MCref-z, and MCref-45 D_{90} values are presented in the target ($PTV0.5$) for the whole cohort in Table 3.8. D_{90} differences between MCref and MCref-z are sizable for many patients, with a $\% \Delta D_{90}$ value of greater than 2% in over half of the cohort. MCref-45 D_{90} values are much closer to those extracted from MCref. Percentage differences in D_{90} of under 2% occur in 33 of 35 cases and the mean difference between a MCref-45 patient D_{90} and a MCfixed patient D_{90} is just 0.77% (Table 3.8). Patient #27 is an outlier, with D_{90} value differing by 7.02% between MCref and MCref-45.

Table 3.8: $PTV0.5 D_{90}$ metrics in simulations of MCref, MCref-45, and MCref-z

Patient Number	MCref [Gy]	MCref - Z		MCref - 45°	
		[Gy]	%Δ	[Gy]	%Δ
1	94.3	92.5	1.91	94.3	0.00
2	94.7	98.8	-4.28	94.7	0.05
3	85.5	86.1	-0.70	85.6	-0.12
4	88.3	85.2	3.62	88.5	-0.11
5	68.2	66.6	2.49	69.4	-1.61
6	82.0	81	1.28	82.5	-0.55
7	59.3	57.9	2.36	59.6	-0.51
8	117.0	118.1	-0.90	116.7	0.26
9	111.7	112.1	-0.36	111.5	0.18
10	91.3	95.2	-4.27	91.9	-0.60
11	82.4	83.9	-1.82	83.0	-0.67
12	95.2	94.3	1.00	93.5	1.79
13	92.1	86.2	6.51	92.2	0.00
14	85.8	84.2	1.92	85.8	0.06
15	86.1	79.5	7.67	85.6	0.64
16	101.5	98.7	2.76	102	-0.49
17	96.5	96.9	-0.41	96.8	-0.31
18	76	74.3	2.24	77.1	-1.45
19	80	81.9	-2.38	80.7	-0.88
20	97.8	93.7	4.24	97.9	-0.05
21	65.9	67.9	-2.96	65.8	0.30
22	111.3	110.5	0.67	111.0	0.22
23	106.4	102.9	3.24	105.0	1.27
24	108.6	104.7	3.55	108.6	-0.05
25	116.9	115.8	1.03	117.4	-0.38
26	125.5	126.3	-0.64	127.7	-1.79
27	56.3	59.4	-5.60	60.2	-7.02
28	101.6	101.7	-0.15	102.0	-0.44
29	47.3	46.8	1.06	45.9	2.96
30	119.7	114.5	4.34	119.8	-0.08
31	75.4	74.3	1.46	74.8	0.73
32	94	91.4	2.77	94.5	-0.48
33	70.1	72.2	-3.00	70.4	-0.36
34	117	115.9	0.94	116.8	0.17
35	108.7	105.4	2.99	108.2	0.41

For volume metrics, larger differences occur between MCref and the two alternatively angled models (Figure 3.17). Like many metrics, differences between the reference and alternative models increase as the dose level and the size of the target region being considered increases. Comparing MCref and MCref-z in the *PTV0.5*, this results in a mean absolute difference of 2.09 and 3.11% for V_{150} and V_{200} , respectively. For MCref-45, the 45° seed angle approximation produces results in closer agreement with MCref, with mean absolute differences in *PTV0.5* V_{150} and V_{200} values of just 0.60 and 1.32%.

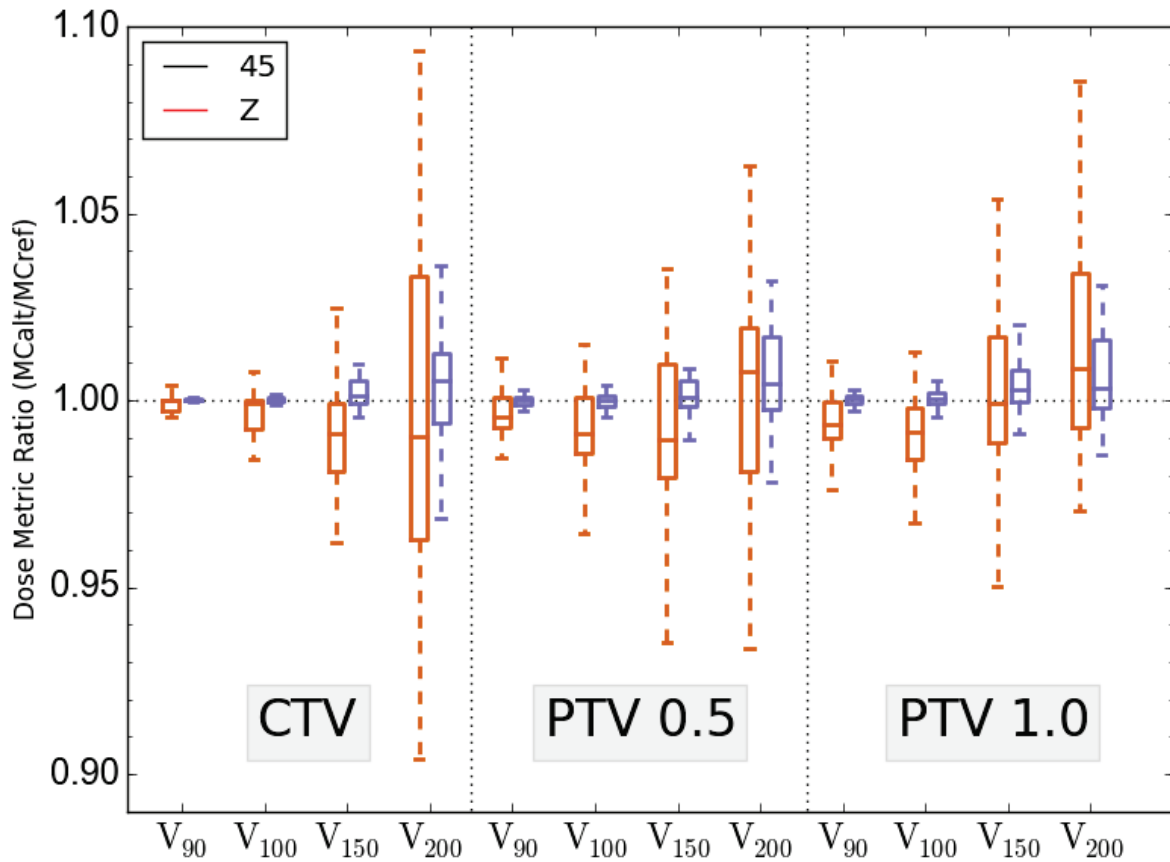


Figure 3.17: Boxplots representing the ratios of volume metrics generated by different seed orientations for all cohort patients. Presented dose ratios are MCref-z / MCref (Orange, Left) and MCref-45 / MCref (Purple, Right)

As shown in Figure 3.18 and Table 3.9, seed orientation can have a considerable effect on peak skin dose and D_{1cm^2} metrics in many patients. High dose skin areas are

often created by only a few seeds located very closely to the skin. At these short length scales, the photon emission of a Theraseed200 ^{103}Pd seed is not isotropic, due to lack of spherical symmetry in seed construction and radionuclide distribution. Therefore, a difference in seed orientation, relative to the position of high dose skin voxels, can cause appreciable differences in skin dose metrics. Similarly to target dose metrics, the 45° seed angle approximation produces better consistency with MCref results than MCref-z. The average difference in $D_{1\text{cm}^2}$ values between MCref and MCref-z is 4.1%, with one patient differing by 27.5% (as this patient is a large outlier, the data point is not shown in Figure 3.18). MCref and MCref-45 $D_{1\text{cm}^2}$ differ by less, but the average $\% \Delta$ is still 2.9%.

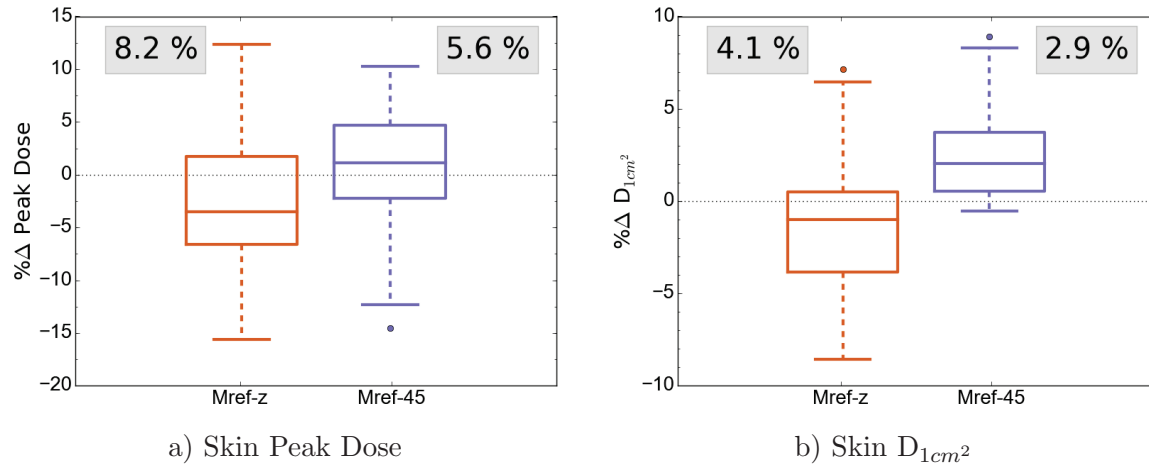


Figure 3.18: Boxplots of skin dose $\% \Delta$ due to seed orientation. Differences between MCref and MCref-z are in orange (left), MCref and MCref-45 are in purple (right). The mean absolute $\% \Delta$ for both orientations is indicated in gray inset.

Rib and chest wall tissues are also often located close enough to seed positions for changes in seed orientation to impact dose metrics (Figure 3.19). The cortical bone present in these regions also often has such high μ_{en}/ρ and density values that even small changes to photon fluence and spectra can result in fairly sizable differences in dose. Comparing MCref-z and MCref, chest wall and rib peak doses differ by up to 47%; MCref-45 and MCref-45 peak doses differ by up to 24%.

Homogeneity and Conformity indices are fairly insensitive to seed orientation (Fig-

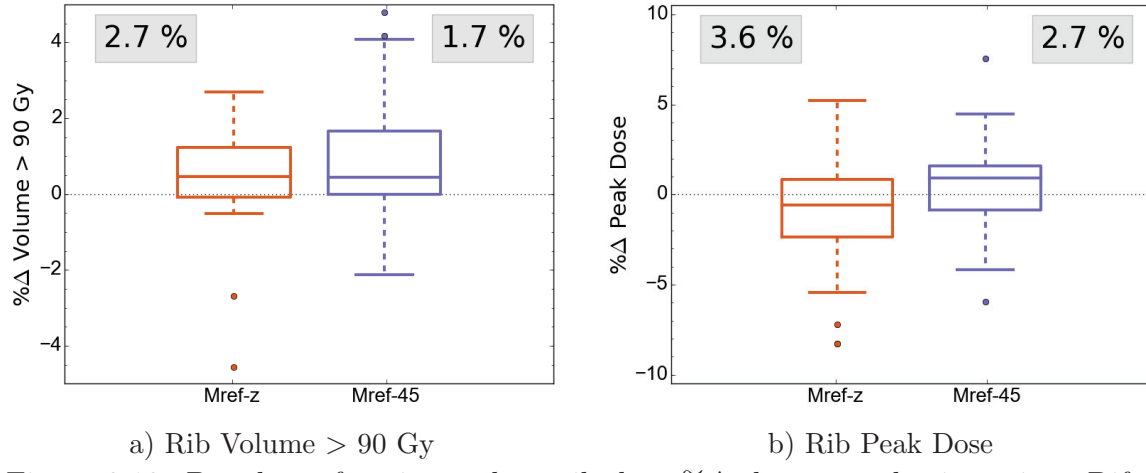


Figure 3.19: Boxplots of patient cohort rib dose $\% \Delta$ due to seed orientation. Differences between MCref and MCref-z are in orange (left), MCref and MCref-45 are in purple (right). The mean absolute $\% \Delta$ for both orientations is indicated in gray inset.

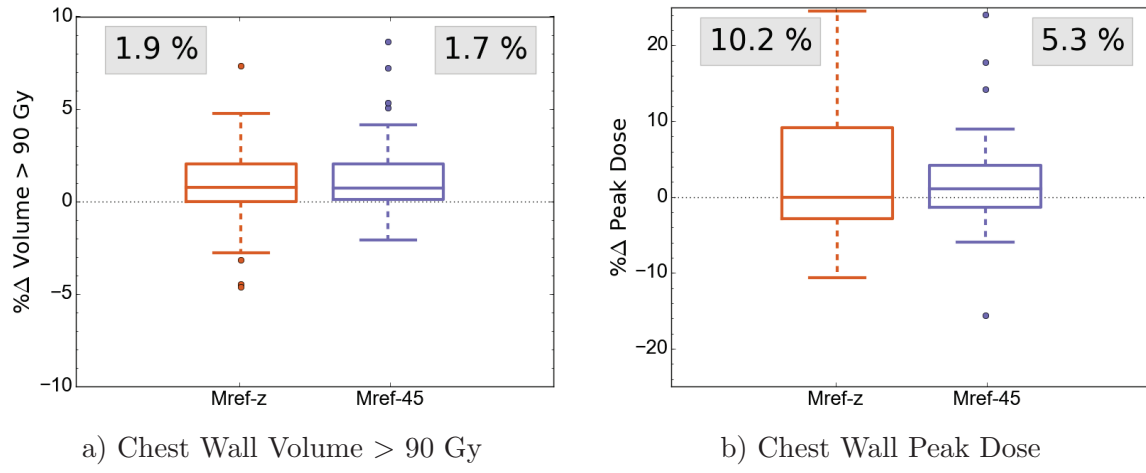


Figure 3.20: Boxplots of patient cohort chest wall dose $\% \Delta$ due to seed orientation. Differences between MCref and MCref-z are in orange (left), MCref and MCref-45 are in purple (right). The mean absolute $\% \Delta$ for both orientations is indicated in gray inset.

Table 3.9: Skin D_{1cm^2} metrics in simulations of MCref, MCref-45, and MCref-z

Patient Number	MCref [Gy]	MCref - Z		MCref - 45°	
		[Gy]	%Δ	[Gy]	%Δ
1	89.8	92.4	-2.90	88.0	2.02
2	6.6	7.8	-17.35	6.2	6.52
3	50.8	53.0	-4.34	48.9	3.75
4	65.6	65.2	0.61	65.6	0.07
5	13.1	16.7	-27.54	12.6	3.67
6	24.3	22.8	6.43	23.7	2.72
7	105.0	105.6	-0.64	103.5	1.42
8	122.3	127.0	-3.91	120.3	1.61
9	98.2	102.0	-3.80	96.9	1.37
10	106.4	103.3	2.89	104.3	1.93
11	77.3	76.6	0.94	77.7	-0.47
12	18.3	19.9	-8.56	16.8	7.93
13	110.3	112.7	-2.25	108.3	1.75
14	116.5	115.8	0.62	110.7	5.00
15	147.7	148.6	-0.58	148.2	-0.31
16	78.0	83.8	-7.41	75.2	3.67
17	113.0	118.3	-4.75	112.2	0.69
18	136.1	145.1	-6.63	131.2	3.61
19	84.2	81.5	3.14	81.8	2.82
20	65.7	67.5	-2.77	64.3	2.05
21	58.9	56.1	4.77	59.2	-0.53
22	151.8	157.0	-3.42	151.2	0.39
23	105.3	107.5	-2.04	102.9	2.28
24	87.1	87.9	-1.00	87.3	-0.30
25	65.7	62.7	4.66	65.5	0.37
26	99.9	101.8	-1.91	91.0	8.92
27	103.8	104.3	-0.52	92.8	10.54
28	136.5	137.2	-0.52	131.2	3.89
29	30.0	31.8	-5.84	28.0	6.77
30	176.9	178.1	-0.64	175.9	0.61
31	69.2	69.6	-0.65	66.9	3.29
32	69.5	70.9	-1.97	63.8	8.29
33	51.3	51.0	0.41	51.2	0.15
34	74.8	75.0	-0.26	73.4	1.86
35	43.3	40.2	7.14	43.1	0.46

ure 3.21). While small differences are seen between MCref and MCref-z in homogeneity and conformity indices, they are generally sub-2%. Differences between MCref and MCref-45 are usually sub-1%.

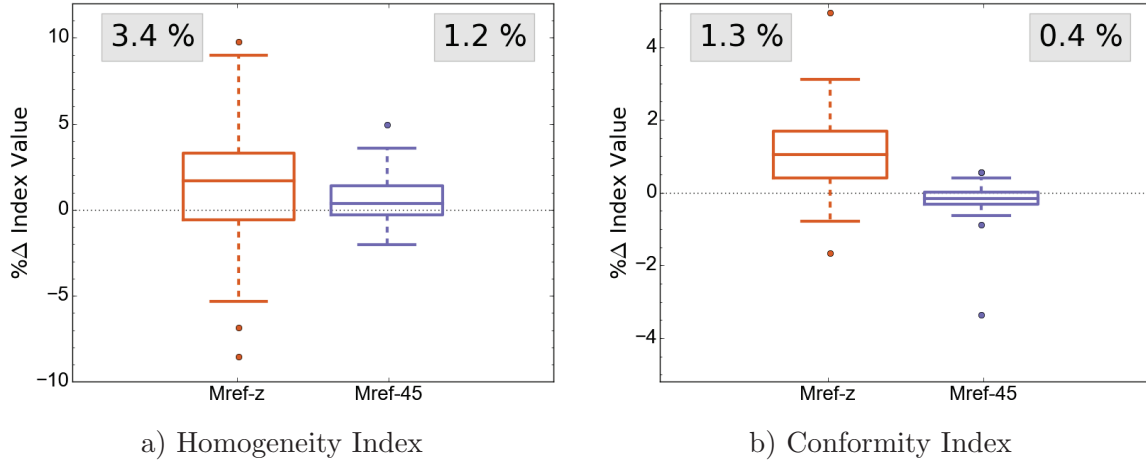


Figure 3.21: Boxplots of patient cohort homogeneity and conformity indices $\% \Delta$ due to seed orientation. Differences between MCref and MCref-z are in orange (left), MCref and MCref-45 are in purple (right). The mean absolute $\% \Delta$ for both orientations is indicated in gray inset.

As heart and lung tissues are located too far from seed locations to experience differences in dose due to seed orientation, they are not presented.

3.3 Lead shielding

The dosimetric effect of the BCCA specific lead shield is also investigated. The virtual lead shields (as described in 2.4) are overlaid on top of existing MCref patient models, creating MCref-Pb. MCref-Pb simulations were performed for all patients, creating dose distributions for comparison to existing MCref distributions. Skin peak doses and D_{1cm^2} values were extracted. The created virtual lead shield model has an insignificant effect on skin dose, with negligible differences between MCref and MCref-Pb in all examined patient D_{1cm^2} values.

To look more closely at the impact of lead shielding on individual dose distributions, a colourwash of dose differences (MCref/MCref-Pb) was created, using slice 79 from

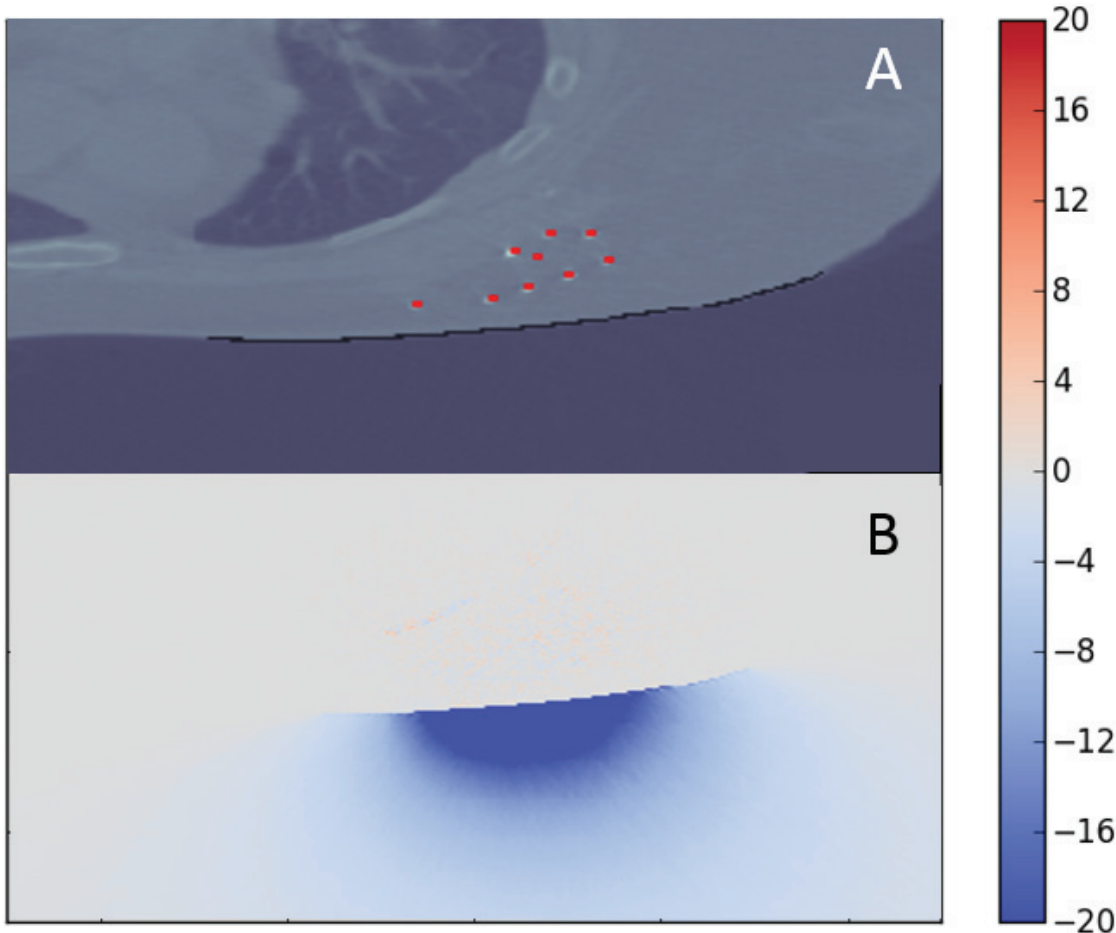


Figure 3.22: The position of the virtual lead shield, shown in black, and seed positions (red) with respect to patient #14’s anatomy (A). A colourwash of the same region is then presented (B), representing the dose differences (colourwash scale is in Gy) between MCref and MCref-Pb ($MCref - MCref-Pb$).

Patient #14 (Figure 3.22). For ease of comparison, this is the same patient and slice as seen in Figure 3.1 as well as Figure 2.2. No increases in dose due to the lead shield are seen in skin voxels (or voxels of any tissue (Figure 3.22 B)), despite the proximity of photon-emitting sources to the shield. On the opposite side of the shield, dose to air is considerably reduced. Within a few centimeters of the shield center, differences in dose to air voxels of greater than 20 Gy occur. This lack of skin dose increase is consistently seen in all patient dose ratio visualizations.

Chapter 4

Discussion

4.1 Comparison of MCref and TG43sim models

This retrospective MC study demonstrates large differences in dose distributions between the traditional, clinical TG43 approach, and patient-specific model-based MC dose calculations. Comparing our reference patient-specific detailed model (MCref) and the water-based, TG43 model (TG43sim), considerable differences in PBSI dose distributions occur in all patients. TG43sim consistently overestimates dose in the tumour region, with differences in patient D₉₀ values routinely exceeding 10 Gy (Table 3.2). In healthy tissues, TG43sim underestimates dose, downplaying the potential risk for radiation induced toxicity. Important skin doses are often misrepresented by 20% or more; heart and lung metrics are tens of percent lower in TG43sim; TG43sim rib doses differ from MCref models by greater than a factor of three. These differences between TG43sim and MCref dose metrics also have a large inter-patient variability, preventing the possible use of these percentage differences as correction factors for existing TG43 methods. This motivates the clinical adoption of MBDCAs with corresponding patient-specific models, such as the MC calculations carried out in this thesis, to correctly account for the dose distribution altering effects of accurate tissue assignment and seed attenuation in patient anatomies.

Several other works in the literature have undertaken investigations into the effects of tissue heterogeneity and interseed attenuation on PBSI dose distributions. The following paragraphs examine the works of Miksys et al³², Afsharpour et al³³, and Mashouf et al⁵², whose results regarding PBSI brachytherapy provide interesting points of comparison for this work. Unfortunately, the lack of clear guidelines for virtual breast model creation can result in substantial differences between literature models and the ones used in this thesis, weakening the ability to make direct comparisons between the PBSI dose distributions observed in various cancer centres.

Miksys et al.³² investigated patient-specific MC dose calculations in PBSI treatments, exploring several necessary assumptions for deriving PBSI patient models. Patient-specific, adipose-gland segmented models were created for 4 PBSI patients treated at The Ottawa Hospital Cancer Centre (TOHCC), allowing for the extraction of D_{90} , V_{100} , V_{200} , and HI metrics. Despite both hospitals prescribing a 90 Gy target dose, the four patient cohort, TG43-based D_{90} values were found to be 45.9, 76.4, 28.0, and 46.7 Gy ($\bar{D}_{90} = 49.3$ Gy), significantly lower than TG43sim results in this study ($PTV0.5 \bar{D}_{90} = 105.1$ Gy). Considering the patient model closest in construction to MCref, ‘Detailed2’, D_{90} values of 40.8, 64.1, 26.3, and 41.6 Gy were found, with a mean of 43.2 Gy. This result is considerably lower than the mean D_{90} found herein using MCref (91.7 Gy). It is unlikely that a difference in absolute doses of this magnitude is caused solely by the small differences in model construction between MCref and ‘Detailed2’. This 48.5 Gy decrease in average D_{90} value could be partially explained by a difference in target definition, as Miksys et al did not define the *PTV* used in planning at TOHCC, or could be representative of large differences in PBSI treatment planning and surgical techniques between treatment centers. Despite these large differences in absolute target dose, the mean percentage discrepancy found between detailed and TG43-based models is similar. Miksys reports that a water-based model overestimates D_{90} by 14.6% on average,

compared to the 14.1% difference found in this thesis. Extracted skin metrics are also comparable between the two works. Although large patient-by-patient variations are always seen in skin D_{1cm^2} values, all four TOHCC patients report skin metric values consistent with those seen in TG43sim and MCref. The mean TOHCC patient skin D_{1cm^2} increases by 18.2% (from 46.5 Gy to 57 Gy) when detailed tissues are considered, comparable to the increase in skin D_{1cm^2} from TG43sim to MCref of 22.2% presented in this thesis.

In 2011, Afsharpour et al³³ investigated the consequences of using different tissue modeling schemes in MC calculations of PBSI brachytherapy dose distributions for 28 patients treated at the Toronto Sunnybrook Hospital. Several alternative water and detailed patient models were created, allowing for the extraction of PTV D_{90} values. Although dose to water ($D_{w,m}$) was the primary dose scoring method, dose to medium ($D_{m,m}$) results were also reported, allowing for a comparison to the results of this thesis. For treatment evaluation, the Sunnybrook planning target volume was defined as the lumpectomy cavity plus an additional 1 cm margin, so MCref and TG43sim results are compared using the equivalent target examined in this work, *PTV1.0*. Of the six models presented, ‘Uniform Water Breast’ (UWB) and ‘Segmented Breast Tissue’ (SBT), are the most similar in construction to TG43sim and MCref, respectively. Using UWB and SBT models to consider the effects of interseed attenuation and accurate tissue modeling results in an average D_{90} decrease of 19.7%, larger than the average 14% decrease demonstrated by both Miksys et al³² and this thesis. A mean UWB D_{90} value of 86.8 Gy, with a range of 53.8 to 147.6 Gy, is reported for a 28 patient cohort, higher than the mean MCref *PTV1.0* D_{90} of 77.1 Gy. The use of the SBT model results in average D_{90} values of 72.5 Gy, with individual values between 47.1 and 121.7 Gy, compared to a mean TG43sim *PTV1.0* D_{90} of 67.2 Gy. This indicates that patients treated at Sunnybrook Hospital are receiving comparatively higher doses than

the BCCA patients considered herein, with the average target dose found to be 12.5% greater in Sunnybrook treated patients (MCref vs. SBT).

Alternative non-MC methods to account for the effects of tissue heterogeneity have also been proposed in the literature. Mashouf et al^{52,53} have created a new methodology that uses a patient-specific inhomogeneity correction factor (ICF) to modify existing TG43 dose distributions, possibly improving the accuracy of dose metrics without requiring the use of MC simulations. This multiplicative ICF factor is computed on a voxel-by-voxel basis and is defined in terms of the attenuation coefficient (μ) and mass energy absorption coefficient (μ_{en}) of water and breast tissues at the mean photon energy of ^{103}Pd . By choosing to use a 1D source approximation for the TG43 formalism underlying the initial, pre-ICF dose distributions, seeds are modeled as simple point sources, ignoring the effects of seed material and 3D radionuclide distribution. Average percentage differences in skin and CTV (defined equivalently to the $PTV1.0$ used in BCCA target definition) dose metrics between TG43 and $TG43 \times \text{ICF}$ were presented for a 140 patient cohort.⁵² In calculating percentage differences in dose metrics, Mashouf et al used a slightly different $\% \Delta$ definition than Eq. (4.1). With inadequate information provided to convert Mashouf values to our $\% \Delta$ definition, an alternate method to calculate percentage differences is defined as

$$\% \Delta_{Mashouf} = \frac{M_{MCref} - M_{TG43}}{M_{TG43}} \times 100\% \quad (4.1)$$

to allow for the comparison of ICF and MCref dose metrics.

The use of the ICF correction factors causes a reduction in target D_{90} values by 6.2%, with extracted V_{90} , V_{100} , V_{150} , and V_{200} metrics shrinking by 4.2, 5.4, 6.9, and 8.2 % respectively. Comparing the MCref and TG43sim models, percentage decreases in D_{90} and $PTV1.0$ V_{90} (V_{100} , V_{150} , V_{200}) are 12.3% and 5.65% (7.30%, 20.9%, 32.1%),

considerably larger than the decreases observed using the ICF method. This difference is especially notable in the regions of high target dose represented by V_{150} and V_{200} . In the skin, the use of an ICF correction factor results in a mean percentage increase in D_{1cm^2} of 17.6%, whereas a 33.9% increase from TG43sim to MCref was observed in this thesis. While the changes in dose created by the use of an ICF factor agree with the general dosimetric trends appearing in this thesis, it is clear the differences between ICF and TG43 based dose distributions are much smaller than the differences observed between water-based and detailed models in MC simulations, indicating the ICF method may not be completely capturing the dosimetric effects of accurate tissue and seed modeling.

4.2 Sensitivities in patient modeling

The structure and composition of patient breast tissues is a highly individualistic element of PBSI treatments. The density and proportion of breast adipose and gland tissues varies significantly from patient to patient⁵⁴, dependent on many factors, such as patient age, lifestyle⁵⁵, and hormone concentrations⁵⁶. The proper segmentation of these varying adipose and gland tissues in the breast has been shown to be an important aspect of calculating accurate breast brachytherapy dose distributions³⁰, but an investigation into the sensitivity of MBDCA dose calculations to the use of a patient-specific adipose-gland segmentation threshold has not been performed, motivating the creation of the MCfixed patient model. For most patients, only minor (sub-1%) differences exist between the fixed threshold (MCfix) and individualized (MCref) model dose and volume metrics, but outliers do occur. When comparing MCref and MCfixed, the largest differences in target D_{90} , V_{100} , and V_{200} are found to be 4.6%, 2.2%, and 8.7% respectively. While these differences in dose metric value are not typical (as the majority of patients

have only small density differences between their custom adipose-gland boundary and the constant MCfix value), they do indicate the potential for considerable dose metric errors in patients with non-typical adipose and gland tissue densities.

The only comparable result in PBSI literature is the 2016 work done by Miksys et al³². Rather than investigate the issue of patient-specific segmentation thresholds, Miksys et al compared two fixed boundaries, each motivated by different literature reported adipose and gland densities (Woodard and White⁴⁴ and Afsharpour³³). While these two models represent a larger change in boundary density (0.29 g cm^{-3}) than any patients analyzed in this work, as well as being a comparison between two fixed boundary models rather than using a patient-specific threshold, it is still useful as a point of comparison for patients with large changes in threshold between MCref and MCfixed. By changing the adipose-gland segmentation threshold, Miksys et al reported variations in target D_{90} , V_{100} , and V_{200} values up to 3%, 3% and 19% respectively, and skin D_{1cm^2} values change by up to 4%. These variations in metric are comparable to the largest differences between MCref and MCfixed metrics in this thesis, further illustrating the sensitivity of patient dose distributions to adipose-gland thresholding.

A few studies have attempted to examine the effects of seed orientation on brachytherapy dose distributions, but these works were either focused on prostate brachytherapy or used non-realistic seed angles in their investigations. For ^{125}I prostate brachytherapy, Fekete et al⁵⁷ compared parallel and realistic seed orientations. No significant changes in patient CTV metrics were observed, but average differences of 2% in external organs at risk were reported. In the breast, Miksys et al³² investigated seed orientation in heterogeneous ^{103}Pd PBSI models for four patients, considering seeds that differed in orientation from an axial-oriented reference case by either 90° or a randomly chosen angle between 0° and 45° . This method showed large differences in D_{90} , with up to 4% and 20% differences in random and 90° rotations (when compared to consistent axial

orientation). Skin D_{1cm^2} values varied by up to 6% (random) and 20% (axial).

In the current work, differences in D_{90} of greater than 2% are seen in a large portion of the cohort when comparing realistically (MCref) and axially modeled (MCref-z) source orientations. The average difference between MCref and MCfixed in peak skin doses (8.2%) and skin D_{1cm^2} values (4.1%) is also large. These differences are smaller than those seen by Miksys et al³², but use a larger patient cohort to support the idea that axial seed orientation is a poor approximation of actual seed angles, and motivate attempts to realistically position seeds in the breast. When better approximations of realistic seed angles are used (MCref-45), differences in target metrics are much smaller, with an average difference of sub-2% between MCref and MCfixed for D_{90} , V_{90} , V_{100} , and V_{150} values. However, larger discrepancies are seen in V_{200} , as well as skin, rib, and chest metrics for many patients. This suggests that while the MCref-45 45° approximation gives considerably more accurate results than the default MCref-z axial approximation used in many PBSI works, actual seed angles should be used whenever possible to recreate treatment conditions.

Lastly, a simple lead shield model is shown to have little dosimetric effect on patient skin. This use of a lead shield is not typical treatment protocol in PBSI brachytherapy, as the chosen ^{103}Pd isotope minimizes the potential for incidental radiation dose to the patient's loved ones. However, this is still a favourable result for patients choosing to wear the shield post-treatment, who are predominately patients requiring extra reassurance that family and friends will not be affected by the radiation present in the treatment.

4.3 Evaluation of treatment doses

In Section 2.2 the goal of the performed PBSI treatments was stated as “to deliver a prescription dose of 90 Gy to the target ($PTV0.5$), while minimizing the dose received by the skin and other normal tissues.” Using the results presented in Section 3.1.1, the ability of the created PBSI dose distributions to achieve this goal is assessed.

Looking just at the water-based TG43sim model, one would determine that the prescribed target dose of 90 Gy was achieved in 25 of 35 cases (71%) when using D_{90} as an analog for treatment dosage (Figure 3.2). However, once the D_{90} lowering effects of accurate tissue and seed modeling are accounted for in MCref, the number of patients receiving the prescribed dose is lowered to 20 (57%). Of the fifteen patients with MCref D_{90} values below 90 Gy, seven receive $PTV0.5$ doses just below the prescribed dose (80 - 90 Gy in MCref). Of potential clinical concern are patients receiving target doses well below the prescribed dose, with three patients (#7, #27, and #29) having MCref $PTV0.5$ D_{90} values below 60 Gy (59.3, 56.2, and 47.3 Gy). If only TG43-based modeling was performed, two of these patients would not have been identified as potential low dose risks, as their TG43sim D_{90} values are 16.7% (#7) and 18.3% (#27) higher (69.2 Gy and 66.5 Gy). Although no long-term retrospective study has connected MC target doses to treatment outcomes in PBSI patients (as PBSI treatments have only been performed on a small scale since 2006), the patients receiving these low target doses should be shown particular clinical interest in follow up appointments, as the low MCref D_{90} values may indicate a higher risk for DCIS recurrence. Future work should attempt to correlate treatment outcomes with accurate MBDCA doses. This will allow for a possible revision of PBSI prescription dose and target definition to account for the differences in dose shown by MC PBSI studies, improving PBSI treatment planning and evaluation in the long term.

While providing a lethal radiation dose to tumour cells is critical, another goal of PBSI treatment is to minimize the dose delivered to skin and other healthy tissues. As no dose thresholds or limits are set for these structures in PBSI literature, the evaluation of this goal is more subjective. Even without knowledge of PBSI organ dose limits, it is readily apparent that significant skin D_{1cm^2} values are seen in PBSI patients. Skin D_{1cm^2} values exceed the treatment dose of 90 Gy in 43% in patients, with many of these patients having peak skin dose values of over 200 Gy. Had these patients been evaluated using the current TG43 treatment planning approach, assessed skin D_{1cm^2} values would have been 22.2% lower on average, possibly misrepresenting the potential for skin damage. Recently, Mashouf et al⁵² attempted to correlate treatment outcomes with skin metrics produced using the ICF formalism. The usage of the ICF method led to an increase in correlation of skin side effects to skin dose metrics by up to 91%, a significant improvement in the ability to predict skin toxicity. However, as previously mentioned, the ICF method may not be as accurate as the use of full MC simulations, suggesting MBDCAs may be able to further improve predictions of skin toxicity in treatment evaluation.

Rib doses are also grossly underestimated by water-based models, with MCref modeling causing the average estimated rib volume over 90 Gy to increase by a factor of 6. However, adult cortical bone is not considered to be a relatively radiosensitive organ, and previous studies investigating brachytherapy treatments with ^{125}I sources implanted less than 0.5 cm from the ribs showed no osseous toxicity in a long-term retrospective analysis⁵⁸. Heart and lung doses are very low in both TG43sim and MCref models, with mean heart V_{50} and V_{10} values equal to zero, and mean heart doses below 0.60 Gy for all MCref patients. However, when heart D_{1cm^2} metrics are extracted, some MCref models have values above 10 Gy. Although this is still well below the guidelines set to prevent pericarditis by the ‘Quantitative Analyses of Normal Tissue Effects in the

Clinic' (QUANTEC) study⁵⁹, it may still be high enough to warrant clinical interest, as the rate of long-term, post-radiation major coronary events has been linked to heart dose with no apparent lower threshold⁶⁰. To prevent radiation induced pneumonitis, QUANTEC sets a limit of mean lung dose at 7 Gy, a much higher value than that received by all BCCA PBSI patients (as indicated by the low values of MCref patient lung V₅ and V₂₀ values).

4.4 Future directions

The successful transition from TG43 to MBDCA-based clinical treatment planning and evaluation relies heavily on the accuracy of the breast models used in simulations. Many works in the literature have examined different aspects of breast modeling, aiding in the transition from simple, basic breast models to complex, more accurate virtual representations. The antiquated assumption that breast is composed of 50% fibroglandular tissue and 50% fat tissue was shown to be unrealistic^{26,54}. The use of different MAR methods has been investigated³¹, with the STR technique recommended for its ability to mitigate CT artifacts while preserving tissue heterogeneity. The segmentation of adipose and gland tissues is required, as it significantly changes the photon fluence when compared to averaged tissue phantoms^{30,33}. To improve the accuracy of this segmentation, this thesis demonstrates that adipose-gland segmentation should be performed using a patient-specific tissue threshold, rather than a single, fixed density boundary. This thesis also suggests that the orientation of modeled sources should be as close to realistic as possible, as the axial seed positioning used in other MC studies may introduce errors into skin and target dose metrics.

Despite this work addressing some outstanding questions in MC breast model creation, several other assumptions involved in MC model-creation remain unanswered.

Large uncertainties exist in the elemental composition of assigned breast tissue. These uncertainties have been shown to have large effects on brachytherapy dose distributions for a small number of patients³², but no study has assessed the possible difference in dose metrics due to variations in elemental composition for a substantial patient cohort. CT scans taken at one month post-implantation are assumed to be representative of patient anatomies, but the swelling and edema common to PBSI surgeries can result in variable patient geometries over the course of several ¹⁰³Pd half lives. Breast geometries may also shift when moving from the supine position used in CT imaging and the upright position of day-to-day patient activities. The assignment of skin tissue often relies on an approximation of skin thickness, but no consensus skin thickness value has been chosen. Current works in the literature use thickness values of 1 mm (Mashouf et al (2016)⁵²), 2 mm (this Thesis (based on work by Hilts et al at the BCCA¹¹) and Afsharpour et al³³ (2011)), and 5 mm (Afsharpour et al³³ (2010) and Miksys et al³² (2016)), but no research has investigated the effect of these varying skin depths on skin dose metrics.

These unaddressed questions in model-creation could potentially have considerable influence on the calculation of patient dose distributions. Additionally, this thesis quantifies PBSI radiation dose to the tumour and organs at risk, but no study has yet coupled MC patient-specific PBSI dose metrics with patient outcomes. Recent ICF work by Mashouf et al⁵² demonstrated the possible predictive abilities of more accurate dose calculation, but additional studies are needed to fully understand the relationship between accurate PBSI dose metrics and patient health. The dosimetric results presented in this thesis could be used in these future outcomes studies.

Chapter 5

Conclusions and Outlook

The current clinical treatment planning approach for PBSI brachytherapy is based on the TG43 formalism. Source dose distributions are calculated in water media, ignoring the influence of interseed attenuation. To quantify the effects of tissue heterogeneity and interseed attenuation on photon energy deposition, this thesis considered a retrospective dosimetric study of 35 PBSI patients treated at the BC Cancer Agency between 2012 and 2016, the first such treatment evaluation performed on patients treated at this clinic. Water-based and detailed, full-tissue models are created for simulation using the MBDCA egs_brachy, allowing for 32 different dose metrics to be extracted for several target definitions and five organs at risk. Large differences in patient dose distributions are demonstrated between TG-43-based models (TG43sim) and those accounting for tissue heterogeneity and interseed attenuation (MCref). Current TG43 methods considerably overestimate the dose delivered to the target, with differences of up to 28% occurring in extracted D₉₀ values. Doses to the skin, ribs, heart, and lungs are all underestimated by the TG43 formalism, often by greater than 20%.

This thesis demonstrated a sensitivity in MBDCA dose distributions to currently unexplored options in the creation process behind the use of patient-specific models. Differences in dose metrics between MCref and MCfixed support the determination of adipose-gland segmentation thresholds on a patient-by-patient basis. Although the

difference between the fixed-boundary and individualized-boundary models was not substantial for all patients, a relationship is shown between the difference in adipose-gland boundary value and dose metrics. For patients with atypical breast tissue densities, this relationship may lead to appreciable differences in target and organ metrics. Differences observed between simulations of the reference case (MCref), with seeds oriented according to the planned angle of the surgical needle, and those with axially aligned seeds (MCref-z) are above 3% for many target and skin metrics, suggesting seed orientation should be modeled as accurately as conditions allow. If possible, seed angles should be modeled according to recorded surgical information. In the absence of known orientations, a best approximation should be made. The smaller dosimetric differences between MCref and MCref-45 (seeds angled at a 45° approximation), relative to those seen between MCref and MCref-z, suggest that a seed angle of 45° across the transverse plane may be a good choice of approximation. Negligible differences in patient dose distributions are found when the BCCA lead shield used for radiation protection was modeled in egs-brachy, suggesting it can be ignored in future PBSI dosimetric studies.

The sensitivity of MBDCA dose calculations to variations in patient modeling motivates the adoption of a standardized procedure for the creation of PBSI breast models, such as the procedures used herein to create MCref. Future PBSI work has many opportunities to improve the accuracy of these models. Research into breast tissue compositions is required, as many of the tissue elemental compositions used in this thesis are taken from antiquated sources examining only a few patients. A study into the sensitivity of skin dose metrics to assumptions of skin depth should be performed, as skin thicknesses from 1 to 5 mm are routinely used in PBSI literature. Volume-changing breast models should be investigated, as the use of static breast models may be inaccurate due to the swelling and edema caused by the surgical implantation. Finally, outcomes studies are needed to correlate more accurate MBDCA dose metrics

with patient outcomes. If MC-based dose metrics become the norm, clinical dose targets and thresholds could also need revision, in order to better reflect the new, more accurate patient doses.

Appendix A

CT Calibration Curve

All pixel mass density (g cm^{-3}) values used in this thesis had to be first derived from the original Hounsfield Units (HU) output by the CT machine. This conversion is performed using a CT calibration curve, presented in Table A.1. Mass density values for CT Numbers found between any two listed values are calculated using a linear interpolation. The CT scanner used in this work was a GE Lightspeed RT 16 using a 120 kV, 250 mA helical scan parameters, with a 2 mm slice spacing and 56 cm field of view.

Table A.1: CT calibration curve for the conversion of pixel Hounsfield Units into mass density values

CT Number / HU	Mass Density / g cm^{-3}
-1000	0.001
0.0	1.008
61.9	1.073
1000	1.667
2000	2.300
3000	2.933
3100	2.999
5000	2.999
10000	7.365
20000	10.000
25000	10.000

References

- [1] Canadian Cancer Societys Advisory Committee on Cancer Statistics, Canadian Cancer Statistics 2016, Technical report, Canadian Cancer Society, Toronto, Canada, 2016. (p 1)
- [2] V. L. Ernster, J. Barclay, K. Kerlikowske, D. Grady, and I. Henderson, Incidence of and treatment for ductal carcinoma in situ of the breast, *Jour. Am. Med. Assoc.* **275**, 913–918 (1996). (pp 1 and 2)
- [3] M. J. Silverstein, M. D. Lagios, P. H. Craig, J. R. Waisman, B. S. Lewinsky, W. J. Colburn, and D. N. Poller, A prognostic index for ductal carcinoma in situ of the breast, *Cancer* **77**, 2267–2274 (1996). (p 1)
- [4] R. Holland, J. S. Stekhoven, J. Hendriks, A. Verbeek, and M. Mravunac, Extent, distribution, and mammographic/ histological correlations of breast ductal carcinoma in situ, *The Lancet* **335**, 519 – 522 (1990). (p 2)
- [5] J.-P. Julien, N. Bijker, I. S. Fentiman, J. L. Peterse, V. Delledonne, P. Rouanet, A. Avril, R. Sylvester, F. Mignolet, H. Bartelink, and J. A. V. Dongen, Radiotherapy in breast-conserving treatment for ductal carcinoma in situ: first results of the EORTC randomised phase III trial 10853, *The Lancet* **355**, 528 – 533 (2000). (p 2)
- [6] E. R. Fisher, J. Costantino, B. Fisher, A. S. Palekar, and C. Redmond, Pathologic findings from the national surgical adjuvant breast project (NSABP) protocol B-17. Intraductal carcinoma (ductal carcinoma in situ), *Cancer* **75**, 1310–1319 (1995). (p 2)
- [7] E. B. Podgorsak, *Radiation Physics for Medical Physicists (2nd Ed)*, Springer-Verlag, Berlin, 2010. (pp 2 and 6)
- [8] E. J. Hall and A. J. Giaccia, *Radiobiology for the Radiologist*, 7th ed., Lippincott Williams & Wilkins, Philadelphia, 2012. (p 3)
- [9] L. L. Anderson *et al.*, *Interstitial Brachytherapy: Physical, Biological, and Clinical Considerations*, Raven Press, New York, 1990. (p 4)
- [10] J.-P. Pignol, B. Keller, E. Rakovitch, R. Sankreacha, H. Easton, and W. Que, First report of a permanent breast ^{103}Pd seed implant as adjuvant radiation treatment for early-stage breast cancer, *Int. J. Radiat. Oncol. Biol. Phys.* **64**, 176 – 181 (2006). (p 4)

- [11] M. Hilts, H. Halperin, D. Morton, D. Batchelar, F. Bachand, R. Chowdhury, and J. Crook, Skin dose in breast brachytherapy: Defining a robust metric, *Brachytherapy* **14**, 970 – 978 (2015). (pp 4 and 79)
- [12] Z. Chen and R. Nath, Dose rate constant and energy spectrum of interstitial brachytherapy sources, *Medical Physics* **28**, 86–96 (2001). (p 4)
- [13] D. Batchelar, M. Hilts, M.-P. Milette, and J. Crook, Starting a Pd-103 Permanent Breast Seed Implant Program: Dosimetric Results for Our First 25 Cases, *Brachytherapy* **15**, S45 (2017). (p 4)
- [14] R. Nath, L. L. Anderson, G. Luxton, K. A. Weaver, J. F. Williamson, and A. S. Meigooni, Dosimetry of interstitial brachytherapy sources: Recommendations of the AAPM Radiation Therapy Committee Task Group No. 43, *Med. Phys.* **22**, 209 – 234 (1995). (p 5)
- [15] R. E. P. Taylor and D. W. O. Rogers, An EGSnrc Monte Carlo-calculated database of TG-43 parameters, *Med. Phys.* **35**, 4228 – 4241 (2008). (p 5)
- [16] F. H. Attix, *Introduction to Radiological Physics and Radiation Dosimetry*, Wiley, New York, 1986. (p 6)
- [17] R. M. Thomson and D. W. O. Rogers, Monte Carlo dosimetry for ^{125}I and ^{103}Pd eye plaque brachytherapy with various seed models, *Med. Phys.* **37**, 368 – 376 (2010). (pp 8 and 36)
- [18] L. Beaulieu, A. C. Tedgren, J.-F. Carrier, S. D. Davis, F. Mourtada, M. J. Rivard, R. M. Thomson, F. Verhaegen, T. A. Wareing, and J. F. Williamson, Report of the Task Group 186 on model-based dose calculation methods in brachytherapy beyond the TG-43 formalism: Current status and recommendations for clinical implementation, *Med. Phys.* **39**, 6208 – 6236 (2012). (pp 9 and 22)
- [19] M. Chamberland, R. E. P. Taylor, D. W. O. Rogers, and R. M. Thomson, egs_brachy: a versatile and fast Monte Carlo code for brachytherapy, *Phys. Med. Biol.* **61**, 8214 – 8231 (2016). (pp 10, 25, 27, and 29)
- [20] J. F. Williamson, Monte Carlo evaluation of kerma at a point for photon transport problems, *Med. Phys.* **14**, 567 – 576 (1987). (p 10)
- [21] R. E. P. Taylor, G. Yegin, and D. W. O. Rogers, Benchmarking BrachyDose: voxel-based EGSnrc Monte Carlo calculations of TG-43 dosimetry parameters, *Med. Phys.* **34**, 445 – 457 (2007). (p 10)
- [22] J.-F. Carrier, L. Archambault, L. Beaulieu, and R. Roy, Validation of GEANT4, an object-oriented Monte Carlo toolkit, for simulations in medical physics, *Med. Phys.* **31**, 484–492 (2004). (p 10)
- [23] R. E. P. Taylor, G. Yegin, and D. W. O. Rogers, Monte Carlo modeling of the Xoft Axxent x-ray source, *Med. Phys.* **33**, 2205 (2006). (p 10)

- [24] O. Chibani, J. F. Williamson, and D. Todor, Dosimetric effects of seed anisotropy and interseed attenuation for ^{103}Pd and ^{125}I prostate implants, *Med. Phys.* **32**, 2557 – 2566 (2005). (p 10)
- [25] J.-F. Carrier, L. Beaulieu, F. Therriault-Proulx, and R. Roy, Impact of interseed attenuation and tissue composition for permanent prostate implants, *Med. Phys.* **33**, 595 – 604 (2006). (p 10)
- [26] M. J. Yaffe, J. M. Boone, N. Packard, O. Alonzo-Proulx, S.-Y. Huang, C. L. Peressotti, A. Al-Mayah, and K. Brock, The myth of the 50-50 breast, *Med. Phys.* **36**, 5437 – 5443 (2009). (pp 11 and 78)
- [27] H. Afsharpour, J.-P. Pignol, B. Keller, J.-F. Carrier, B. Reniers, F. Verhaegen, and L. Beaulieu, Influence of breast composition and interseed attenuation in dose calculations for post-implant assessment of permanent breast ^{103}Pd seed implant, *Phys. Med. Biol.* **55**, 4547 – 4561 (2010). (p 11)
- [28] G. Landry, B. Reniers, L. Murrer, L. Lutgens, E. Bloemen-Van Gurp, J.-P. Pignol, B. Keller, L. Beaulieu, and F. Verhaegen, Sensitivity of low energy brachytherapy Monte Carlo dose calculations to uncertainties in human tissue composition., *Med. Phys.* **37**, 5188 – 5198 (2010). (p 11)
- [29] C. Furstoss, B. Reniers, M. J. Bertrand, E. Poon, J.-F. Carrier, B. M. Keller, J.-P. Pignol, L. Beaulieu, and F. Verhaegen, Monte Carlo study of LDR seed dosimetry with an application in a clinical brachytherapy breast implant, *Med. Phys.* **36**, 1848 – 1858 (2009). (p 11)
- [30] J. G. H. Sutherland, R. M. Thomson, and D. W. O. Rogers, Changes in dose with segmentation of breast tissues in Monte Carlo calculations for low-energy brachytherapy, *Med. Phys.* **38**, 4858 – 4865 (2011). (pp 11, 22, 73, and 78)
- [31] N. Miksys, C. Xu, L. Beaulieu, and R. M. Thomson, Development of virtual patient models for permanent implant brachytherapy Monte Carlo dose calculations: interdependence of CT image artifact mitigation and tissue assignment, *Phys. Med. Biol.* **60**, 6039 (2015). (pp 11, 12, 18, and 78)
- [32] N. Miksys, J. E. Cygler, J. M. Caudrelier, and R. M. Thomson, Patient-specific Monte Carlo dose calculations for ^{103}Pd breast brachytherapy, *Phys. Med. Biol.* **61**, 2705–2729 (2016). (pp 11, 12, 18, 22, 25, 31, 70, 71, 74, 75, and 79)
- [33] H. Afsharpour, G. Landry, B. Reniers, J. P. Pignol, L. Beaulieu, and F. Verhaegen, Tissue modeling schemes in low energy breast brachytherapy, *Phys. Med. Biol.* **56**, 7045 – 7060 (2011). (pp 11, 12, 22, 24, 70, 71, 74, 78, and 79)
- [34] H. Afsharpour, B. Reniers, G. Landry, J.-P. Pignol, B. M. Keller, F. Verhaegen, and L. Beaulieu, Consequences of dose heterogeneity on the biological efficiency of ^{103}Pd permanent breast seed implants, *Phys. Med. Biol.* **57**, 809 – 823 (2012). (pp 11 and 12)

- [35] H. Afsharpour, G. Landry, M. D'Amours, S. Enger, B. Reniers, E. Poon, J.-F. Carrier, F. Verhaegen, and L. Beaulieu, ALGEBRA: ALgorithm for the heterogeneous dosimetry based on GEANT4 for BRachytherapy, *Phys. Med. Biol.* **57**, 3273 – 3280 (2012). (pp 11, 12, and 22)
- [36] M. Hilts, D. Batchelar, J. Rose, and J. Crook, Deformable image registration for defining the postimplant seroma in permanent breast seed implant brachytherapy, *Brachytherapy* **14**, 409 – 418 (2015). (p 12)
- [37] C. Xu, F. Vergaegen, D. Laurendeau, S. A. Enger, and L. Beaulieu, An algorithm for efficient metal artifact reductions in permanent seed implants, *Med. Phys.* **38**, 47 – 56 (2011). (p 16)
- [38] J. G. H. Sutherland, N. Miksys, K. M. Furutani, and R. M. Thomson, Metallic artifact mitigation and organ-constrained tissue assignment for Monte Carlo of permanent implant lung brachytherapy, *Med. Phys.* **41**, 011712 (2014). (pp 16 and 18)
- [39] J. G. H. Sutherland, K. M. Furutani, Y. I. Garces, and R. M. Thomson, Model-based dose calculations for ^{125}I lung brachytherapy, *Med. Phys.* **39**, 4365 –4377 (2012). (p 18)
- [40] P. S. Basran, A. Robertson, and D. Wells, CT image artifacts from brachytherapy seed implants: A postprocessing 3D adaptive median filter, *Med. Phys.* **38**, 712 – 718 (2011). (p 18)
- [41] M. Abdoli, M. R. Ay, A. Ahmadian, and H. Zaidi, A virtual sinogram method to reduce dental metallic implant artefacts in computed tomography-based attenuation correction for PET, *Nuclear Medicine Communications* **31**, 22 – 31 (2010). (p 18)
- [42] M. Abdoli, M. R. Ay, A. Ahmadian, R. A. J. O. Dierckx, and H. Zaidi, Reduction of dental filling metallic artifacts in CT-based attenuation correction of PET data using weighted virtual sinograms optimized by a genetic algorithm, *Med. Phys.* **37**, 6166 – 6177 (2010). (p 18)
- [43] ICRU, Photon, Electron, Photon and Neutron Interaction Data for Body Tissues, ICRU Report 46, International Comission on Radiation Units and Measurements, Washington D.C., 1992. (pp 19 and 24)
- [44] H. Q. Woodard and D. R. White, The composition of body tissues, *Brit. J. Radiol.* **59**, 1209 – 1219 (1986). (pp 19, 22, 24, and 74)
- [45] M. J. Rivard, B. M. Coursey, L. A. DeWerd, M. S. Huq, G. S. Ibbott, M. G. Mitch, R. Nath, and J. F. Williamson, Update of AAPM Task Group No. 43 Report: A revised AAPM protocol for brachytherapy dose calculations, *Med. Phys.* **31**, 633 – 674 (2004). (pp 19, 22, 25, 30, and 31)
- [46] J. Cui, B. Sahiner, H.-P. Chan, A. Nees, C. Paramagul, L. M. Hadjiiski, C. Zhou, and J. Shi, A new automated method for the segmentation and characterization of breast masses on ultrasound images, *Med. Phys.* **36**, 1553–1565 (2009). (p 22)

- [47] S. A. White, G. Landry, G. P. Fonseca, R. Holt, T. Rusch, L. Beaulieu, F. Verhaegen, and B. Reniers, Comparison of TG-43 and TG-186 in breast irradiation using a low energy electronic brachytherapy source, *Med. Phys.* **41** (2014). (p 22)
- [48] I. Kawrakow, E. Mainegra-Hing, D. W. O. Rogers, F. Tessier, and B. R. B. Walters, The EGSnrc Code System: Monte Carlo simulation of electron and photon transport, NRC Technical Report PIRS-701 v4-2-3-2, National Research Council Canada, Ottawa, Canada. <http://www.nrc-cnrc.gc.ca/eng/solutions/advisory/egsnrc/download.egsnrc.html>, 2011. (p 29)
- [49] M. J. Berger, J. H. Hubbell, S. M. Seltzer, and *et al.*, XCOM: Photon cross section database (version 1.5), Technical Report NBSIR87-3597, NIST, Gaithersburg, MD, <http://physics.nist.gov/xcom>, 2010. (p 30)
- [50] J. F. Williamson, Monte Carlo modeling of the transverse-axis dose distribution of the Model 200 ^{103}Pd interstitial brachytherapy source, *Med. Phys.* **27**, 643 – 654 (2000). (p 31)
- [51] R. Drzymala, R. Mohan, L. Brewster, J. Chu, M. Goitein, W. Harms, and M. Uriel, Dose-volume histograms, *Int. J. Radiat. Oncol. Biol. Phys.* **21**, 71 – 78 (1991), Three-Dimensional Photon Treatment Planning Report of the Collaborative Working Group on the Evaluation of Treatment Planning for External Photon Beam Radiotherapy. (p 31)
- [52] S. Mashouf, E. Fleury, P. Lai, T. Merino, E. Lechtman, A. Kiss, C. McCann, and J.-P. Pignol, Clinical significance of accounting for tissue heterogeneity in permanent breast seed implant brachytherapy planning, *Int. J. Radiat. Oncol. Biol. Phys.* **94**, 816 – 823 (2016). (pp 70, 72, 77, and 79)
- [53] S. Mashouf, E. Lechtman, P. Lai, B. M. Keller, A. Karotki, D. J. Beachey, and J. P. Pignol, Dose heterogeneity correction for low-energy brachytherapy sources using dual-energy CT images, *Phys. Med. Biol.* **59**, 5305 (2014). (p 72)
- [54] S. Vedantham, L. Shi, A. Karella, and A. M. O'Connell, Dedicated breast CT: Fibroglandular volume measurements in a diagnostic population, *Med. Phys.* **39**, 7317–7328 (2012). (pp 73 and 78)
- [55] G. Masala, D. Ambrogetti, M. Assedi, D. Giorgi, M. R. Del Turco, and D. Palli, Dietary and lifestyle determinants of mammographic breast density. A longitudinal study in a Mediterranean population, *International Journal of Cancer* **118**, 1782–1789 (2006). (p 73)
- [56] C. A. Haiman, L. Bernstein, D. V. D. Berg, S. A. Ingles, M. Salane, and G. Ursin, Genetic determinants of mammographic density, *Breast Cancer Research* **4**, R5 (2002). (p 73)
- [57] C.-A. Collins Fekete, M. Plamondon, A.-G. Martin, E. Vigneault, F. Verhaegen, and L. Beaulieu, Quantifying the effect of seed orientation in postplanning dosimetry of low-dose-rate prostate brachytherapy, *Med. Phys.* **41**, 101704–n/a (2014), 101704. (p 74)

- [58] L. Mandell, D. Nori, L. Anderson, M. Belanich, and B. Hilaris, The effects of permanent I-125 interstitial implantation on cortical bone, *Int. J. Radiat. Oncol. Biol. Phys.* **11**, 1029 – 1034 (1985). (p 77)
- [59] S. M. Bentzen, L. S. Constine, J. O. Deasy, A. Eisbruch, A. Jackson, L. B. Marks, R. K. Ten Haken, and E. D. Yorke, Quantitative Analyses of Normal Tissue Effects in the Clinic (QUANTEC): An introduction to the scientific issues, *Int. J. Radiat. Oncol. Biol. Phys.* **76**, S3–S9 (2010). (p 78)
- [60] S. C. Darby, M. Ewertz, P. McGale, A. M. Bennet, U. Blom-Goldman, D. Bronnum, C. Correa, D. Cutter, G. Gagliardi, B. Gigante, M. Jensen, A. Nisbet, R. Peto, K. Rahimi, C. Taylor, and P. Hall, Risk of ischemic heart disease in women after radiotherapy for breast cancer, *New England Journal of Medicine* **368**, 987 – 998 (2013). (p 78)